Novel Thermal Controller for Active Stabilization of Microring Modulators

Daniel Musat

A Thesis

in

The Department

of

Electrical and Computer Engineering

Presented in Partial Fulfillment of the Requirements

for the Degree of

Master of Applied Science (Electrical Engineering) at

Concordia University

Montréal, Québec, Canada

April 2024

CONCORDIA UNIVERSITY

School of Graduate Studies

This is to certify that the thesis prepared

By: **Daniel Musat**

Entitled: **Novel Thermal Controller for Active Stabilization of Microring Modulators**

and submitted in partial fulfillment of the requirements for the degree of

Master of Applied Science (Electrical Engineering)

complies with the regulations of this University and meets the accepted standards with respect to originality and quality.

Signed by the Final Examining Committee:

_____ Chair
Dr. John Xiupu Zhang

_____ External Examiner
Dr. Wen-Fang Xie

_____ Examiner
Dr. John Xiupu Zhang

_____ Supervisor
Dr. Glenn Cowan

Approved by _____
Dr. Yousef R. Shayan, Chair
Department of Electrical and Computer Engineering

_____ 2024

_____
Dr. Mourad Debbabi, Ph.D.,P.Eng., Dean
Faculty of Engineering and Computer Science

Abstract

Novel Thermal Controller for Active Stabilization of Microring Modulators

Daniel Musat

The bandwidth of electrical interconnects is reaching a bottleneck, leading to a surge of interest in silicon photonic interconnects. Microring modulators (MRM) are particularly attractive because of their high bandwidth, energy efficiency, and small size. However, implementing MRMs in commercial products is challenging due to their high thermal sensitivity caused by their high thermo-optic coefficient. Control systems that actively stabilize MRM have demonstrated the ability to compensate for thermal fluctuations, but none have addressed all system requirements for large-scale commercial applications. This work presents a simple and calibration-free method to stabilize MRM that can potentially fulfill all system prerequisites.

The proposed thermal controller requires a double-bus microring resonator (MRR) to monitor the through and drop averages and lock the operation where the through and drop power outputs are identical. This operating point has been shown to be within 3 % of the optimal optical modulation amplitude (OMA), making it an excellent operating point. Furthermore, this controller is proven to be immune to any external perturbations and requires only analog components. After designing and building a printed circuit board (PCB) that incorporated the proposed thermal tuner, experimental tests were conducted on the controller using an MRM. The obtained results served to validate the functionality of the controller.

Finally, in applications where MRMs have unbalanced input data, the original proposed design is demonstrated to suffer from a region of locking instead of a single operating wavelength. A modified design was then developed and validated to extend that approach to unbalanced data.

Acknowledgments

I want to express my gratitude to my supervisor, Prof. Glenn Cowan, for encouraging my graduate studies. His expert knowledge, guidance, and insightful input were instrumental in shaping the direction of my research.

I am immensely thankful to my collaborators for their invaluable assistance and expertise, which have played a critical role in the success of my research. Specifically, I would like to sincerely thank David Rolston, Prof. Odile Liboiron-Ladouceur from McGill, José García-Echeverría, and Ataollah Mahsafar for their outstanding contributions.

I thank the Canadian Microelectronic Corporation (CMC) for their assistance and financial support.

Additionally, I cannot express enough appreciation towards my beloved family members, including my parents, my brother Paul, and my sister Sandy, whose unwavering love and support have been a constant source of strength and encouragement.

Contents

List of Figures

List of Tables

Chapter 1

Introduction

The need for higher input/output (I/O) bandwidth in server computing systems is constantly growing [11]. As the technology node decreases, the core count and I/O bandwidth requirement increases, and it is projected that by 2030, they will both see a growth of 8-16x [12]. However, the performance limits of copper are causing a bottleneck in the headroom for electrical I/O interconnects [12]. In addition, the silicon die area is limited by the sizes of the interconnect pitches, such as sockets and ball grid arrays, and is projected to see an improvement of only 1.5x by 2030 [12]. As the number of cores increases, it becomes challenging for the area improvements to keep up. More power and area must be dedicated to I/O to fully utilize the cores, which poses a significant challenge for future server architectures [12]. Silicon photonic-based optical interconnects have the ability to significantly enhance bandwidth and data transfer rates owing to their compatibility with CMOS manufacturing [13]. Utilizing the advanced CMOS infrastructure enables the production of these interconnects at low cost and in high volume [1].

Silicon photonics benefits from the high refractive index contrast between silicon and its oxide, resulting in an unprecedentedly small footprint for silicon structures [1]. Microring-based devices specifically benefit from this high contrast since it allows bends as compact as a few micrometers [1].

1.1 Microring Modulators

A MRR is a circular waveguide where the cavity will be in resonance for coupled light whose wavelength is an integer multiple of its circumference. This property makes it useful in filter applications such as dense wavelength division multiplexing (DWDM). Moreover, MRR can function as modulators through the plasma dispersion effect, where the refractive index changes based on the carrier concentration in the waveguide. In [9], a complete DWDM system was demonstrated with the combination of a filter and modulator, using only MRRs.

One of the main shortcomings of MRRs is the high thermo-optic coefficient of silicon. This feature makes MRRs susceptible to temperature changes [14]. Even a minor fluctuation of just 1 $^{\circ}\mathrm{C}$ can cause a MRR to lose its operational functionality [2]. In addition, process variation can lead to shifts in resonance up to nanometer ranges in extreme cases [15]. As a result, the fabricated MRR may not accurately reflect the resonance that was originally intended. In order to ensure proper functionality of the MRR regardless of external perturbations, it is necessary to actively control its operating wavelength.

1.2 Active Stabilization of MRR

There is strong evidence to support the future large-scale commercialization of MRRs with active stabilization, as they have been successfully demonstrated in hybrid CMOS-silicon integration [9]. However, existing ring controllers require initial calibration for each individual structure in order to determine the ideal locking point. This can pose a significant obstacle to large-scale implementation. Ring controllers are typically equipped with integrated heaters that enable the control of the resonance of the MRR. The thermal controller can adjust the local ring temperature to shift the resonance to the desired location by monitoring the output power of the ring.

This work presents a controller that keeps track of the average power at both outputs of a double-bus MRR. The controller then utilizes an integrated heater to lock the MRR at the position where the average powers are equal. This, in turn, leads to a self-reference operating wavelength, thereby eliminating the need for calibration.

1.3 Thesis Organization

Chapter 2 introduces the theory behind microring resonators and their use as filters and modulators. In addition, it highlights the high thermal sensitivity of these devices and the need for thermal stabilization. Existing solutions are then presented and evaluated.

Chapter 3 describes a new approach to solving a microring modulator's high thermal sensitivity. It then provides both simulated and experimental results of the new design. Finally, data-dependent behavior is observed.

Chapter 4 provides a solution to the data-dependent behavior. Simulated results are then analyzed to validate the solution. Experimental results are then provided.

Finally, Chapter 5 compares the proposed solution to existing ones, summarizes the thesis, and presents future objectives.

1.4 Contributions and Publications

The author's work has devised and verified a novel technique for thermally stabilizing microring modulators by keeping track of the power difference between both outputs in a double-bus microring resonator. This method generates an error signal that increases monotonically with a zero crossing at an optimal operating point, which can be efficiently locked to with basic analog circuitry. The viability of this method has been established through rigorous simulations and experiments. Furthermore, the newly developed thermal

controller is entirely calibration-free and can withstand laser wavelength and power fluctuations, as well as process variations that commonly affect conventional thermal controllers of microring modulators.

In addition, a modification to this new thermal stabilization controller was described, enabling it to function effectively even with unbalanced data. The described modification to the microring modulators presents compelling evidence for their suitability in logic gate and switch applications where non-balanced data is common.

After the successful PCB implementation and testing, it has been established that the new thermal control approach is effective. This provides compelling evidence that an integrated chip based on this design can offer a competitive alternative to existing solutions.

A provisional patent application with Serial No. 63/550,369 was filled out based on this work on February 6, 2024. Now that a provisional patent has been submitted, a paper detailing this work is in preparation. In addition, another paper that utilizes this work for neural network weight banks is also being written.

Chapter 2

Background and Literature Review

This chapter begins by presenting the essential knowledge required to understand the functionality of MRRs and MRMs. Then, it explains why thermal stabilization is required for silicon MRRs. Additionally, it provides a brief description of how to use MRMs as logic gates. Finally, this chapter will provide a comparison of currently employed thermal control methods for MRMs, which will later be used to compare with the new proposed method described in Chapter 3.

2.1 Microring Resonators

Two basic structures of an MRR are shown in Fig. 2.1. The basic single-bus structure (A), also called an all-pass ring resonator, comprises two waveguides: a straight and a circular waveguide. For resonance to occur in the cavity, the circumference of the circular waveguide must be an integer multiple of the wavelength of light coupled into the resonator as given by eq. 1 where n_{eff} is the effective index, L is the ring's circumference, and m is a positive integer. This equation implies that multiple wavelengths can resonate in the circular cavity, where the distance between successive resonances is called the free spectral range (FSR). Based on the self-coupling, cross-coupling ratio, and circumference of the

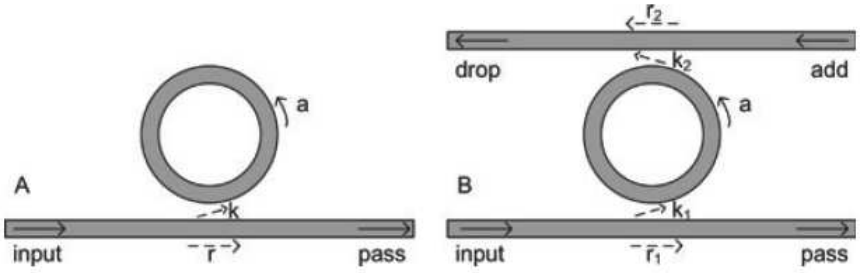

Figure 2.1: (A) Single-Bus and (B) Double-Bus Micoring Resonator in [1]

microring resonator, the transmitted output at the through port will experience destructive interference (at resonant wavelength) or constructive interference (at non-resonant wavelength). This structure acts like a notch filter since all wavelengths are transmitted except resonant ones.

$$\lambda_{res} = \frac{n_{eff} L}{m} \tag{1}$$

The double-bus structure in Fig. 2.1 adds a straight path waveguide compared to the single-bus. This addition allows resonant wavelengths in the cavity to couple to this new waveguide, also called the drop port. Any wavelength other than the resonant one will not couple into the drop port.

Fig. 2.2(A) shows the normalized transmission spectrum of the through and drop port for a double-bus ring resonator. In the case of a single-bus, the drop port transmission is removed. This plot shows the physical representation of the FWHM and resonant wavelength. The FWHM, as the name implies, is the width of the spectrum where the spectrum value is half its maximum. The resonant wavelength is located at the minimum of the through spectrum or maximum of the drop spectrum. Fig. 2.2(B) demonstrates the periodic behavior of the resonance and shows the physical representation of FSR.

A few spectral characteristics are essential when discussing MRRs: the FSR, the FWHM, the quality factor (Q-factor), and the resonant wavelength. The FSR was explained earlier

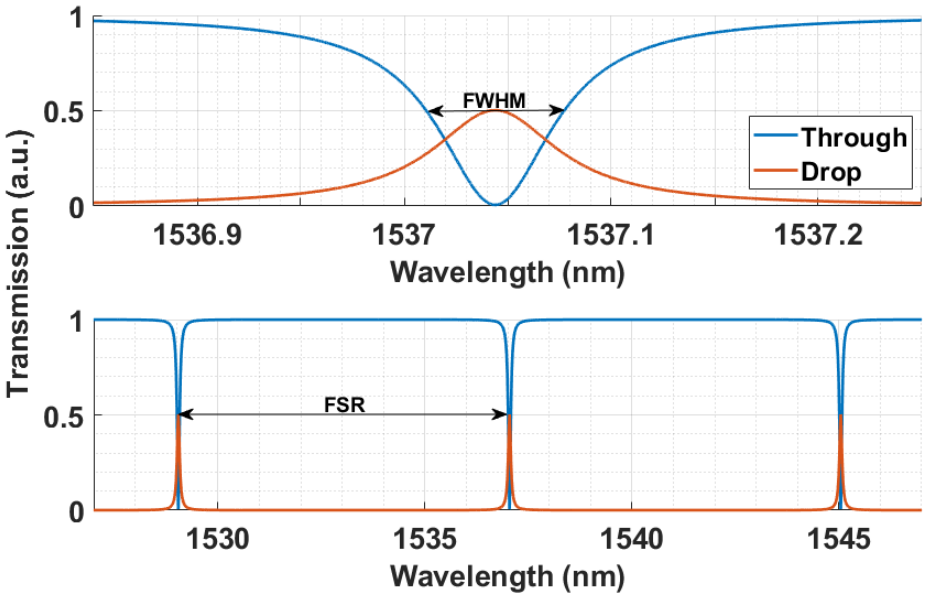

Figure 2.2: (A) Transmission spectrum example of a double-bus microring resonator with the Full-Width at Half Maximum (FWHM) and (B) Periodic resonance occurring at FSR intervals

and is defined in eq. 2 where L is the round trip length, and n_g is the group index to account for the dispersion in the waveguide [1]. This equation shows that the FSR can be chosen based on the circumference of the cavity: a larger path length leads to a smaller FSR, and vice-versa. Eq. 3 gives the double-bus FWHM where r_1 and r_2 are the self-coupling coefficients of the through and drop port respectively, and a is the single-pass amplitude transmission [1]. Finally, the Q-factor represents the steepness of the resonant slope. Eq. 4 defines the Q-factor. This equation shows that the Q-factor is inversely proportional to the FWHM; therefore, a higher Q-factor implies a steeper slope or a smaller FWHM.

$$FSR = \frac{\lambda_0^2}{n_g L} \tag{2}$$

$$FWHM = \frac{(1 - r_1 r_2 a)\lambda_{res}^2}{\pi n_g L \sqrt{-r_1 r_2 a}} \tag{3}$$

$$Q - factor = \frac{\lambda_{res}}{FWHM} \tag{4}$$

Depending on the application of the MRR, the coupling and length of the ring can be chosen to optimize for that application. An example of an application for the microring resonator is to use it as a filter to add or drop specific wavelengths from the waveguide, which is critical for wavelength division multiplexing (WDM) applications. Apart from its use as a filter, the microring resonator can also function as a modulator, known as a microring modulator (MRM), which is elaborated on in the upcoming subsection.

2.2 Microring Modulator

Optical modulators alter the amplitude, phase, or polarization of a propagating light beam [14]. The modulator encodes information in the light by varying these properties, which enables data transmission from one point to another. The MRM achieves this in two ways: thermal modulation or through the plasma dispersion effect [14]. Due to its slow process, thermal modulation is unsuitable for meeting today's high-speed transmission demands. Consequently, the only viable option is to use the plasma dispersion effect, which is the change in refractive index due to the carrier concentration in silicon [14]. Refer to Eq. 1 to understand how the plasma dispersion effect allows modulation. This equation shows that the resonant wavelength is a function of the effective index of the ring. Thus, the resonant wavelength will shift by modifying the number of carriers in the ring due to the plasma dispersion effect.

Carrier density manipulation in the circular waveguide of the MRM is realized through depletion, carrier injection, or accumulation [14]. Carrier injection requires a portion of the microring resonator to be surrounded by a p-i-n diode, while depletion requires a p-n diode [1]. Fig. 2.3 shows the top view and cross-section of a circular waveguide for an MRM. When reverse-biasing the p-n diode, the magnitude changes the width of the depletion region in the waveguide, effectively changing the effective index. When forward biasing a p-i-n diode, carriers are injected in the waveguide, which, once again, changes the effective index. In the injection-based modulation, the resonant peak is blue-shifted (meaning the resonance moves towards lower wavelengths). In contrast, the resonant peak is red-shifted (meaning the resonance shifts towards higher wavelengths) in the depletion-based modulation. Both methods are relatively fast, but injection is limited by the recombination time of the carriers; it is a slower process [1] compared to depletion; therefore, it is less used to design a modulator.

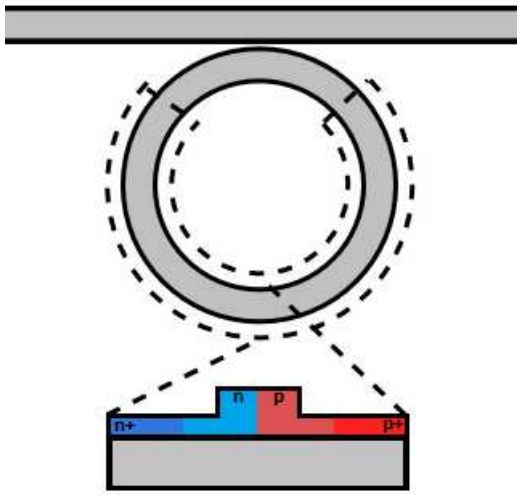

Figure 2.3: Top view and cross-section of the circular waveguide of a depletion-based MRM based on [1]

Fig. 2.4 illustrates how modulation is achieved by rapidly shifting the resonant wavelength. For an unbiased ring, no voltage is applied to the diode's p-n junction, and the

resonance remains at its original location. Once a reverse bias voltage is applied to the diode, the depletion region width increases, and the carrier concentration reduces in the ring. As a result, the effective index changes and red-shifts the resonant wavelength, as seen in the figure. This transition in resonance occurs rapidly, typically within 0.1 ns, and is constrained by the depletion region capacitance [1]. The continuous-wave (CW) laser at the input gets modulated at the MRM's outputs by rapidly varying the reverse bias voltage.

From Fig. 2.4, the quality of the modulated output highly depends on the ring's input laser wavelength. No modulation occurs at the output when the input light is significantly far from the resonance. However, if the input laser is positioned near the slope of the unshifted resonance wavelength, a signal with a robust optical modulation amplitude (OMA) can be detected at the output, as seen from λ_1 and OMA_1 in the figure. The resonant wavelength must be precisely controlled and locked to the desired wavelength to ensure an optimally modulated output against external influences. For example, if the input laser wavelength fluctuates from λ_1 to λ_2 as shown in the figure, the OMA at the output reduces by more than half.

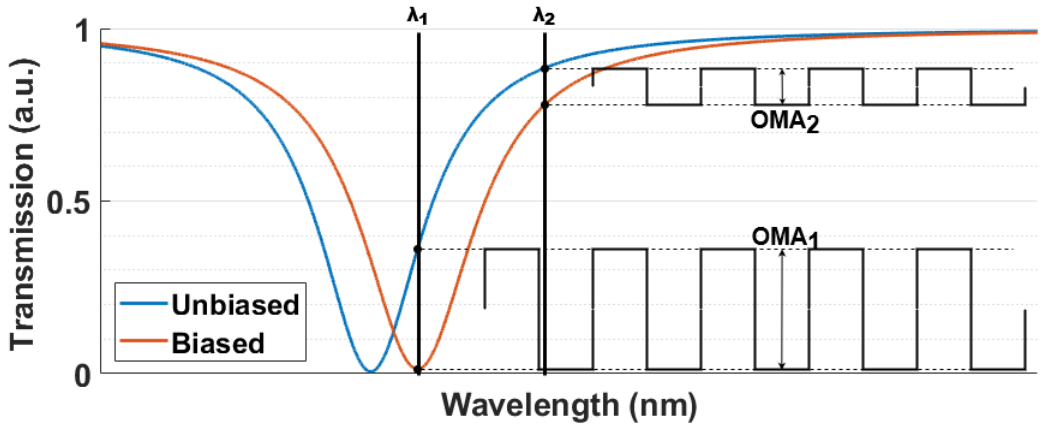

Figure 2.4: Modulation from a rapidly varying reverse bias voltage dependent on the CW laser's wavelength

When searching for the optimal locking wavelength, it is crucial to consider the relevant

figures of merit. In current modulator designs, three main performance metrics are examined: the extinction ratio (ER), the optical modulation amplitude (OMA), and the transmission penalty (TP). However, these three metrics highly depend on the locking point and do not overlap.

The ER is important since it measures the power ratio between a 1-bit and a 0-bit. It also allows us to estimate the distance that the modulated data can be transmitted compared to the losses in the waveguide or fiber. Therefore, a high ER is desired for long-haul communication. The ER is usually expressed in decibels (dB) and is defined in eq. 5 where P_1 is the optical output power of a 1-bit and P_0 is the optical output power of a 0-bit in mW.

$$ER[dB] = 10\log_{10}(\frac{P_1}{P_0}) \tag{5}$$

The OMA is defined as the optical amplitude at the output of the ring. A higher OMA leads to a better bit-error rate (BER) and a larger eye-opening. The OMA is a better figure of merit for shorter-reach applications where the ER is less important. The OMA is in linear units and is defined by eq. 6.

$$OMA[mW] = P_1 - P_0 \tag{6}$$

The minimum TP gives the optimal trade-off between the insertion loss (IL) and ER [16]. At the optimal ER, the IR increases significantly; thus, a compromise is desired when locking to the minimum TP. The Tp is given in eq. 7 where P_{in} is the input optical power.

$$TP[dB] = -10\log_{10}(\frac{P_1 - P_0}{2P_{in}}) \tag{7}$$

2.3 Thermal Sensitivity and Process Variation

As previously mentioned, a robust tuning mechanism for the MRM is required to lock at the optimal wavelength and compensate for external thermal fluctuations and process variation. Silicon exhibits a significant thermo-optic coefficient [14], meaning that a slight shift in temperature can significantly change the effective index, which, in turn, alters the resonant wavelength according to eq. 1. For microring resonators, the typical values of the thermo-optic shift are within the range of 0.07-0.12 nm/$^{\circ}$C [17, 18]. To optimize for speed and efficiency, MRMs are typically used with a Q-factor around 5000-25000 [1], leading to an FWHM of around 0.06 - 0.3 nm, as per eq. 4 in the C-band. Therefore, even a small 1 $^{\circ}$C temperature change can significantly alter the locking point and potentially destroy the modulated data.

In addition, the manufactured resonance of the ring resonator will not necessarily be located at the designed location. Process variation can affect the final resonant wavelength. [19] reports a 0.15 - 0.55 nm standard deviation in resonance between rings in the same chip depending on the distance between rings and a 1.8 nm deviation for rings on different chips.

However, these external factors can be managed using the thermo-optic effect. By integrating a local microheater near the ring and taking advantage of the high thermo-optic coefficient, the resonance can be red-shifted by increasing the temperature of the local area [18]. It is important to note that this allows only heating and passive cooling, so the ring will need to be continuously heated for locking, which can increase the energy consumption of the ring [1]. This partially negates the low energy consumption advantage of the microring resonator.

2.4 Logic Gates

A logic gate is usually an electronic circuit that operates on one or more binary inputs and produces a single binary output, performing a specific boolean function. The basic logic gates are AND, NAND, OR, NOR, XOR, XNOR, and NOT. Fig. 2.5a illustrates the logic gate diagram for an AND gate, and Table 2.5b displays its corresponding truth table. The truth table is derived from the boolean expression A and B = Y. Each basic logic gate has its unique boolean expression and consequently, different truth tables. These logic gates are fundamental building blocks in digital circuits. They are implemented in various applications, including digital computers, memory units, data storage, digital signal processing, communication systems, and many more.

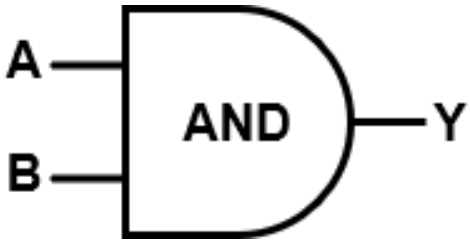

(a) Logic gate symbol

A	B	Y
0	0	0
0	1	0
1	0	0
1	1	1

(b) Truth Table

Figure 2.5: AND Logic Gate

As previously mentioned, the limitation of copper is causing a bottleneck in I/O interconnects. Therefore, there is a growing interest in all-optical devices, such as optical computing, which are less limited in speed and distance than electronics. Fig. 2.6 illustrates a method to use MRMs as logic gates. Two optical inputs (A and B) are converted to electrical equivalents, which are typically done with photodiodes (PD) and transimpedance amplifiers (TIA). Then, an electronic AND logic gate performs the boolean expression to obtain $Y_{electrical}$. This signal then reverse-biases the pn junction diode of the MRM. The AND operation, $Y_{optical}$, can appear at the through or drop output depending on where the MRM is locked on its resonance spectrum. In the figure, it is assumed that it is locked in the region where $Y_{optical}$ appears at the drop output and $\overline{Y}_{optical}$ is at the through output.

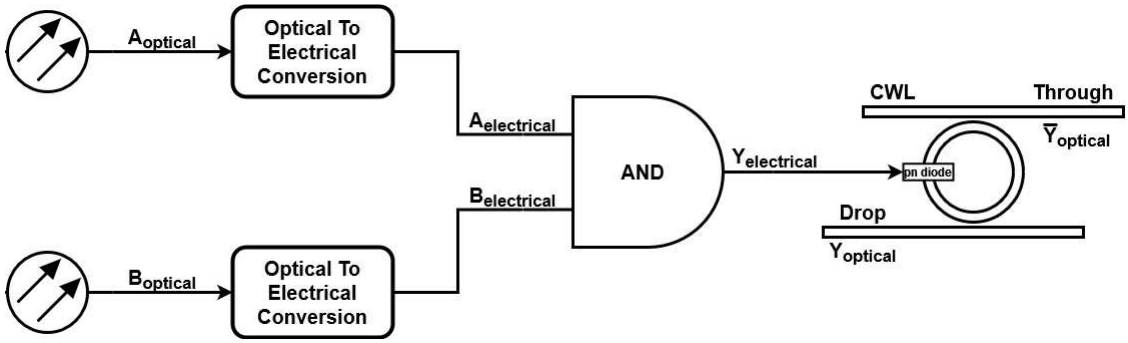

Figure 2.6: Potential AND logic gate for MRRs

This logic gate is not all-optical and incorporates electro-optic conversions. More research needs to be done in this area to have a fully optical logic gate using MRMs.

Although electro-optic conversions are still incorporated, this is still desired in long-reach applications since optical signals can travel farther distances without limiting signal speed. An optical AND and NOR gate are demonstrated using a cascade of two Mach-Zehnder interferometers (MZI) in [20]. In this case, an optical input and output and two thermal inputs allow for AND and OR gate operation.

2.5 Current Thermal Control Methods for MRM

As mentioned in the previous section, microrings are highly sensitive to temperature fluctuations, necessitating the microring's thermal stabilization. The optimal thermal stabilization has the following key features: WDM compatible, immune to process and temperature variation, immune to laser wavelength and power variation, self-heating cancelation, locked at an optimal wavelength, large tuning range, low power consumption, and small footprint. Current control techniques address some of these features but have yet to demonstrate a system that satisfies all criteria.

Five promising solutions have been researched to thermally lock MRM: athermal devices [10, 21, 22], thermal dithering feedback control [4, 5, 23], temperature sensor thermal

compensation [6,24,25], through or drop port power monitoring [26–28], and photocurrent-based control [9]. This section will elaborate on the different implementations of these methods and their advantages and disadvantages.

2.5.1 Average Power Monitoring

The most common method for locking a MRM involves monitoring the average power of either the through or drop port, as noted by various studies [3, 26–30]. A 10% tap is placed at either output waveguide of the ring resonator, which is detected by a PD responsible for converting power to current based on its responsivity. The current is then converted to voltage by a low-speed TIA. Finally, a feedback controller is employed to regulate the voltage/current applied to the integrated microheater of the ring.

The research conducted by [2, 28] was the first to demonstrate that this ring control method could achieve high-speed error-free performance. Their work utilized a gcarrier injection MRM, which requires forward diode biasing. An integrated heater is not needed for injection-based MRM since a change in the biasing current of the p-i-n diode significantly heats the rings due to carrier recombination. Thus, temperature stabilization can be achieved by controlling the biasing current of the diode. This was first shown in [31] with a 15 $^{\circ}$C temperature tuning range; however, they had to manually change the biasing current to lock the ring, which is impractical in real applications.

Figure 2.7 shows their experimental measurement of the mean optical power at the through output for a wavelength sweep of the resonance spectrum while the microring is being modulated. In addition, the eye diagram of the on-off keyed (OOK) output signal at different possible locking wavelengths is displayed. In the dashed red region of the figure, the eye diagram of the output signal is suitable for transmission.

Figure 2.8 showcases the experimental setup that was used to demonstrate error-free modulation. The feedback control first compares the mean of the transmitted optical power

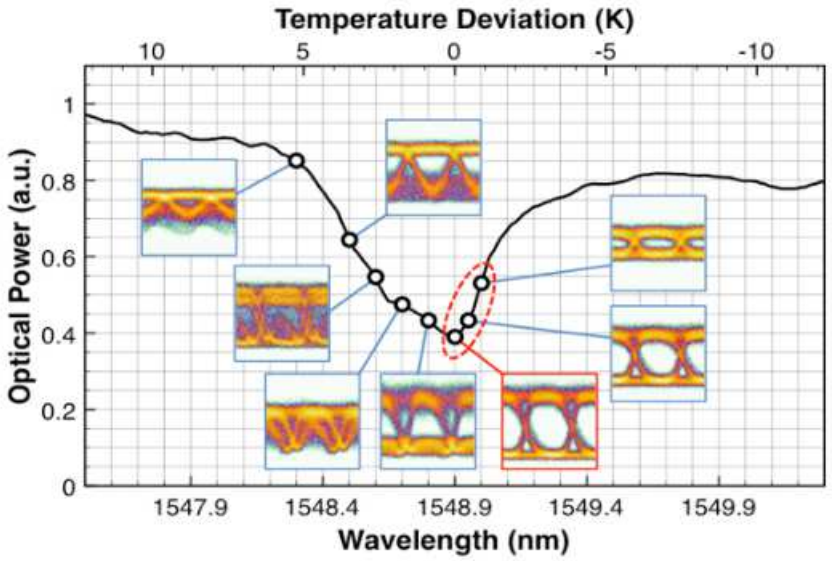

Figure 2.7: Normalized mean optical output power after a wavelength sweep for a modulated ORR in [2]

to a reference value, which generates an error signal. This error signal becomes the input to a proportional-integral-derivative (PID) controller. The PID output changes the forward biasing current of the ring's diode, which has the ancillary effect of changing the local temperature of the ring. The PID then continues to modify the biasing current until the error signal equals zero.

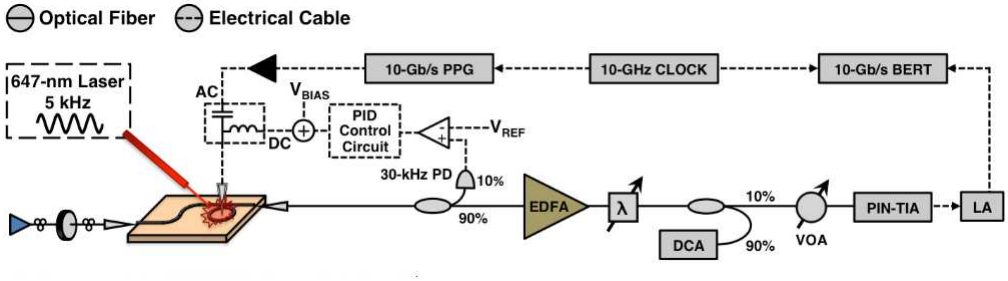

Figure 2.8: Experiment setup for error-free MRM in [2]

For this control to work, it is necessary to place the locking wavelength not at the minimum mean optical power where the ideal OOK signal is generated but in the middle of

the slope within the red dashed circle of Fig. 2.7 [2]. Setting the reference voltage to the minimum will result in a positive-only error signal; thus, locking will not occur. However, positioning the reference voltage in the middle will yield an error signal with a monotonically increasing slope and zero crossing. An increase in the mean optical power suggests a decrease in temperature, while a decrease in mean optical power implies a temperature increase [2]. This process involves negative feedback with an error signal that can lock to zero.

In their publication [3], the same group introduced an improved integrated version of their control scheme. The mean optical power was monitored at the drop port instead of the through port, which eliminated the need for a power tap of the modulated output. Additionally, they used a depletion-based MRM, which allowed for faster modulation speeds. Depletion-based MRM implies using an integrated microheater instead of changing the bias of the diode's current to vary the local temperature of the MRM. The feedback control remained almost the same, except for the optical mean being monitored at the drop port and the use of an integrated heater to vary the temperature instead of the diode bias. Figure 2.9 shows the simplified control system diagram.In this figure, the PD responsible for measuring the drop port output power is not biased to eliminate the dark current. Although this will decrease the PD's response time, it is not a significant concern since the control measures the average power, which operates at slow speeds.

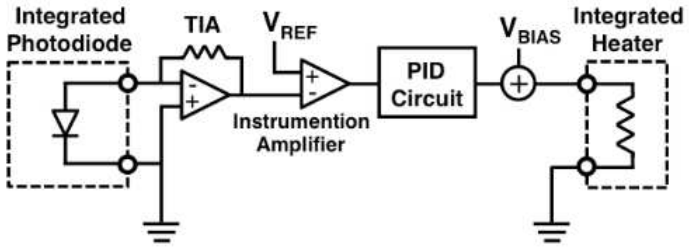

Figure 2.9: Thermal Stabilization Control System in [3]

This control scheme offers several advantages, such as being low-cost and energy-efficient due to its implementation with low-speed analog circuitry. Additionally, drop port monitoring ensures WDM compatibility by preventing wavelengths far from resonance from coupling in the drop port. [26] has developed a fully integrated version of this scheme using a monolithic 45 nm CMOS-Silicon-Photonics (Si-Ph) platform, which has an ultra-compact footprint of 200 μm x 220 μm.

However, the main drawback of this technique is that it requires a reference value, which means going through an initial calibration process to determine the optimal reference value. Moreover, any input laser power or wavelength modifications require restarting the calibration process.

Various implementations of this control scheme have been demonstrated [27, 29, 30], in which the feedback is digital and utilizes specific algorithms. [27] has an automated initial calibration but is still not immune to laser input power and wavelength variations. Any method that requires saving a reference value will suffer from this drawback.

2.5.2 Thermal Dithering Control

Thermal dithering is another effective method to stabilize ORRs [4, 5, 23]. This technique involves applying a small, low-speed dithering signal to the integrated heater of the MRM. This creates a small, modulated optical output, as demonstrated in Fig. 2.10.

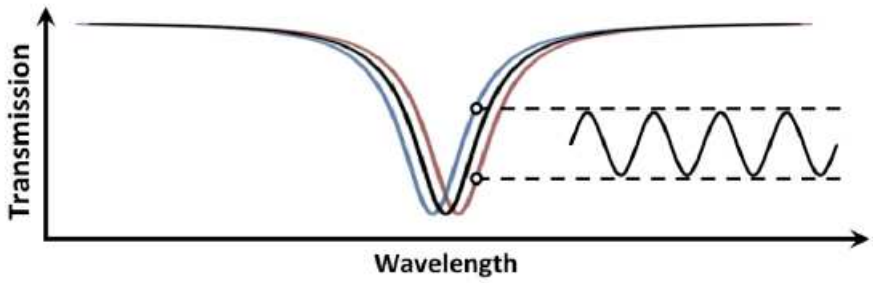

Figure 2.10: Optical modulated output due to dithering signal in [4]

The drop port is monitored with a PD to capture the small modulated optical output, given that the TIA's bandwidth is higher than the frequency of the dithering signal. Depending on whether the input laser wavelength is blue or red-shifted compared to the resonant wavelength, the drop port signal will be in-phase or out-of-phase, respectively, relative to the dithering signal [4]. By mixing the dithering signal with the TIA output, the mixer output is obtained with eq. 8 where the dithering frequency is f_D, the phase difference is θ, and the multiplication of both signal amplitudes is A [4]. A low-pass filter can filter the higher harmonic to obtain $\pm\frac{A}{2}$. Note that A is not constant and depends on the location of the input laser wavelength compared to the resonant peak. Finally, this process generates an error signal with a monotonic slope and zero crossing, which makes it easy to lock with a PID controller.

$$A[cos(2\pi f_D t)cos(2\pi f_D t + \theta)] = \frac{A}{2}[cos(4\pi f_d t + \theta) + cos(\theta)] \tag{8}$$

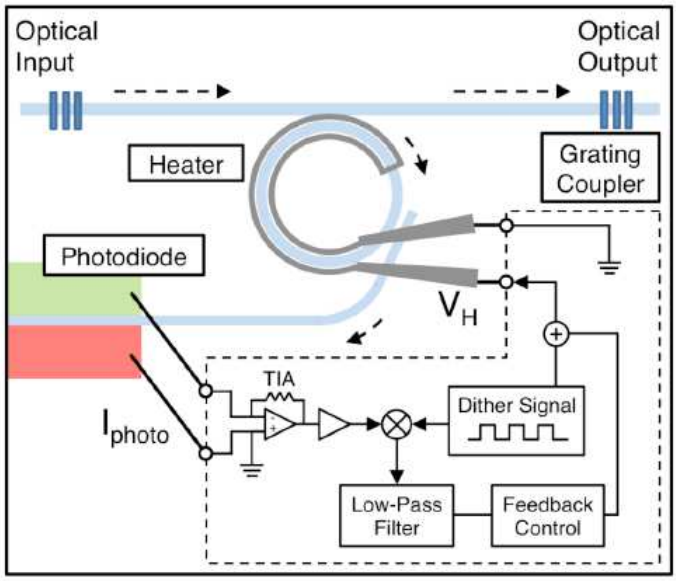

Figure 2.11: Experimental setup for dithering signal locking in [4]

Fig. 2.11 shows the experimental setup utilized for demonstrating this locking technique. The output and dithering signals are mixed, and the higher harmonic is filtered out. The filtered output is the error signal shown in Fig. 2.12. A PID controller drives the error signal to zero by changing the integrated heater's applied voltage.

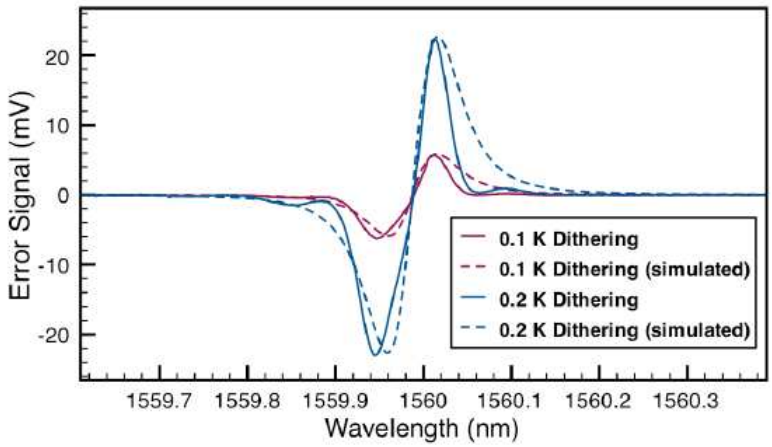

Figure 2.12: Error signal as a function of input laser wavelength for different dithering amplitudes in [4]

As per the experimental results in Fig. 2.12, the error signal exhibits a monotonic slope and crosses zero at the resonant peak. A flaw in this method can be seen from the figure where the error signal is also zero when the input laser wavelength is far from the resonant wavelength. A more refined methodology was proposed in [32], comprising additional circuitry featuring ramp, reset, and hold states. At start-up, the ramp state activates and increases the local temperature of the ring until the error signal becomes non-zero and trips the system into the hold state. The feedback controller is activated in the hold state to stabilize the ORR to the minimum of the optical transmission.

When the ORR is used as a filter with this control method, its locking point is at the minimum transmission, which is optimal. However, the locking does not modulate the output. In Fig. 2.10, the modulated blue and red signals are the same when the black line is at its minimum. Therefore, the modulated output will have a zero amplitude at this locking

wavelength. If this method is to be used for MRM, extra digital circuitry is required to lock at one of the peaks in the error signal, which would also require storing a reference value.

The dithering control has been further refined for application to ring modulators, as described in [5]. As opposed to the original method that involved taking the first derivative of the ring transfer function, the second derivative is obtained by demodulating the output signal using a lock-in amplifier at twice the dithering frequency, as stated in [5]. After Taylor-expanding the heat to output power transfer function of the ring around the locking point, eq. 9 was derived, representing the optical output power of the through port where $H(W)$ is the transfer function, W_{dith} is the dithering amplitude, W_0 is the average heater power, and f_{dith} is the dithering frequency [5].

$$\begin{aligned} P_{OUT}[W] =& P_{IN}\{H(W_0) + H'(W_0)[W_{dith}sin(2\pi f_{dith}t)] \\ &+ \frac{H''(W_0)}{2}W_{dith}^2\left[\frac{1}{2} - \frac{1}{2}cos(2\pi 2 f_{dith}t)\right]\Bigg\} \end{aligned} \tag{9}$$

According to this equation, it is possible to demodulate the second derivative of the ring's transfer function by using a lock-in amplifier with a reference frequency equal to twice the dithering frequency. This second derivative is shown in Fig. 2.13.

This graph shows a monotonic slope with a zero crossing at the maximum slope of the ring transfer function where the ER is close to optimal. Thus, a PID controller in feedback can lock the ring at an optimal operating point. Far from resonance, the error signal is also zero; therefore, it still requires extra circuitry during the initial start-up of the device (ramp, reset, and hold states) to find the resonance, but once it is locked, this design becomes immune to any power and wavelength fluctuation in the input laser, unlike the designs that require a reference value.

This locking method has many advantages: WDM compatible, immune to process and temperature fluctuations, immune to input laser power and wavelength fluctuations, and locks near the minimum TP. This method can also lock the ring for filter applications, not

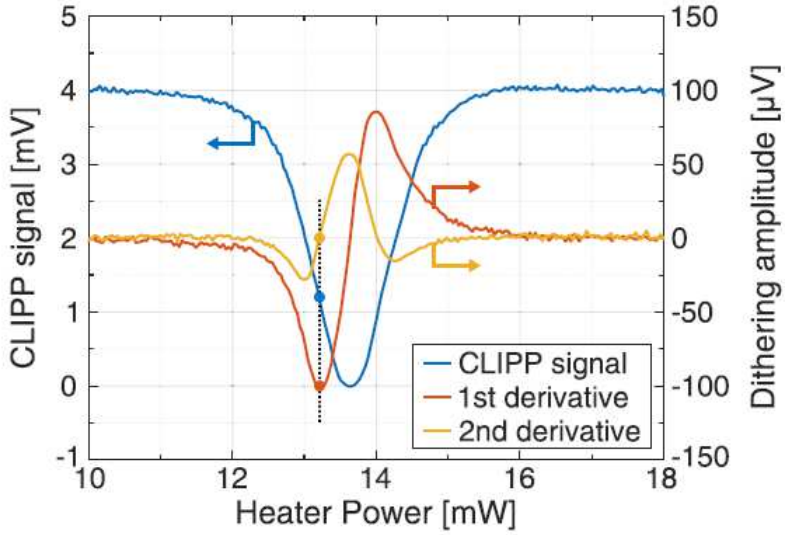

Figure 2.13: Measurement of the first and second derivatives of the ring's resonance spectrum in [5]

only for applications as a modulator. This technique has a drawback, as the dithering signal applied to the integrated heater causes a reduction in the final ER. Specifically, a dithering amplitude of 100 μW results in a significant ER decrease of up to 4 dB.

2.5.3 Sensor Locking

An alternative approach for ring-locking is to monitor the local temperature of the ring rather than the output optical power. There are two experimental methods to demonstrate this technique: using a digital infrared camera to measure the difference in optical scattering from a dual-ring resonator [33] or utilizing a temperature sensing diode [6, 24, 25, 34].

The latest local ring temperature sensing research uses Proportional to Absolute Temperature (PTAT) sensors. [6] uses these sensors to monitor the temperature of the ring directly and then regulate it with an integrated heater. The forward bias voltage difference between two diodes placed near the ring is shown in eq. 10 where T is the temperature, K is the Boltzmann constant, q is the electron charge, I_S is the reverse saturation current , I_D

is the diode current, and n is the emission coefficient.

$$V_{diff} = \frac{nKT}{q} \ln(\frac{I_{S1}}{I_{S2}} \frac{I_{D2}}{I_{D1}}) \tag{10}$$

Fig. 2.14 demonstrates the feedback mechanism utilized in this design. The difference between the diodes is measured and compared to a programmable offset. The voltage difference between the diodes is measured and compared to a programmable offset. Subsequently, an ADC-based digital system is employed to maintain a constant temperature, which enables the ring to lock at any desired location on the ring spectrum by programming the offset.

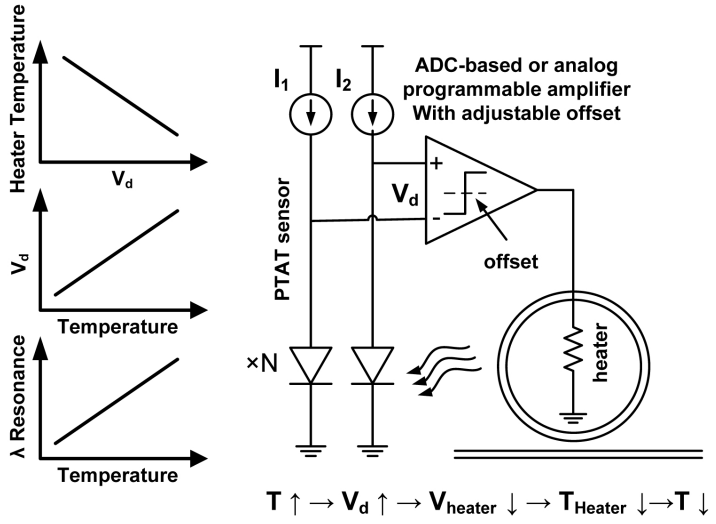

Figure 2.14: Feedback Control Block Diagram for PTAT-based locking in [6]

Compared to other active thermal stabilization methods, this technique directly measures the ring temperature instead of relying on indirect measurements of the ring output. With additional circuitry, automatic locking can be achieved during the initial start-up of the ring, as demonstrated in [34]. However, this solution is susceptible to input laser wavelength variations as it requires saving a reference value, similar to the average power monitoring case. The scattered light solution proposed in [33] entails a complicated process of

monitoring scattered light through cameras, which renders its implementation on a smaller scale quite challenging.

2.5.4 Real-Time Power Monitoring

The temperature stabilizing methods discussed until now are at low speeds compared to the modulated data since the thermal effect is a slow phenomenon, and they either monitor the output power or temperature of the ring. In contrast, [7] and [8, 34] take a different approach by monitoring the Bit-Error-Rate (BER) and optical modulation amplitude (OMA) of the output of the ring, respectively. These two approaches directly monitor the quality of the output data, which guarantees an excellent output in either BER or OMA.

The diagram displayed in Fig. 2.15 provides an overview of the temperature feedback control system that optimizes for BER, as described in [7]. The drop port output data is compared with the transmitted data through an error detection block. According to the paper, a zero error occurs when the receiver reads a 1 but the transmitter sends a 0, while a one error occurs when the opposite happens. Based on the number of zero or one errors detected, the control circuit decides whether to increase or decrease the integrated heater's power to shift the resonant curve until no more errors are detected.

This method has numerous advantages: laser wavelength and power immunity, error-free modulation, and WDM compatibility. However, due to its high speed and complex circuitry, it consumes more power, which could be a disadvantage. Furthermore, as the modulator data rate increases, the power consumption could escalate further.

The feedback control setup for locking to optimal OMA [8] is illustrated in Fig. 2.16. The method proposed in the paper entails measuring the power of individual 1-bit and 0-bit signals and taking their difference to obtain a voltage reading representing the output data's OMA. By comparing the current OMA voltage and its previous value at a sampling rate higher than the thermal time constant, a 1-bit slope quantizer can track the slope of the

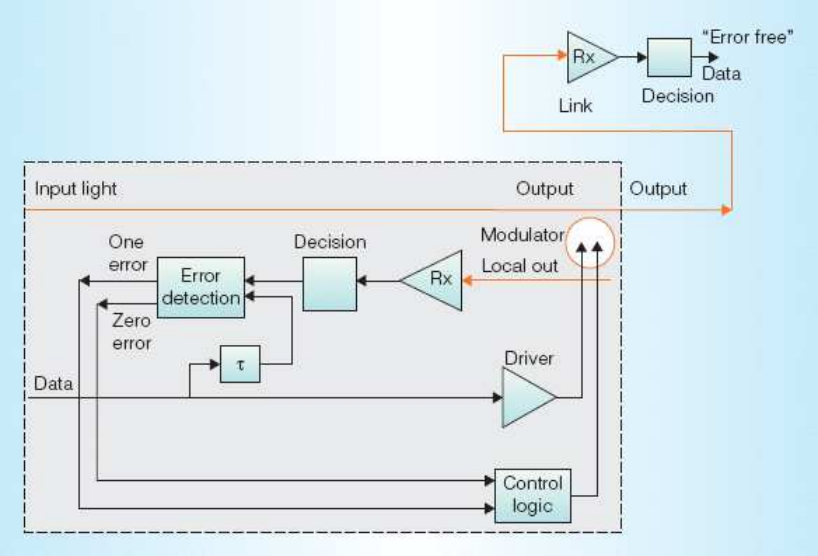

Figure 2.15: Block diagram of the thermal control that optimizes for BER in [7]

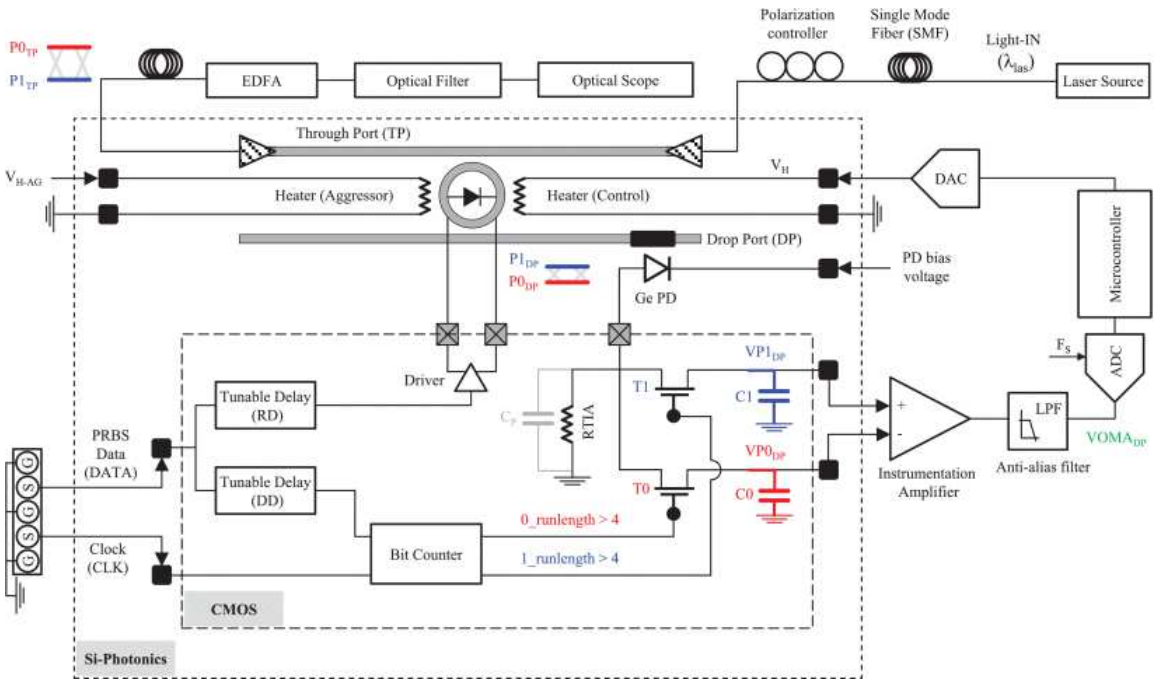

Figure 2.16: Schematic of the thermal control that locks to optimal OMA in [8]

OMA and outputs a 1-bit quantized λ_e depicted in Figure 2.17. Finally, this output goes into an up-down counter, followed by a digital-to-analog converter (DAC), which applies its output to the integrated heater to close the feedback loop. The experimental setup in Fig.

2.16 has the 1-bit slope quantizer and up-down counter implemented in a microcontroller.

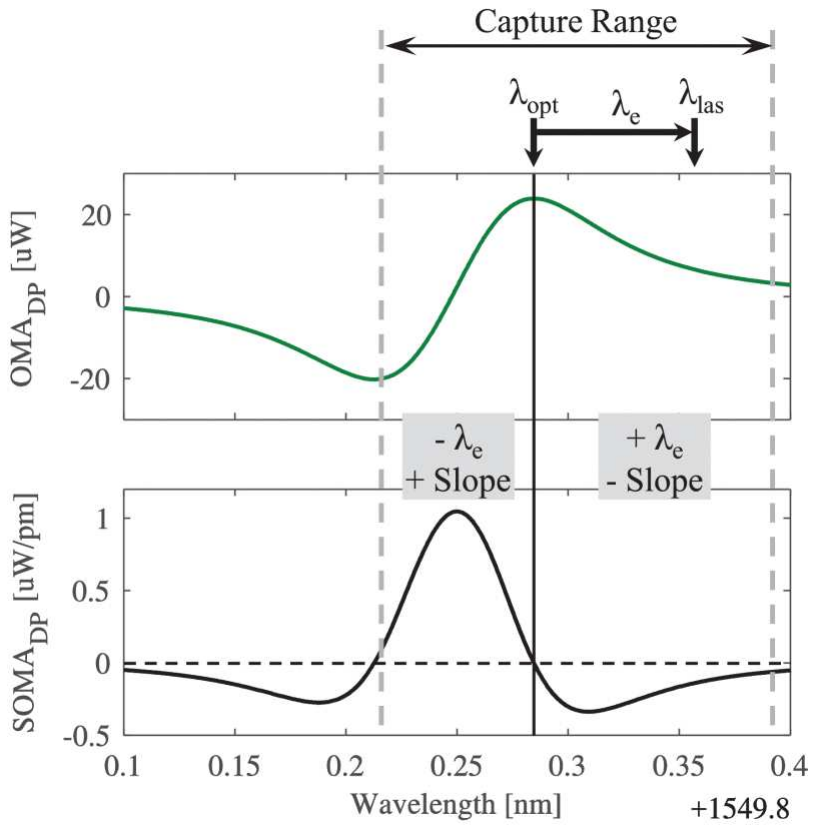

Figure 2.17: OMA and its slope as a function of wavelength near resonance in [8]

Upon initial examination, it may seem that this method necessitates high-speed TIAs to capture the output power for a 1-bit and 0-bit. However, the design features a bit counter that activates the sampling transistor only upon detecting a specified number of consecutive 1-bits or 0-bits [8]. This bandwidth reduction is only possible because the input-modulating data is known for MRM. This control method will not work for a filter application.

This method incorporates all critical features required for use as an MRM. However, using a passive TIA increases the signal-to-noise ratio (SNR), requiring larger sampling capacitors, increasing the control scheme's footprint, and thus reducing scalability. This method requires low noise for accurate stabilization due to the OMA comparator.

2.5.5 MRM Photocurrent Sensing

Wirebonding is required between chips in a hybrid solution with photonic and electronic chips, and the total number of wirebonds is limited. Therefore, the extra interfaces required for thermal control, like PDs for the average power monitoring control, are undesired in a system with many rings. A technique to mitigate the number of connections is described in [9], where the photocurrent generated from the p-n diode that modulates the MRM is measured instead.

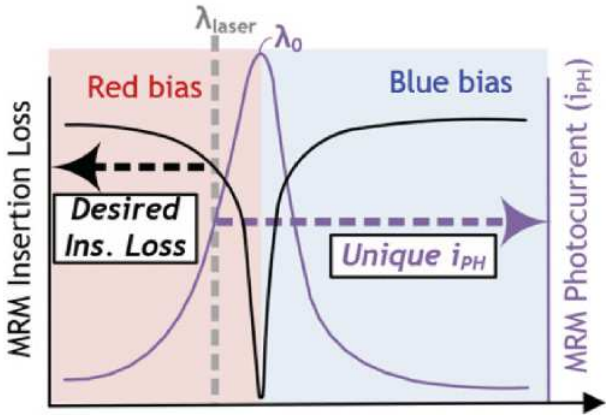

Figure 2.18: MRM photocurrent at resonance as a function of wavelength in [9]

Fig. 2.18 shows the MRMs photocurrent as a function of wavelength near resonance. This curve is similar to the one obtained from a monitor PD at the drop port. This current is compared to the current generated from a PD at the input of the ring. Careful tuning of the ratio of the TIA gains for both these currents allows for locking at a targeted insertion loss (IL) with the use of a bang-bang controller [9]. The controller changes the power to an integrated heater to adjust the local temperature of the ring. The thermal control block diagram is shown in Fig. 2.19.

Most features for MRM control are incorporated in this control scheme. Since the current is compared to a monitor PD at the input of the ring, the device becomes immune to power fluctuations in the input laser, unlike average power monitoring schemes. The

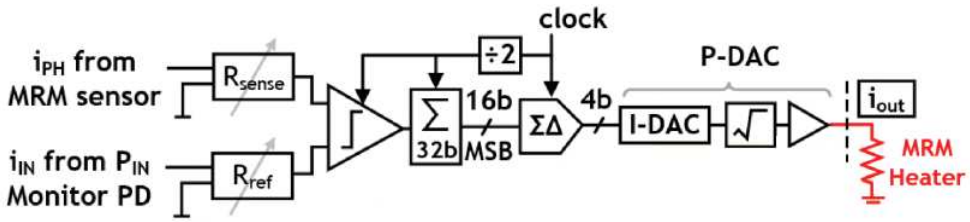

Figure 2.19: Thermal control block diagram for MRM photocurrent sensing in [9]

biggest drawback of this method is the rigorous calibration process required in adjusting the TIA gain ratios for each ring in the design.

2.5.6 Athermal ORR

As previously mentioned, ORRs are made with silicon, which has a high thermo-optic coefficient, making ORRs highly sensitive to temperature fluctuations. Rather than actively controlling the ring temperature to compensate for this thermal sensitivity, which is the case for most solutions presented, two alternative approaches try to reduce the ring's temperature dependence instead. These methods include having additional material in the cladding with negative thermo-optic coefficients [10,22] or using an additional Mach-Zehnder interferometer (MZI) [21].

The concept of athermalization of waveguides is not novel and was first demonstrated in [35]. [10] adopts this technique for ORR. This technique involves compensating silicon's positive thermo-optic coefficient with a material with a negative thermo-optic coefficient of the same magnitude. This approach has been successfully demonstrated using both a polymer cladding [10] and a titanium oxide cladding TiO_2 [22]. The ORR design needs to ensure that the aggregate thermo-optic coefficient is near zero [32].

The cross-section of the ring's waveguide with the polymer cladding is depicted in Fig. 2.20a, while Fig. 2.20b illustrates the critical need for the waveguide width to be fabricated within strict limits to avoid high-temperature dependence. The final fabricated ORR had an

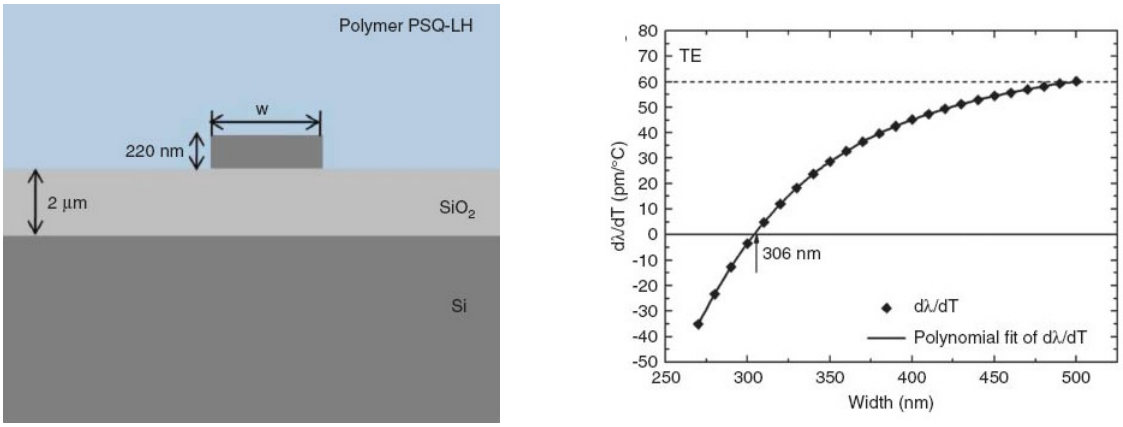

(a) (b)

Figure 2.20: (a) Cross-Section of the ORR waveguide with polymer cladding and (b) Calculated wavelength temperature dependence as a function of waveguide widths for SOI waveguides with a polymer cladding [10]

ideal width of 350 nm with temperature dependence of -5 pm/$^{\circ}$C over a 50 $^{\circ}$C temperature range [10].

The manufacturing process faces difficulty consistently meeting the stringent waveguide width requirements [35]. In addition, polymers and the CMOS-fabrication process are not very compatible due to the degradation of the polymer in high-temperature environments [35]. For this reason, research conducted in [22] uses TiO_2 cladding instead. The strict waveguide requirement is still there, but the compatibility with the CMOS fabrication process is improved.

These results show that using a negative thermo-optic coefficient material for the cladding is a viable solution to nearly eliminate the temperature sensitivity of rings. This solution should become more popular once the fabrication process improves and the waveguide width falls within the fabrication tolerance. This method will still suffer from process variation, requiring initial calibration, and is not immune to input laser wavelength fluctuation. The second athermal solution using MZI [21] will not be elaborated on since the addition structure increases the small footprint of the ORR and reduces scalability.

2.5.7 Summary of Methods

This chapter provided a comprehensive overview of the MRM thermal control designs. Six different MRM locking techniques have been reviewed. Athermal devices require an initial manual tuning for each ring. Temperature sensors, average power monitoring, and photocurrent sensing all require an initial calibration process to determine the optimal locking point for each ring. Real-time power monitoring requires high-speed electronics, which increases the system's power consumption. Finally, the dithering approach has trouble stabilizing when the input laser wavelength is far from resonance. A method that is entirely calibration-free and can lock under any initial condition is necessary for scalability to facilitate fabrication and implementation processes.

Chapter 3

Proposed Thermal Tuning

This chapter will proposes and describes a new method to thermally tune microrings that is fully analog, calibration-free, and power-independent. The proposed thermal tuner is substantiated through comprehensive simulation and experimental results, validating its effectiveness.

3.1 MRR Control

Before presenting and describing the proposed methodology for controlling MRMs, the dynamics of a passive MRRs are observed to enhance the reader's intuitive understanding of how a controlled double-bus microring operates. MRRs typically have a CW laser as a fixed optical input with a narrow bandwidth and a wavelength denoted as λ_{Laser}. Fig. 3.1 displays an example of the transmission spectrum for the through and drop port of a double-bus MRR. Assume that a single CW laser is coupled into the input of the ring with wavelength λ_{Laser1} as shown in the figure. This figure shows that most of the input laser signal is directed towards the through port, while a negligible amount is directed towards the drop port for that specific input. Now, if the input laser is changed to one with a wavelength of λ_{Laser2}, there will be almost no transmission at the through port; instead,

the majority of the input signal couples to the drop port. This observation shows that the outputs depend on the input laser's location compared to the ring's resonant wavelength.

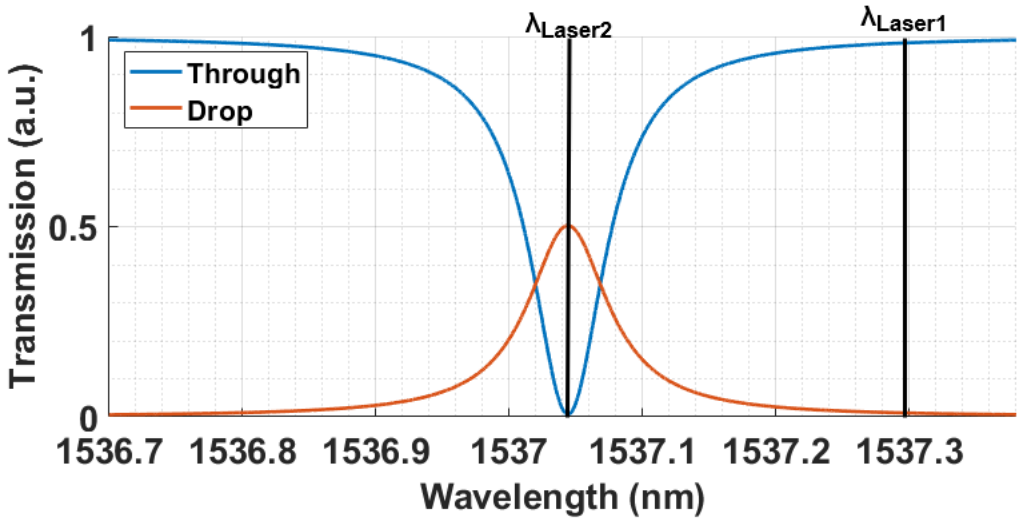

Figure 3.1: Example of Transmission spectrum for a double-bus MRR

In most applications, the input laser is constant. Therefore, the only way to ensure the ring operates at the desired wavelength compared to the input laser is by controlling the resonant wavelength of the ring. This control can be done with the thermo-optic effect by placing an integrated heater near the ring to change its local temperature. In Chapter 2, it was explained that the ring's resonance can be red-shifted (i.e. shifted to the right) by increasing the local temperature, while it can be blue-shifted (i.e. shifted to the left) by decreasing the temperature. This transition is demonstrated in Fig. 3.2. Applying more power to the integrated heater increases the local ring temperature and red-shifts the resonance. Currently, active cooling is not feasible, but a viable alternative is passive cooling, achieved by reducing the power supplied to the heater.

To summarize, the two output powers of a microring are based on the distance of the CW laser input to the resonance. Moreover, the microring's resonance can be controlled by an integrated heater. Therefore, a closed-loop feedback controller can control the ring

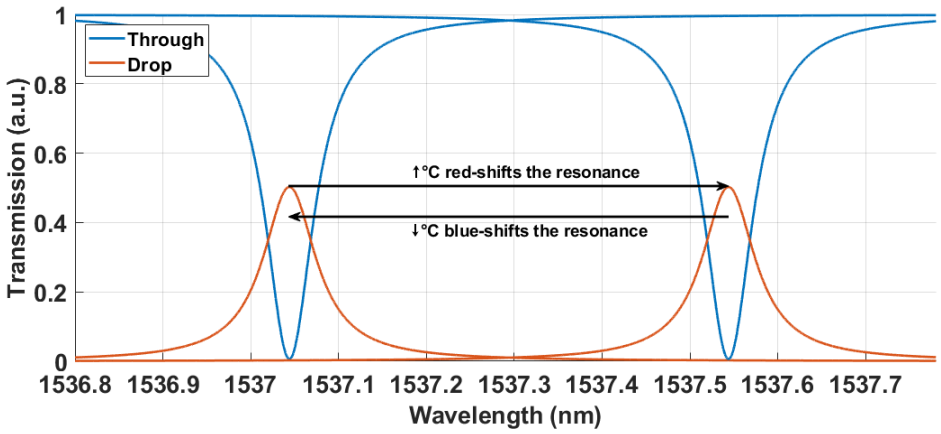

Figure 3.2: Resonance shift base on changes in local temeprature of the ring

resonance based on measurements of the MRR output powers by varying the power to the integrated heater. Based on this, feedback controllers have been successfully implemented, as explained in Chapter 2.

Our proposed method measures the output powers of both the through and drop outputs and subtracts them to obtain an error signal. Fig.3.3 depicts the through minus drop error signal. Observe that the wavelength corresponding to a zero error signal is the point of intersection between through and drop transmissions. This is expected since the error signal is the subtraction of through and drop, and it will only be zero when the through and drop outputs are the same. A monotonic error signal with a zero crossing is obtained. By inputting this error signal into a PID controller that regulates the power supplied to the microheater, the PID controller systematically reduces the error signal to zero. This closed-loop feedback controller locks the MRR operation at the wavelength where the through and drop powers are equal.

This locking method eliminates the need for a reference value or calibration, as the controller obtains the error signal directly from the MRR. While the locking point may not be optimal for MRR filter applications, when employed as a modulator, this method achieves lock at near optimal OMA, as will be demonstrated in Section 3.4.1. Intuitively,

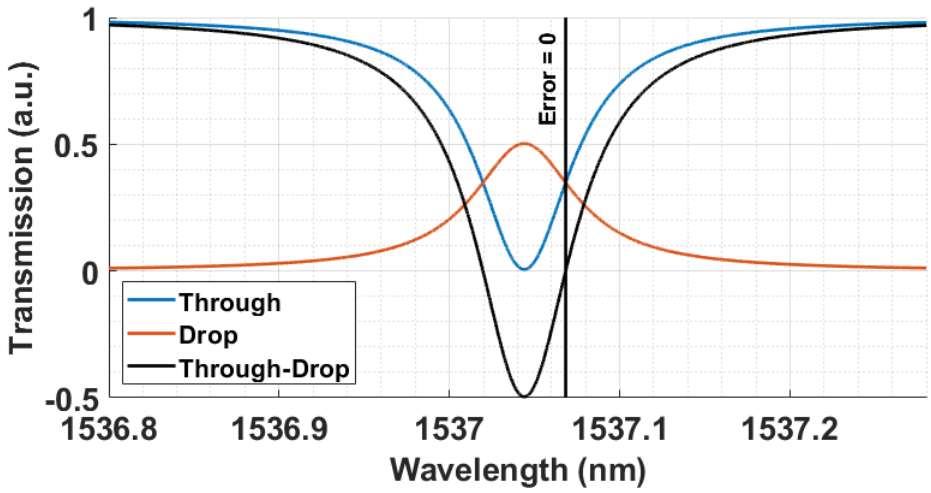

Figure 3.3: Error signal obtain from Through - Drop signal

a high output OMA is achieved by locking at the wavelength on the transmission spectrum where the slope is high, which is the case for the through and drop crossing wavelength shown in Fig. 3.3. In filter applications, different gains can be applied to the through and drop outputs before the subtraction to lock at a more optimal location on the resonance curve.

3.2 MRM Control

The previous section described the basics of the proposed thermal controller for a passive MRR. This same method can also be applied to active MRMs. In this case, the average output powers are obtained and then subtracted. Fig. 3.4(A) depicts the MRM outputs for a biased and non-biased ring. As explained in Chapter 2, a rapid shift in resonance is possible through the electro-optic effect that allows modulation of an MRR. Assuming a high-speed balanced amplitude modulated data is applied to the ring's diode, the ring outputs will spend half the time at the '1' bit or high level (unbiased diode) and the other half at the '0' bit or low level (reverse biased diode). Therefore, the average power of each

output is the middle point between the high and low levels and is plotted in Fig.3.4(B). This assumes a two-level amplitude modulation scheme, such as non-return-to-zero (NRZ) modulation. Any balanced amplitude modulation scheme will have the average power at the middle point; thus, this locking method would still apply. Other modulation schemes will need to be further investigated in future work.

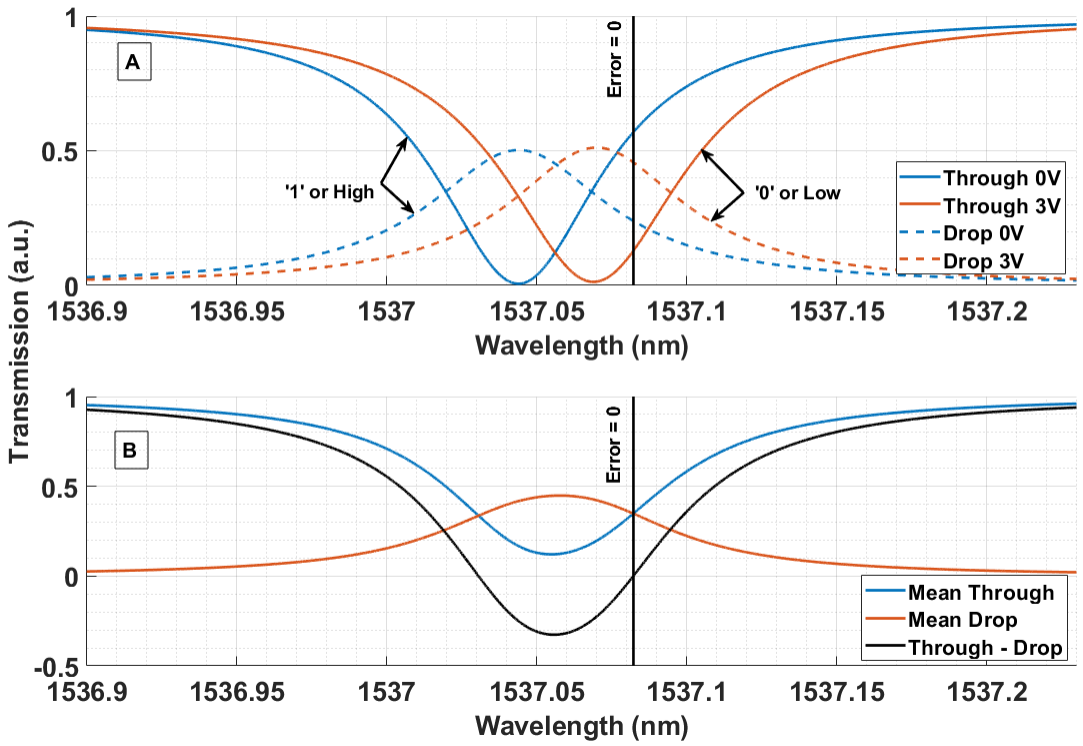

Figure 3.4: (A) Example of through and drop transmissoin spectrum of a double-bus MRM for a biased and non-biased p-n junction and (B) error signal obtained by the difference in average through and drop output powers

Fig. 3.4(B) is very similar to the passive MRR case in Fig. 3.3. The subtraction of the average powers of the through and drop outputs becomes the error signal, enabling a closed-loop PID controller to stabilize the MRM at the operating point where the mean of through and drop ports are identical. Therefore, the proposed thermal controller will stabilize the MRR or MRM at the operating point where the average powers of through and

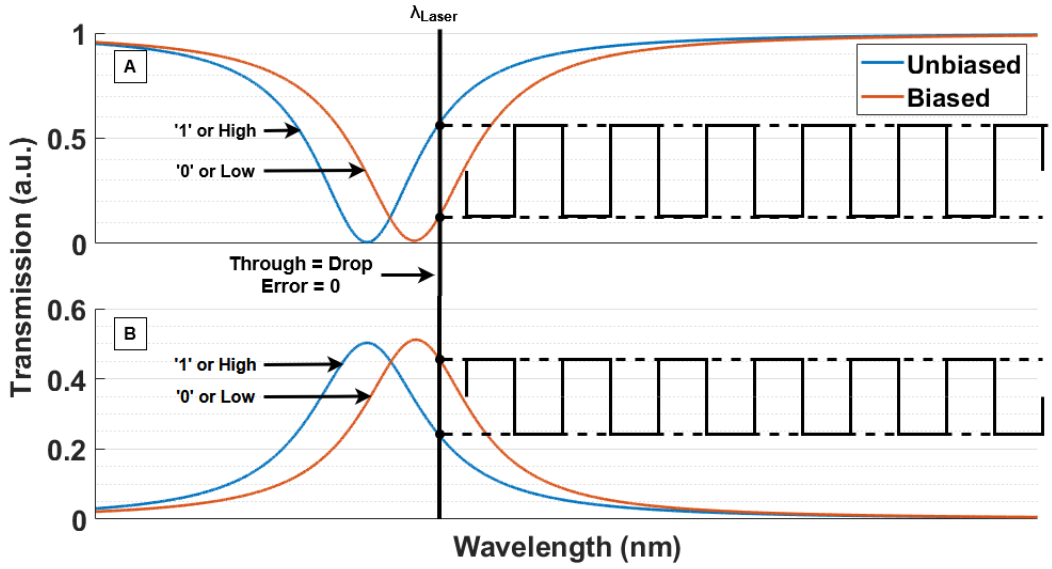

Figure 3.5: (A) Modulated Through Output at locking point and (B) Modulated drop output at locking point

drop are identical.

Figure 3.5 shows the modulated ring outputs under the locking operation of through = drop. Note that the CWL wavelength is constant, and the thermal tuner has already shifted the through = drop wavelength to match the CWL's wavelength, stabilizing it at this point. When the ring's pn diode is not reversed biased, the through output is considered a '1' or high at the locking point. After applying a reverse bias to the pn diode of 3 V, the resonance gets red-shifted due to the plasma dispersion effect. Then, the through output becomes a '0' or low at the locking wavelength. By rapidly alternating between these two states with a high speed voltage applied to the ring's pn diode, the MRM effectively modulates the CW laser.

The ring's output OMA and ER are subject to change depending on the input CWL wavelength compared to the resonance spectrum, as previously seen in 2.4. This highlights the significance of employing a thermal control scheme with an optimal locking point.

3.3 Proposed MRM Thermal Tuner

The block diagram depicted in Figure 3.6 showcases the proposed design for thermal control, requiring a small power tap for both the through and the drop output. These taps are connected to two separate PDs, which convert the optical power signal to electrical current ($i_{through}$ and i_{drop}), serving as the inputs for the thermal controller. Amplification and voltage conversion of these currents are carried out through a low-speed TIA to obtain a voltage representation of the average power at the outputs ($v_{through}$ and v_{drop}). Afterward, the voltage representations of the average powers of the through and drop ports are subtracted, resulting in a monotonic error signal with a zero crossing as previously described (v_{error}). The PID controller drives the error signal to zero by adjusting the voltage applied to the integrated heater (v_{heater}). As the error converges to zero, the MRM stabilizes at the point where the average powers of through and drop become equal.

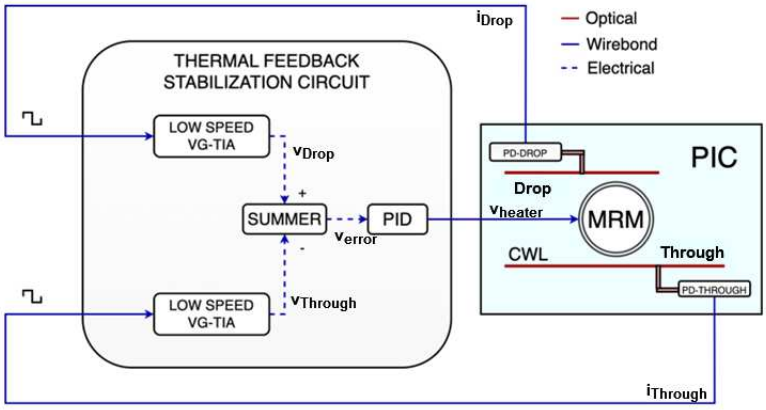

Figure 3.6: Proposed block diagram of the thermal control unit for MRM

A progression from the initial start-up to the operational locking of this design will be demonstrated to gain more insight into the proposed thermal tuner's functionality. Assume that the chosen CWL wavelength is initially far from the fabricated resonance wavelength

of the microring. This assumption is reasonable given the expected variations due to fabrication tolerances and temperature sensitivity of MRRs, which can significantly alter the designed resonant wavelength. Furthermore, the FSR is typically orders of magnitude larger than FWHM, making it probable that the input laser is far from resonance. In addition, the input laser will almost always be to the right of a resonance since the resonance is periodic. For instance, when the laser is positioned to the left of a resonance, it will also find itself to the right of the preceding resonance that is separated by an FSR.

Fig 3.7(A) depicts the initial conditions of the ring for this scenario. In this figure, most of the optical power is transmitted to the through port since λ_{Laser} is far from resonance. A positive error signal, resulting from the difference between the through and drop average powers, prompts the PID controller to apply power to the heater. This action increases the local temperature of the ring, leading to a red-shift in the ring's resonance due to the thermo-optic effect. As the local temperature increases, the error signal gradually decreases near resonance, as depicted in Fig. 3.4. The PID controller increases the heater power until the error signal exponentially decays to zero and locking is achieved.

3.3.1 Regions of Operation

The thermal control can behave differently depending on the initial wavelength of the CWL, λ_{Laser}. Separating the resonant spectrum into three distinct regions will allow for a better understanding of these different behaviors. Figure 3.8 shows three regions where the error signal changes polarities. Note that two locking wavelengths exist where the error signal equals zero; however, only the rightmost one results in negative feedback when implementing a $Through - Drop$ configuration. The subtraction can be reversed to achieve locking on the opposite side, employing a $Drop - Through$ controller. The subsequent section assumes a $Through - Drop$ error signal.

The error signal is positive in regions A and C; therefore, when λ_{Laser} is inside those

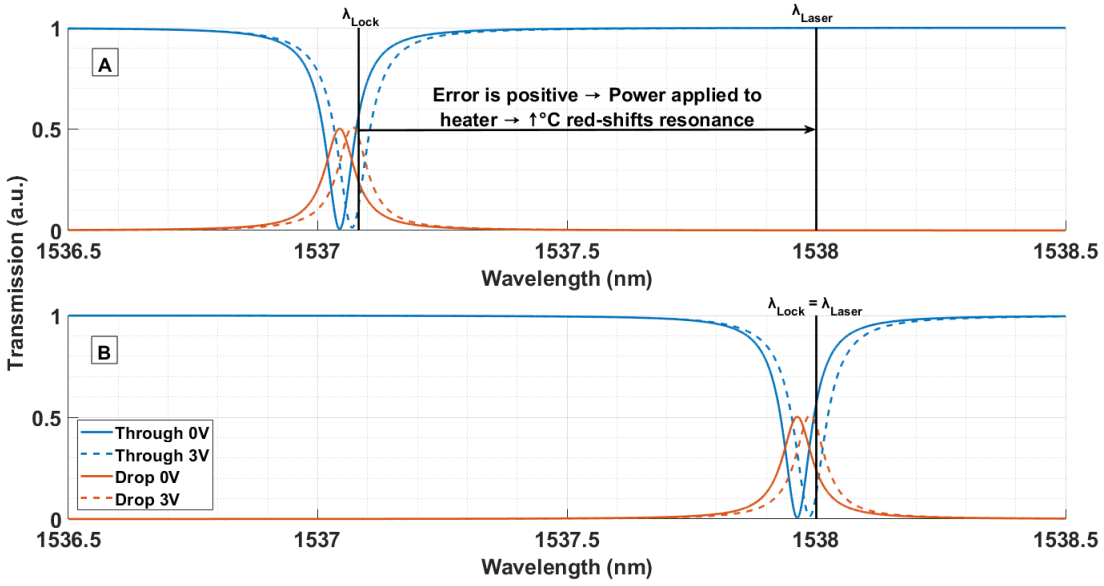

Figure 3.7: (A) Example of an initial conditions of MRM at start-up abd (B) Final MRM locked at through = drop

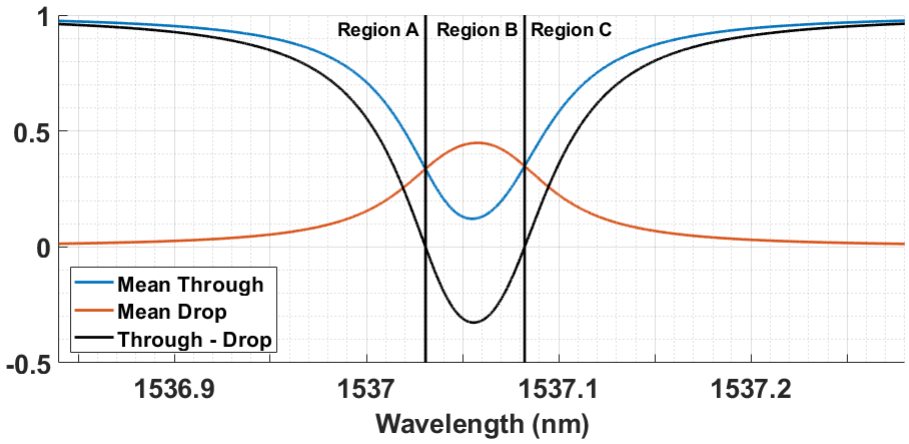

Figure 3.8: Through - drop error signal divided into three distinct regions

regions, the control loop will apply power to the heater, shifting the resonance spectrum to the right (red-shift). If the CWL wavelength is in region C at start-up, the local temperature of the ring will increase until it reaches the locking point. If the CWL wavelength is in region A at start-up, the local temperature of the ring will increase until it reaches the locking point of the next FSR. The further to the right the CWL is from the locking point,

the more power will be consumed by the thermal control to keep the ring locked.

Region B is very different. In this region, the error signal is negative; thus, the control loop will try to decrease the power applied to the ring, which passively cools the ring and blue-shifts the resonance. If the CWL is initially in region B, the power applied to the thermal heater will be zero, and it will be impossible to cool the MRM since no power is applied to the ring. Active cooling is impossible with the integrated heater design, only more or less heat. Therefore, the CWL wavelength must not be in region B at the system's initial start for this feedback design. Fortunately, region B accounts for a tiny percentage of the possible regions, and chances are that this will not occur. However, simple modifications to the current design can eliminate this risk and is presented in section 3.4.4.

This loss of lock does not occur if the CLW wavelength fluctuates into this region during locking operation since the negative error signal tells the controller to provide less power to the heater and passively cool the ring. Passive cooling works because the thermal control was already applying a non-zero power to lock the ring during the wavelength fluctuation.

Finally, the upper limit of tuning range of the thermal control will depend on the maximum power that the control loop can supply without damaging the ring and the thermal efficiency of the design. Furthermore, the lower limit will depend on the initial distance between λ_{Laser} and the lock point at the start of the system. For example, if the external temperature decreases substantially, the thermal control will apply considerable power to the ring and is limited by the maximum power the thermal heater can handle without damage. On the other hand, if the external temperature increases significantly, the power applied to the thermal heater might reach zero, and the control loop will lose its locking point. Section 3.4.4 will provide a solution to the lower limit.

In conclusion, only a finite tuning range exists for this control design. However, if the control can tune for a full FSR before reaching the upper limit, it will always have a locking point. Moreover, there is no need for calibration when using this locking method.

3.4 Simulation Results

This section provides a detailed description of the simulation results for the thermal control design for an MRM. These simulations have been performed using Simulink and Matlab. The model for the ORR used is a Lorenztian approximation from a designed double-bus ORR measured in the laboratory. The transmission spectrum for this has already been shown in Fig. 3.4(A). The model has also incorporated the PD, TIA, subtractor, and PID. Furthermore, nonlinear voltage-to-power and linear power-to-temperature conversion models were also included. The final model is shown in the Appendix.

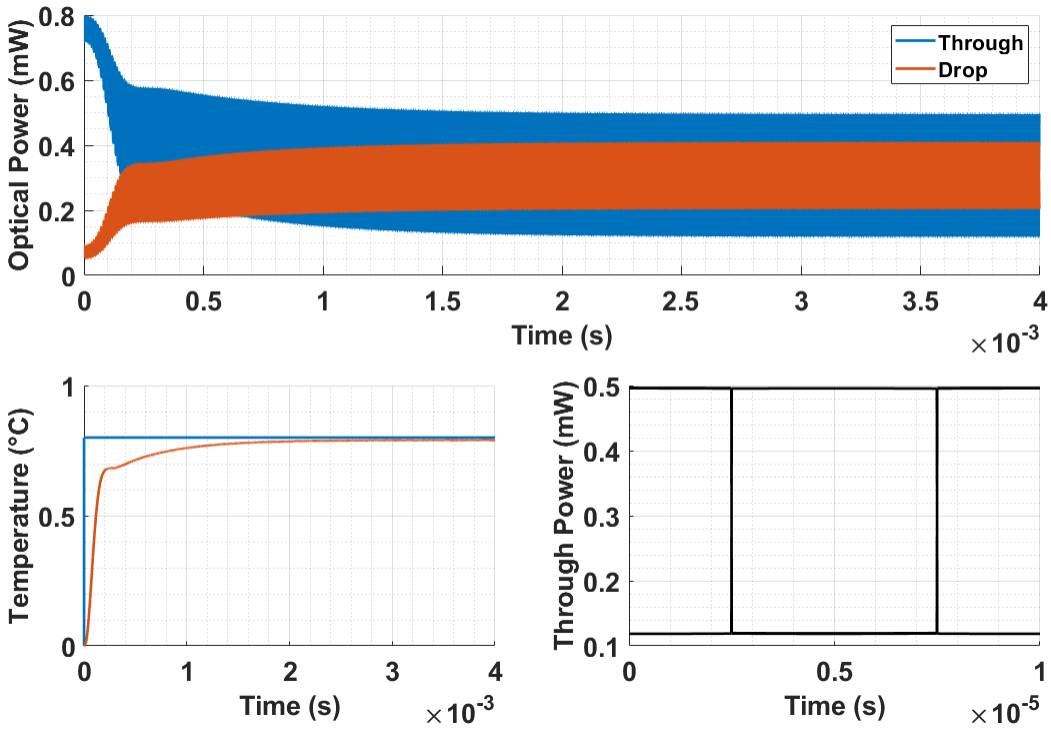

Figure 3.9: Initial simulation results for the proposed control scheme

The ORR model has four inputs: the localized ring temperature, the modulating signal, the CWL wavelength, and the CWL power. Figure 3.9 shows the results for a $3\ V$ modulation amplitude where the ORR is initially far from a lock in region C. The top graph shows

that the thermal tuner stabalized the MRM at the wavelength where the through and drop average powers are equal, as previously mentioned. The last plot shows the through output eye diagram for the locked MRM. In order to decrease the simulation time, slower modulation speeds were utilized during the simulation process, which accounts for the sharp rise and fall times of the eye diagram. These initial simulation results validate the proposed thermal control design. The following subsections will have a more detailed analysis of these results.

3.4.1 OMA and ER

Figure 3.10 compares the two locking points of the proposed control with the optimal OMA and ER as a function of modulation voltage. The modulation voltages are applied at the pn diode of the MRM in a reverse-biasing configuration. The graph shows that the right locking point performs slightly better than the left. In addition, the through OMA, drop OMA, and drop ER are near optimal, but the through ER is nowhere near the optimal ER, as seen in Table 3.1. In shorter-reach applications, the OMA is essential, validating this design. Additionally, the OMA increases when the output signal is taken differentially since the through and drop combine. In longer-reach applications, ER becomes critical, which is not favorable for this design. In this case, the drop port should not be transmitted since the output with the smallest ER limits the maximum allowed transmission distance. Although the ER is closer to optimal for the drop output than the through output, the through output still has a higher ER, enabling it to be transmitted over longer distances despite propagation losses.

Table 3.1 reports the percentage ratio between the simulated and optimal OMA and ER for different diode-basing voltages. These results demonstrate that the wavelength locking point is at the optimal OMA for 2 V modulation and higher.

Figure 3.11 shows the OMA and ER for different modulation amplitudes as a function

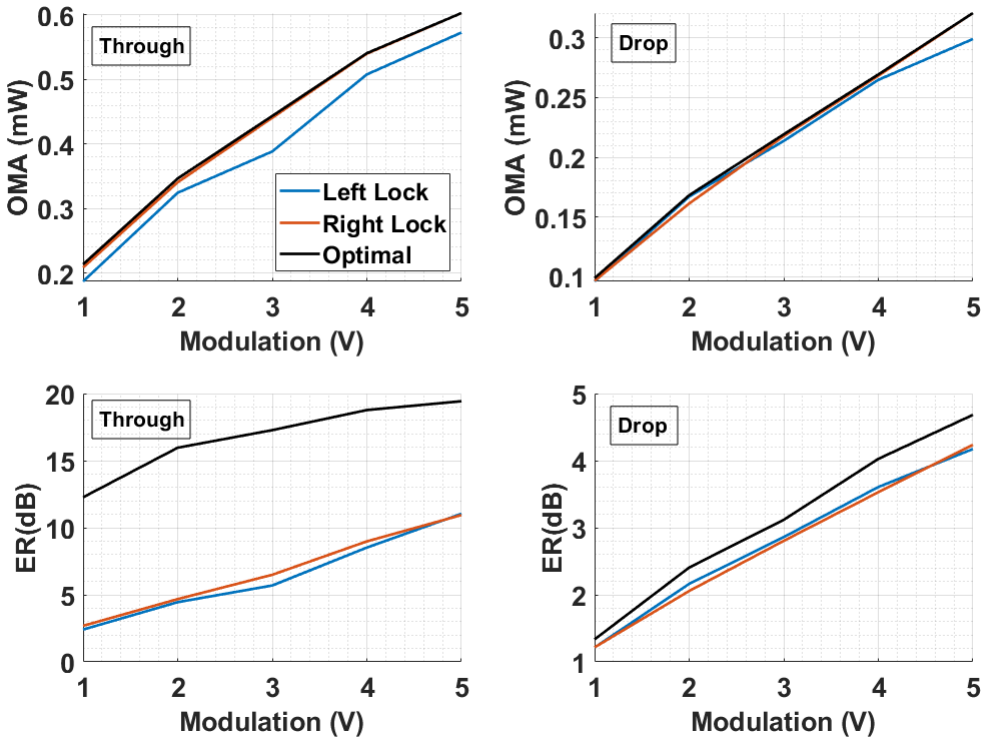

Figure 3.10: Optimal and locking point OMA and ER as a function of modulation amplitude

Table 3.1: Locking point OMA and ER comparison to their optimal values for different biasing voltages

Modulation (V)	$\frac{DesignOMA}{OptimalOMA}(\%)$		$\frac{DesignER}{OptimalER}(\%)$	
	Through	Drop	Through	Drop
1	97.7	97.7	21.9	91.1
2	98.3	95.9	29.3	85.5
3	99.4	99.3	37.6	89.9
4	99.9	99.6	47.9	87.7
5	100	100	56.3	90.5

of wavelength near resonance. The -2 V implies a modulating voltage between 0 and -2 V applied to the MRM's pn diode. The negative sign signifies a reverse-bias pn junction. This graph allows for a more visual comparison of the different locking points. Note that the optimal OMA and ER are not in the same location, so no method allows simultaneous

locking at the optimal point of both.

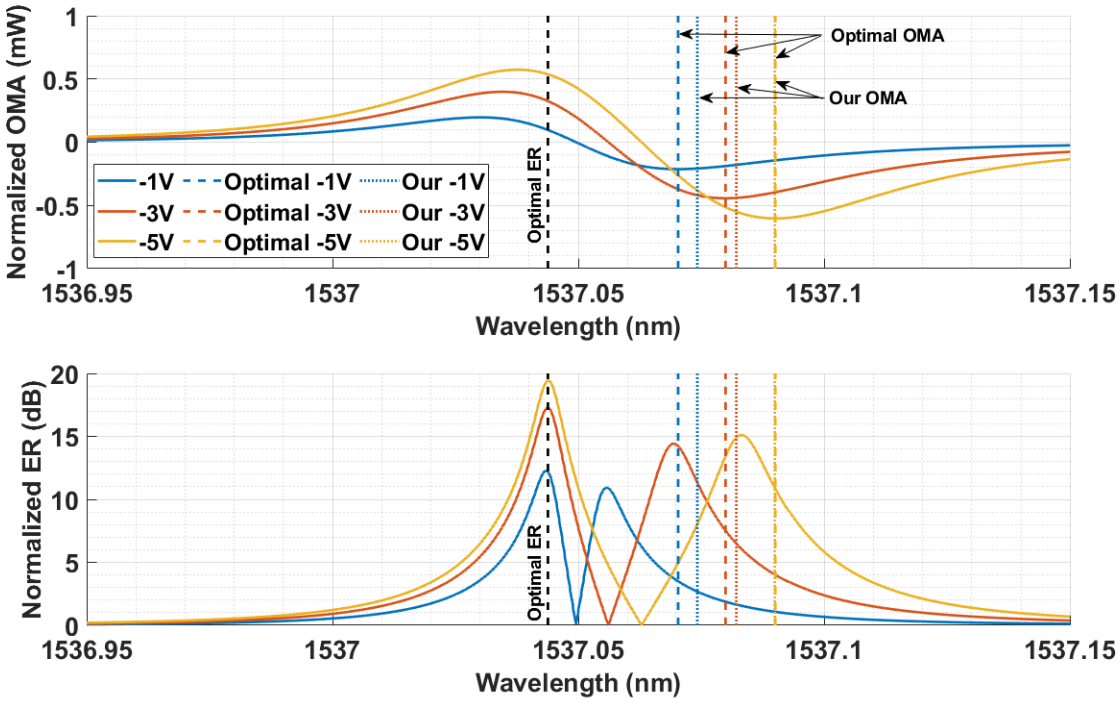

Figure 3.11: OMA and ER as a function of wavelength at resonance

A possible solution to increase the ER for longer-reach applications is reducing the drop TIA gain compared to through TIA gain before the subtraction. This will reduce the average power of the drop output in Fig. 3.8, and therefore, the crossing between the through and drop averages will be approaching the minimum of the through average where the ER improves. Furthermore, if the subtraction is $Drop - Through$, the microring locks on the left side where the ER is larger, as seen in Fig. 3.11.

3.4.2 Stabalizing Thermal Variations

Any temperature fluctuations for an MRM that does not utilize a thermal control will result in data loss. An MRM will typically be used in thermally volatile environments with adjacent microelectronics. Hence, the most crucial feature of any thermal control design

for MRM is to accurately control the local ring temperature to ensure a stable locking point against any external influence. The following simulation will show stable operation against an oscillating external temperature.

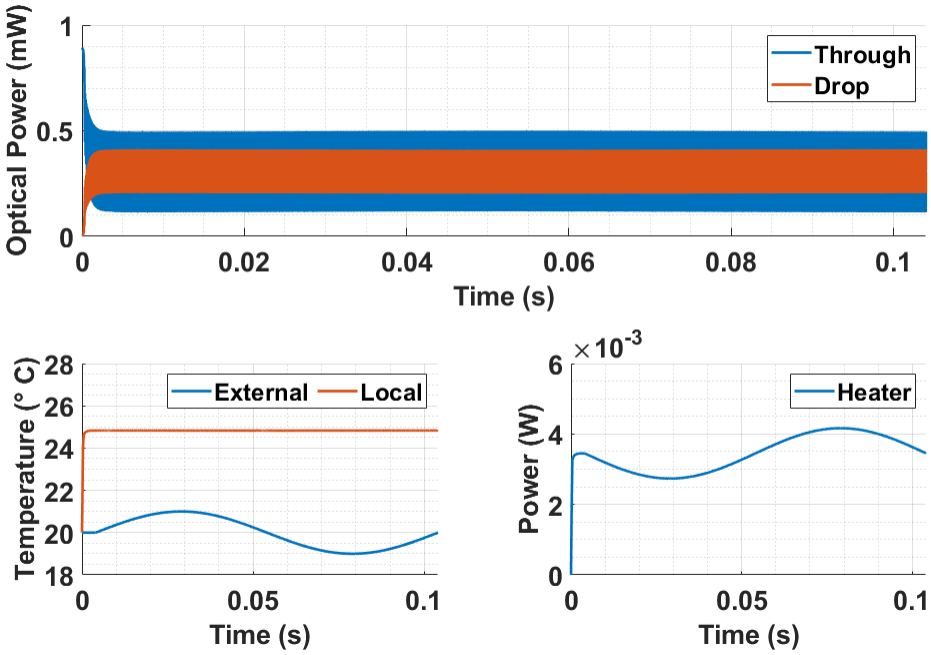

Figure 3.12: Simulation results for an oscillating external temperature

In this simulation, the external temperature in the ring's model varies with an oscillation of 10 Hz. Fig. 3.12 reveals the results obtained. In the first couple of milliseconds, the control stabilizes the ring by increasing the local temperature since the laser wavelength is initially far from a lock. Once locked, the oscillation of the external temperature starts. The local temperature does not change since the power applied to the heater compensates for the external fluctuation, as seen in the results. Furthermore, the through and drop means also remain constant during the simulation.

This simulation validates that this wavelength control can be stabilized against external temperature variations. The maximum speed of external temperature variations that the thermal tuner can compensate for is constrained by the integrated heater's time constant,

which is determined by the slower response time between active heating and passive cooling. In addition, a fluctuation in the input laser wavelength behaves similarly to a change in temperature since temperature changes shift the resonant wavelength. Therefore, this design also regulates against changes in laser wavelength. The temperature sensor and athermal ORR control designs described in Chapter 2 are not immune to these laser wavelength changes. One measures the temperature around the ring instead of the power, and the other has no wavelength control.

3.4.3 Immunity to Laser Power

As mentioned in Chapter 2, the input laser of the ring is not necessarily stable. Changes in the temperature of the laser might lead to fluctuations in its power. Immunity to the laser power fluctuation is preferred in MRMs to maintain locking throughout its operation. Control schemes that lock to a reference value will not be power-independent since the reference value is based on the output power, which varies with laser power. The proposed control locks to the difference between the through and drop powers, where the change in power at both outputs due to laser fluctuations will cancel out.

To demonstrate this, Fig. 3.13 displays a simulation of the MRM where the input power of the laser varies with time. The control locks the ring in the first millisecond since the input laser wavelength is not at the locking point. Locking is achieved when the mean of the through and drop power becomes equal. As the laser power changes, the output power will also vary. However, the difference in through and drop mean power remains unchanged throughout the simulation. Thus, the thermal control maintained the locking point as the laser power changed, making this design power-independent.

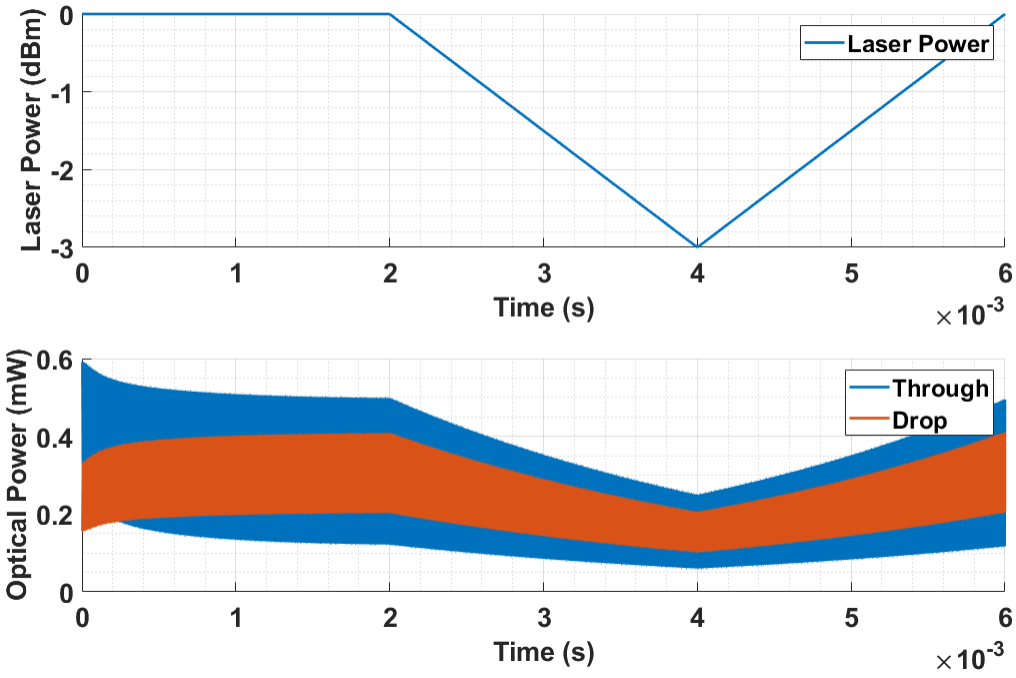

Figure 3.13: Stable locking while varying the input power by -3 dBm

3.4.4 Calibration Free

As the number of ORRs increases, thermal control schemes requiring initial calibration, such as [9], will have a more complex manufacturing process, making it less scalable. Calibration-free MRMs are desired to ease the manufacturing process and increase scalability.

The previous simulations began with the laser wavelength in region C of Fig 3.8. When the MRM is powered on, laser wavelengths in either regions A or C have positive error signals and thus behave similarly. The only distinction between the two regions is that the locking point in Region A is located at the resonance of the next FSR. As mentioned in section 3.3.1, a locking issue arises when the laser wavelength is in region B when the MRM is turned on with this control scheme. In this section, the error signal is negative and tries to cool the ring passively, but at launch, the heater's power is zero and cannot

passively cool the ring by providing less power.

This problem also occurs when the ring is locked correctly, and the external temperature increases until it reaches the local ring temperature. When the local ring and external temperatures are the same, heater power becomes zero, and passive cooling is impossible. This case is depicted in Fig 3.14.

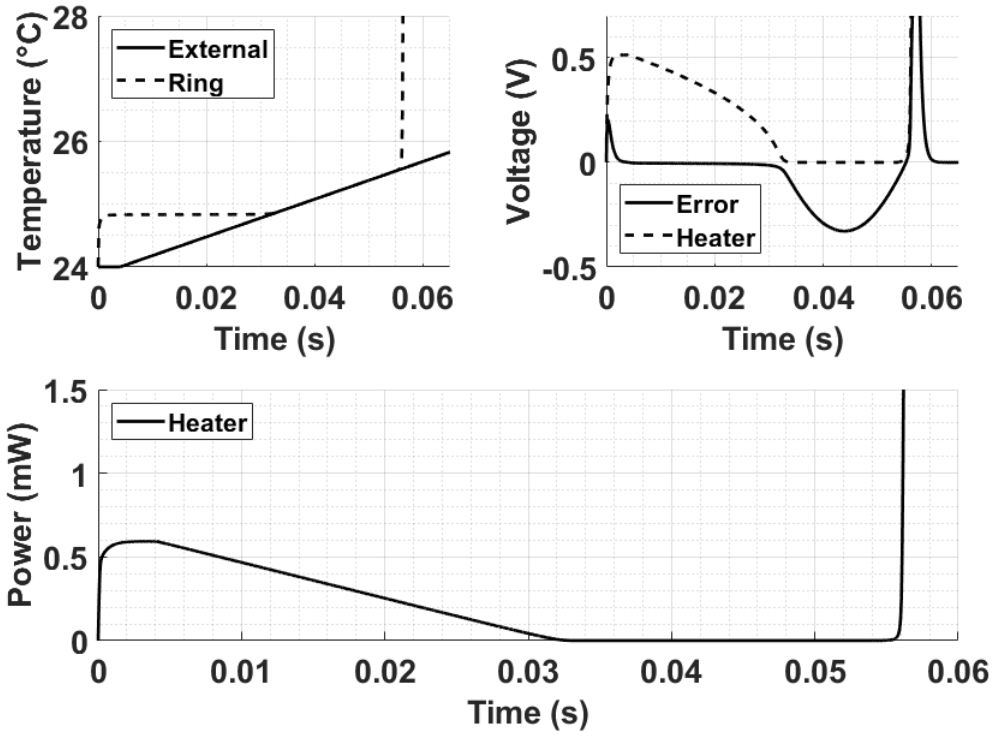

Figure 3.14: Simulation for loss of lock due to heater power reaching zero while error signal is negative

This simulation begins when the laser wavelength is in region C, and the control loop accurately locks the ring. As the external temperature increases, the ring remains locked until the external temperature matches the locked ring temperature. At this point, the voltage applied to the heater becomes zero, and passive cooling is no longer possible. As a result, the laser wavelength shifts into region B, and the error signal turns negative; attempting to cool the ring but cannot since the heater power is zero. Consequently, the controller can

no longer keep the ring locked. The condition for this to occur is that the heater power must be zero and the error signal negative, which only happens when the laser wavelength is in region B. Finally, the error becomes positive once the external temperature increases further and red-shifts the resonance past the laser wavelength. The positive error tells the control to heat the ring until the laser is locked at the next FSR, where the error goes to zero, as seen in the graph.

The possibility for this to occur is slim since region C is much smaller than the full FSR, but since it is possible, this design cannot claim to be calibration-free for every manufactured ring. Process variation might shift the designed resonance to the laser wavelength desired. In addition, the laser might be located in region C but near region B, and only a slight increase in the temperature of the ring's environment might lead to the loss in the locking of the ring. The MRM should lock itself under any initial condition to claim a calibration-free thermal controller.

A potential solution to this problem is to apply negative voltages to the microring's heater. The initial design assumes the final PID stage only supplies current to the integrated heater by applying positive voltages. However, it can also sink current by applying negative voltages. A negative voltage increases the ring's power dissipation since the voltage is squared to obtain power. Therefore, when the heater voltage is negative, a positive error results in a decrease in local ring temperature, while a negative error leads to an increase in local ring temperature. In other words, the polarity of the error signal is flipped from $Through - Drop$ to $Drop - Through$. Consequently, the new locking point is on the left of the ring spectrum depicted in Figure 3.8 when the laser wavelength is located in region B.

Fig. 3.15 illustrates the same simulation as Fig. 3.14 except the PID can now sink current by applying negative voltages to the heater. The simulation starts the same as before, but once the ring and external temperature are equivalent and power reaches zero,

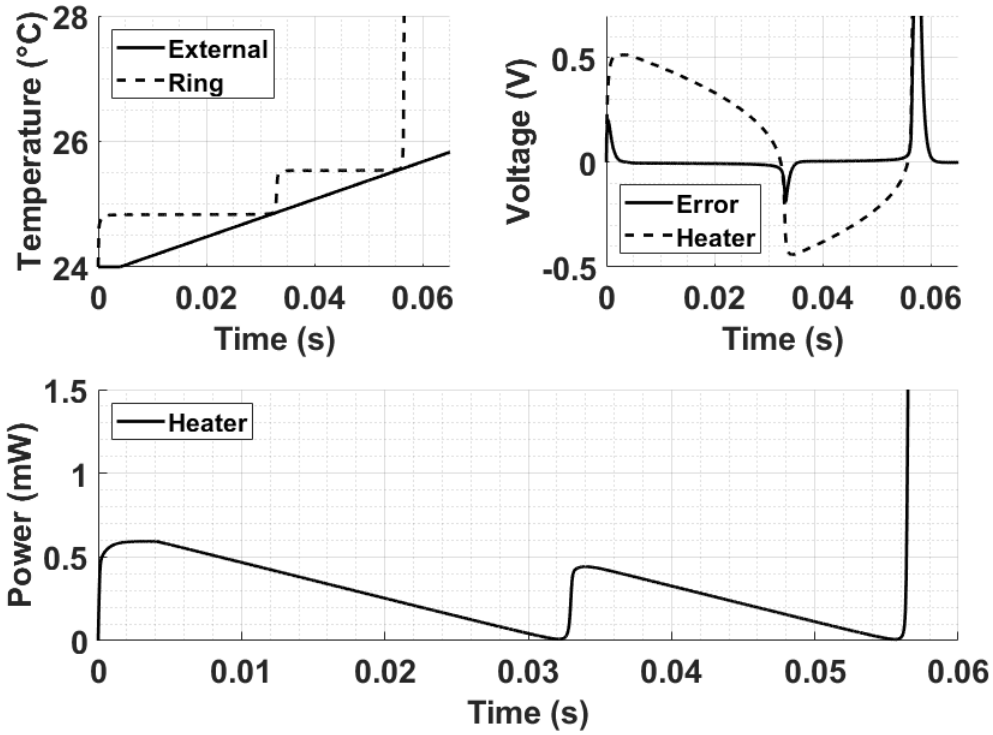

Figure 3.15: Simulation for calibration-free thermal control design

a negative voltage is applied to the heater. The locking wavelength changes to the left of the resonance in Fig. 3.8 and stabilizes there for any laser wavelength in region B. When the external temperature exceeds the second operating temperature, heater voltages become positive again, and the ring locks to the next FSR.

Fig. 3.16 compares the output optical powers of the two simulations described earlier. The results can be divided into three distinct regions based on the location input laser wavelength. It starts in region C, moves into region B, and finishes in region A due to external temperature changes. Both simulations start the same and lock to the same operating point. Once the laser enters region B, the top graph is no longer locked, and the data is lost. However, the bottom graph shows that the controller finds the new locking point, and the data is not lost. Finally, when the laser enters region A, both cases lock the ring to the next FSR, and data is not lost.

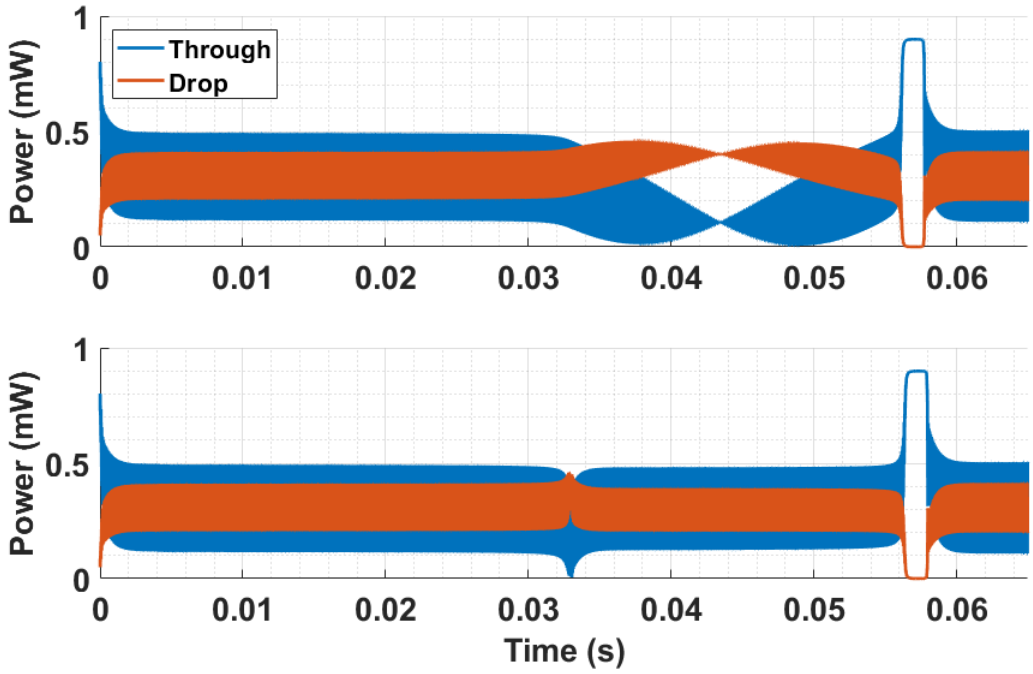

Figure 3.16: (top) Through and Drop optical powers when heater only has positive voltages and (bottom) when heater can have negative voltages

This solution solves the conditions where the MRM loses its operating point. Now, independent of any initial or operating conditions, the controller will always find an optimal operating point to stabilize the ring.

3.4.5 Loop Stability

To ensure a stable system, it is necessary to perform a loop analysis of the thermal controller. However, this can be a challenging task due to the nonlinearity of both the MRM and thermal heating systems. To overcome this difficulty, linearizing the system around the locking point will help us analyze for loop stability. The simplified control loop model is shown in Figure 3.17, where it is worth noting that the input is the external temperature and not the modulation voltage. This is because the thermal loop controls the temperature, not the modulation voltage. For the purpose of this analysis, the modulation

input is assumed to be zero (non-biased ring).

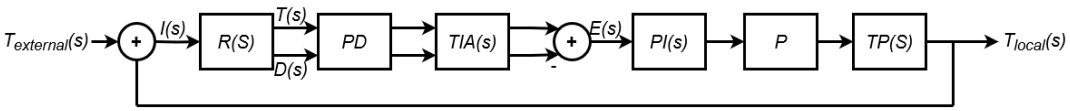

Figure 3.17: Model of the thermal feedback control for loop stability analysis

In Figure 3.17, R(s) is the linearized transfer function of the MRR, PD represents the transfer function of the PD, TIA(s) denotes the transfer function of the TIA, PI(s) is the proportional-integral (PI) controller's transfer function, P is the linearized transfer function of the conversion of the voltage applied to the heater to the power dissipated by the heater, and finally, TP(s) is the conversion of the power dissipated to the localized temperature of the ring. Only a PI controller is implemented in this research, so the derivative term is zero for the PID controller. The PI gain selection needs to be carefully chosen to ensure closed-loop stability; therefore, the gain and phase margin should be analyzed from the loop gain of the system. The equations for each transfer function are shown below, except for the MRR, which will be discussed in detail next.

A PD has an output current proportional to the input optical power based on the proportionality constant R_{PD}, which stands for responsivity and is shown in eq. 11. Note that this equation should have a pole, but it can be ignored and will be explained why later. The TIA is modeled as a simple low pass filter where the gain, R_{TIA}, would be the TIA's feedback resistor, and the cutoff frequency, ω_1, is the cutoff frequency of the TIA.

Eq. 13 is found taking the derivative of $p = \frac{V^2}{R}$ at the point where $V = V_0$. This is to linearize the power voltage relationship at the lock point. V_0 is the locking point voltage applied to the heater, and R is the resistance of the heater. In eq. 14, R_θ is the absolute thermal resistance of the heater, and ω_2 is the reciprocal of the thermal time constant of the ring. Finally, in eq. 15, K_p stands for the proportionality constant, and K_i the integral constant.

$$PD = R_{PD} \tag{11}$$

$$TIA(s) = \frac{R_{TIA}}{1 + \frac{s}{\omega_1}} \tag{12}$$

$$P = \frac{2V_0}{R} \tag{13}$$

$$TP(s) = \frac{R_\theta}{1 + \frac{s}{\omega_2}} \tag{14}$$

$$PI(s) = \frac{K_p s + K_i}{s} \tag{15}$$

The ring's transfer function needs special attention since the input is temperature, and the output is optical power. Therefore, the ring transfer function combines two different transfer functions. It was mentioned in Chapter 2 that temperature variations shift the resonant wavelength of the MRR. This converts the temperature at the input to wavelength, denoted from now on as $R_1(s)$. Finally, the shift in the resonant spectrum changes the optical power at the output. This is the conversion from the wavelength to optical power, denoted from now on as $R_2(s)$. The first conversion has a linear relation, but the second one is nonlinear due to its Lorentzian function model. To linearize $R_2(s)$ around the lock point, the derivative of the Lorentzian functions for the drop and thorugh spectrums need to be found and are shown in 18 and 19 respectively. In these equations, P_{max} is the peak power of the resonance spectrum of the drop output, P_{min} is the minimum power of the resonance spectrum of the through output, λ_{res} is the resonance wavelength of the spectrum, $FWHM$ is the full width at half maximum of the spectrum, λ is the wavelength of the CWL input. Finally, L is the insertion loss of the ring.

$$Drop(\lambda) = \frac{P_{max}}{1 + (\frac{2(\lambda - \lambda_{res})}{FWHM})^2} \tag{16}$$

$$Through(\lambda) = L - \frac{(L - P_{min})}{1 + (\frac{2(\lambda - \lambda_{res})}{FWHM})^2)} \tag{17}$$

$$\frac{\partial Drop}{\partial \lambda_{res}} = \frac{8P_{max}}{FWHM^2} \frac{\lambda_{lock} - \lambda_{res}}{(1 + (\frac{2(\lambda_{lock} - \lambda_{res})}{FWHM})^2)^2} = m_d \tag{18}$$

$$\frac{\partial Through}{\partial \lambda_{res}} = \frac{-8(L - P_{min})}{FWHM^2} \frac{\lambda_{lock} - \lambda_{res}}{(1 + (\frac{2(\lambda_{lock} - \lambda_{res})}{FWHM})^2)^2} = m_t \tag{19}$$

The derivative of a function at a point is simply the slope of the function at that point, so $\mathrm{m_t}$ and $\mathrm{m_d}$ in eq. 19 and 18 are the slopes of the Lorentzians at the lock point. $\mathrm{R(s)}$ is now given in eq. 20 and 21. Note that through and drop will have different transfer functions due to having different Lorentzian representations, so $\mathrm{R(s)}$ is given a subscript based on the output. In addition, $\mathrm{K_{to}}$ represents the proportionality constant of the temperature to resonant wavelength shift due to the thermo-optic effect.

$$R_t(s) = R_1(s)R_{2t}(s) = K_{to}m_t \tag{20}$$

$$R_d(s) = R_1(s)R_{2d}(s) = K_{to}m_d \tag{21}$$

Now, we have all the transfer functions required to determine the loop gain. First, the simplified transfer function from $\mathrm{I(s)}$ to $\mathrm{E(s)}$ is shown in eq. 22 where $\mathrm{I(s)}$ is the input of the model.

$$\begin{aligned} \frac{E(s)}{I(s)} &= [R_t(s) - R_d(s)]TIA(s)\,PD \\ &= K_{to}(m_t - m_d)R_{PD}\frac{R_{TIA}}{1 + \frac{s}{\omega_1}} \end{aligned} \tag{22}$$

Before going into the final loop gain, a comparison of the eq. 22 and simulation results will increase the confidence in this equation. A Simulink model of the ring, PD, TIA, and subtractor was simulated to determine the final transfer function of the system, and the model is included in Appendix A. The ring parameters ($K_{to} = 0.074\frac{nm}{^\circ C}, \lambda_{res} = 1537.044nm, \lambda_{lock} = 1537.067nm, FWHM = 0.07nm, P_{max} = 0.503mW, P_{min} = 0.0062mW$) were chosen directly based on experimental results presented later in section 3.6.1. Figure 3.18a presents the simulation results. From this graph, the gain and bandwidth of eq. 22 can be found and compared to the results from the derived equations. The slope of this transfer function was simulated to be $-1.95\ \frac{\mathrm{V}}{^\circ\mathrm{C}}$. Inputting these same parameters into eq. 22 will obtain a gain of $-2\ \frac{\mathrm{V}}{^\circ\mathrm{C}}$. It can be seen that these values are very similar, providing confidence in eq. 22. Note that since the local temperature of the ring is the addition of the ambient temperature and heater temperature, the negative sign obtained from the slope is what leads to negative feedback.

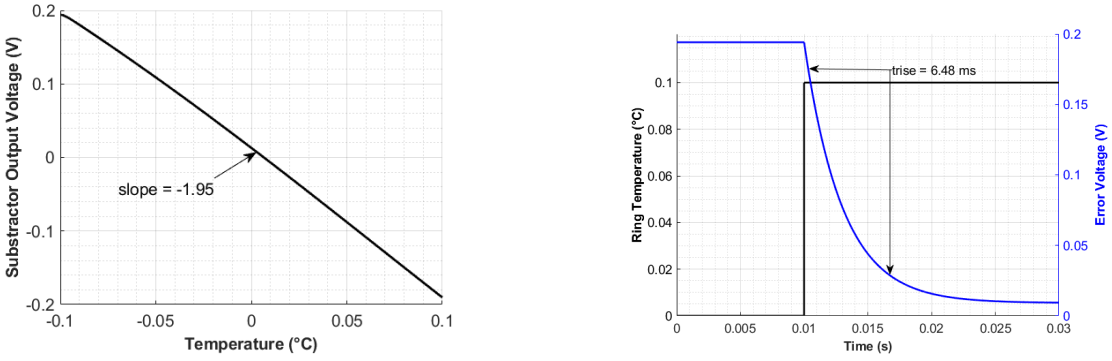

(a) (b)

Figure 3.18: Simulated results of the transfer characteristics from the input to the error signal, $\mathrm{Resp} = 0.0008\ \frac{\mathrm{A}}{\mathrm{mW}}$ and $\mathrm{G} = 1250\ \frac{\mathrm{V}}{\mathrm{A}}$

Note that the poles of the MRR and PD have been ignored in eq. 22. This is because the TIA measures the mean and, therefore, has a much slower response, making it a dominant pole compared to the MRR and PD. This can also be seen in Figure 3.18a. The 3 dB bandwidth of the function can be determined from the rise time simulated in the graph.

The relationship between a 10-90 % rise time and 3 dB bandwidth for single pole low pass filters can be easily derived and is $\omega_1 \approx \frac{2.2}{t_{rise}}$. This leads to a bandwidth of $339\ \frac{\text{rad}}{\text{s}}$. In the Simulink model, the TIA's time constant ω_1 was chosen to be $0.003\ \frac{\text{rad}}{\text{s}}$. Therefore, since the poles of the PD and MRR are much higher than the TIA's, the system's bandwidth is very close to the TIA's bandwidth. These results validate eq. 22. Finally, the open loop gain is shown in eq. 23.

$$\begin{aligned} H_{OL} &= \frac{E(s)}{I(s)} PI(s) TP(s) P \\ &= K_{to}(m_t - m_d) R_{PD} \frac{R_{TIA}}{1 + \frac{s}{\omega_1}} \frac{K_p s + K_i}{s} \frac{2V_0}{R} \frac{R_\theta}{1 + \frac{s}{\omega_2}} \end{aligned} \tag{23}$$

From eq. 23, it can be seen that the system has 3 poles and 1 zero. The PI controller needs to be tuned for an optimal response. This linearized model has been inserted in Simulink with the same ring parameters used in this section. There are many different ways to determine the optimal PI. The Ziegler-Nichols PID tuning was first used, but better results were obtained using Simulink's automated PID tuner. The derivative term was ignored since it does not behave well with noisy systems. Figure 3.22a illustrates the root locus of the controller. In this figure, the closed-loop poles remain on the left half of the complex plane (the real part of the poles remains negative), ensuring this negative feedback is stable for any loop gains. Figure 3.22b depicts the bode plot of the system. In order to enhance the phase margin, the TIA pole was increased compared to the configuration depicted in Figure 3.18b. This adjustment ensures the dominance of the ring's heating pole. Notably, in the bode plot, the PI's zero is positioned close to the heater's pole, resulting in a canceling effect. This, in turn, contributes to a heightened phase margin.

Table 3.2: Step response results

Rise Time (ms)	Settling Time (ms)	Overshoot (%)
0.36	2	6.8

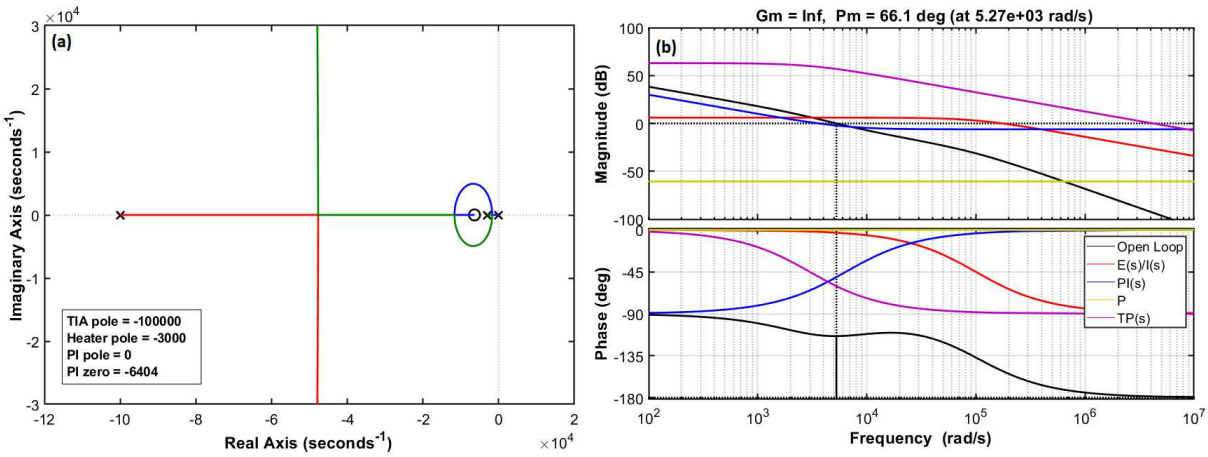

Figure 3.19: (a) Root locus of controller and (b) Bode plot of the open loop transfer function

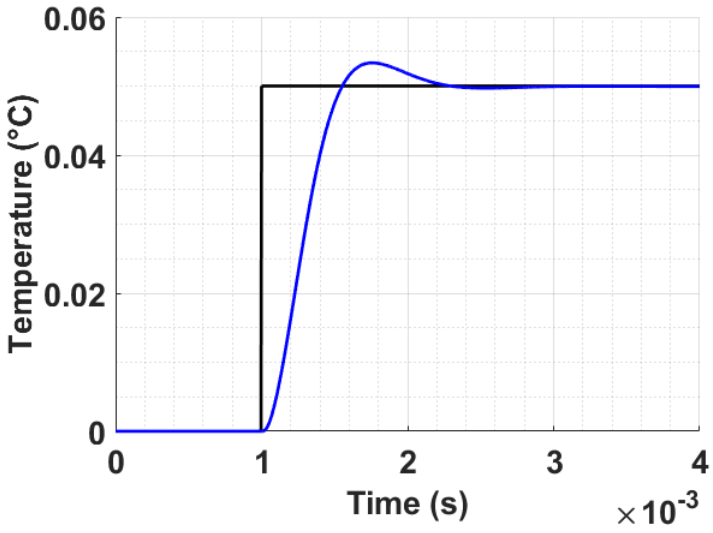

Figure 3.20: Simulated step response of designed thermal feedback control

Figure 3.20 shows the response of the nonlinear Simulink model with the Lorentzian resonance spectrum for a small input step.This shows a stable response to small steps near the lock point, but how does it behave for large inputs where nonlinear effects can greatly impact the system? Figure 3.21 shows that the system becomes unstable for large input steps. Notice that the overshoot changes shape as the input increases. This is due to the second lock point on the left of the resonance explained in section 3.3.1. The overshoot

is based on percentage; therefore, an increase in the input step leads to an increase in the overshoot. Once the overshoot is too large, the system reaches the second lock point and can even pass into region A of Figure 3.8. Once in region A, the control loop now applies heat to the ring and will attempt to lock at the next FSR. This will repeat until the system saturates, making the system unstable. This means that the most important system parameter for this feedback loop is the overshoot of the response. Therefore, the percentage overshoot must be smaller than the temperature difference between lock points over a full FSR. This yields eq. 24 where the $\Delta \mathrm{T}_{\mathrm{lock}}$ is the temperature difference between the two lock points and $\Delta \mathrm{Step}_{\mathrm{FSR}}$ is the maximum temperature that the control system needs to apply for stable operation (a full FSR). In most cases, this will be less than 1%.

$$P.O(\%) \leq \frac{\Delta T_{lock}}{\Delta Step_{FSR}} 100\% \tag{24}$$

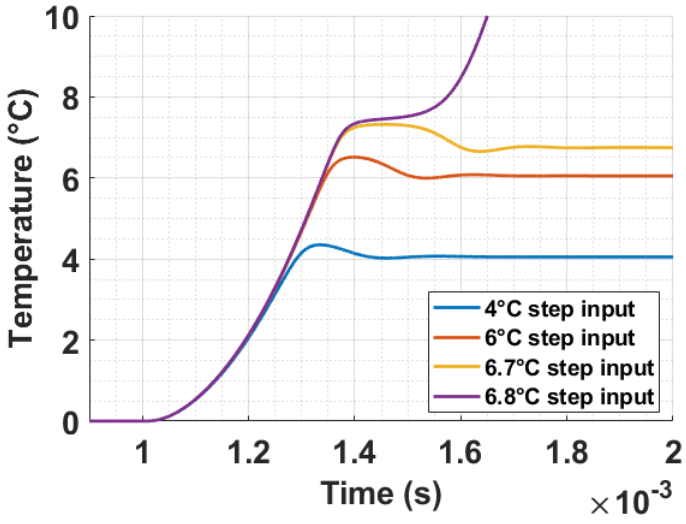

Figure 3.21: Unstability when the step response increases

Reducing the integral gain will reduce the percentage overshoot. With the new PI controller, the system's step response is shown in Figure 3.22b. This improved response will ensure the control system remains stable for any initial condition.

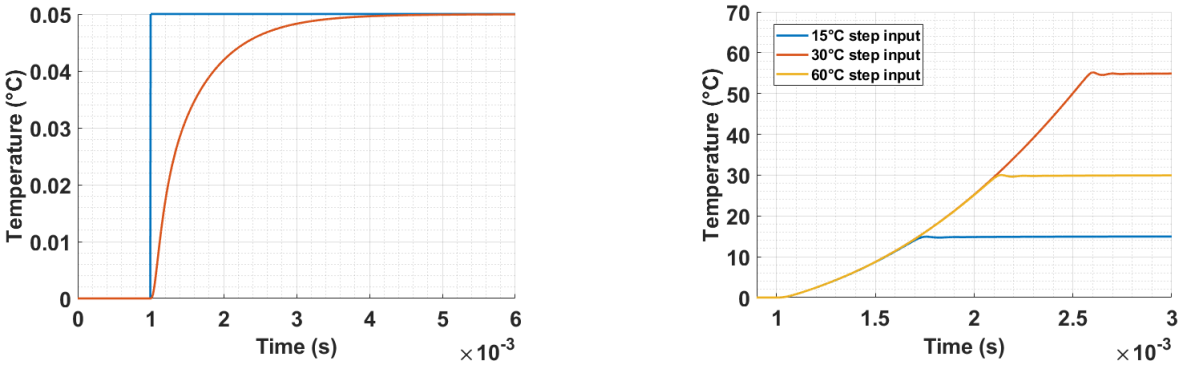

(a) (b)

Figure 3.22: Stability improvement by changing PID controller for larger input steps

3.4.6 Non-Balanced Input Issue

It was mentioned previously to assume that the data that modulates the MRM is balanced, meaning the same density of 1-bit and 0-bit. When the code is balanced, the average output powers are between a '1' or high power and a '0' or low power, as previously shown in Fig. 3.4. When the input modulation is not balanced, the average is no longer in the middle and varies based on the input density. Therefore, if the density of ones changes during operation, the average powers will also change. The controller will still lock the MRM, but instead of a single locking point, it is a region of locking that is not desired. In other words, this MRM will have different locking wavelengths based on the input density of ones.

Fig. 3.23 illustrates how the locking wavelength where the error signal is zero changes based on the density of ones at the input of the MRM. The balanced error is the same as Fig. 3.4, but as the density of one decreases, the zero error shifts toward the unbiased ring spectrum since more '0' bits are transmitted. As the density of one increases, the opposite happens, and the wavelength at which the error sigal is zero shifts towards the biased ring spectrum. Therefore, the zero error signal depends on the input density, and a region of possible locking points exists between the plot's two vertical lines.

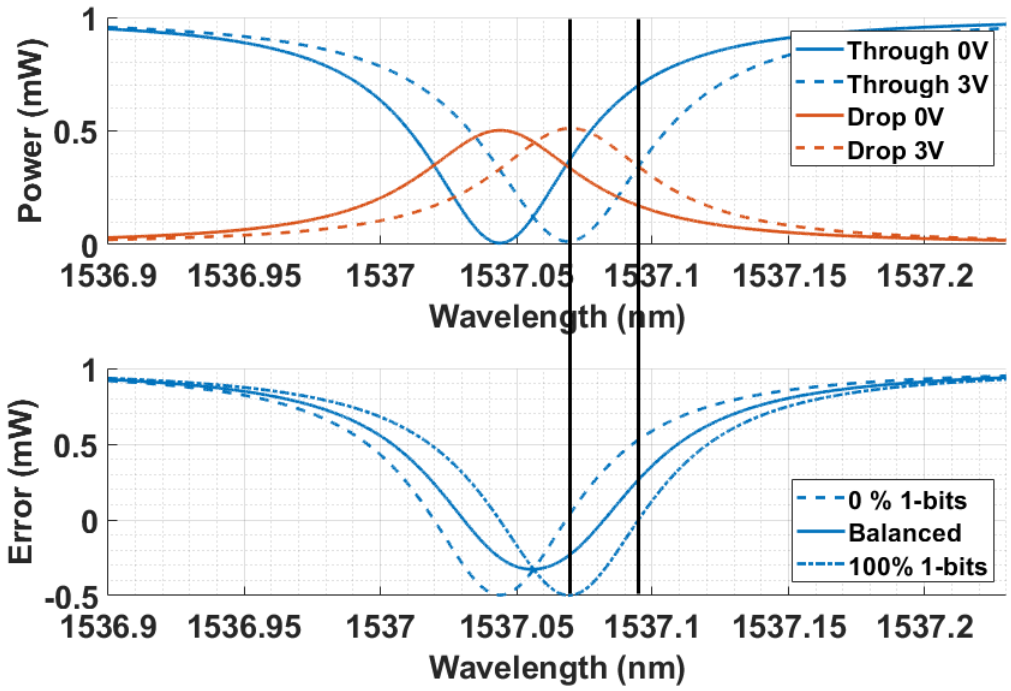

Figure 3.23: Error signal based on densities of 1's at the ring input

Figure 3.24 presents a simulation demonstrating the impact of changing input density on the system. The top graph illustrates the through and drop optical output powers, while the bottom graph shows the local ring temperature. The simulation varies the density of ones at the pn junction of the ring from 100 % to 0 % in drops of 10 %. It is observed that the ring temperature changes as the input density changes yet stabilizes at each density. Receivers can be designed to have variable thresholds, so the shift in locking point does not lead to data loss between 10 and 90 % since the OMA and ER remain acceptable. However, the problem arises when there is a long run of zeros or ones, causing the through and drop powers to become identical. In such cases, differential receivers cannot differentiate between a 1-bit and a 0-bit, leading to data loss.

It is worth noting that MRMs typically have balanced data at the input, so this is not an issue for them. However, in the context of logic gates where the data is unbalanced, the

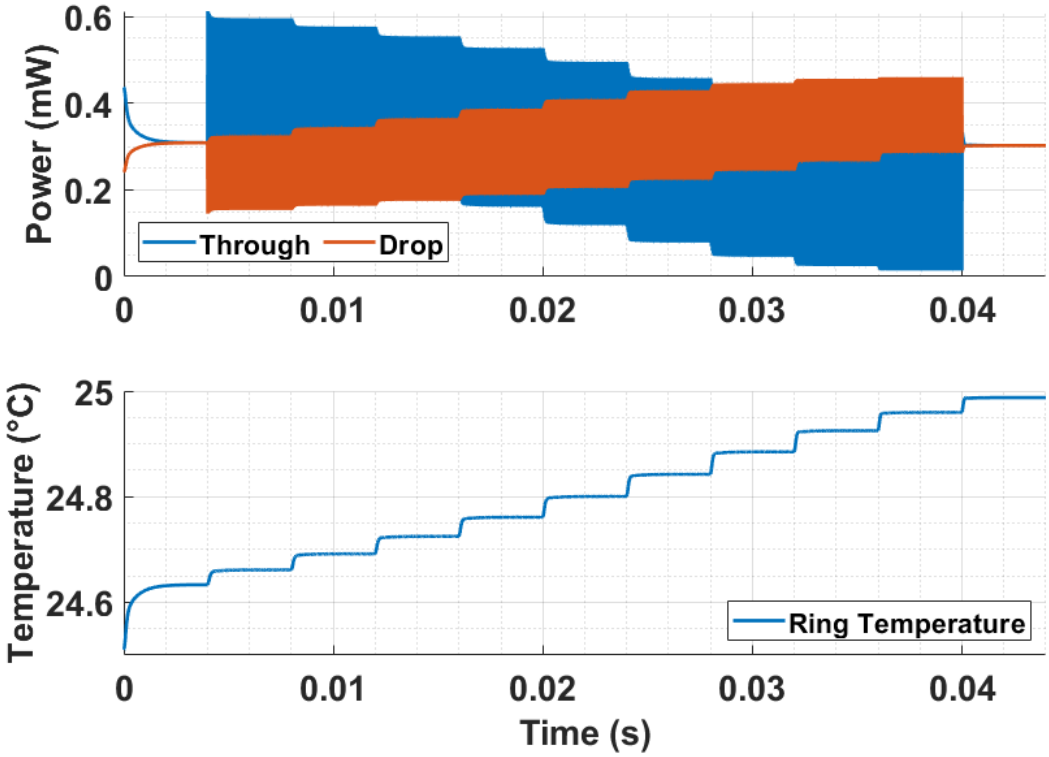

Figure 3.24: Simulation results where the input density of ones is varied from 100 % to 0% in steps of 10 % for a 3 V reverse bias amplitude

locking region poses a real problem. A solution is presented in Chapter 4.

3.5 OpAmp Based Design

The simulations previously presented validate the thermal control design proposed in Fig. 3.6. Experimental results are critical for proper validation. A PCB was designed and fabricated for this purpose. This section will present the thermal control design based on operational amplifiers (OpAmp).

Figure 3.25 displays the designed electrical schematic and can be separated into three sections: the through and drop TIAs (U1 and U2), the subtractor (U3), and the PID controller (U4-U7).

The TIA OpAmps are designed as low-pass filters with a small bandwidth to get the mean powers. The TIA output voltages can be derived by applying Kirchhoff's current law (KCL) at the inverting node and isolating the output voltage, which yields eq. 25 where $v_{through}$ is the output voltage of the through TIA, v_{drop} is the output voltage of the drop TIA, Z_f is the feedback impedance, and V_{bias} is the non-inverting node voltage.

$$v_{through}(t) = i_{through}(t)Z_f + V_{bias} \tag{25}$$

$$\frac{V_{through}(s)}{i_{through}(s)} = \frac{V_{drop}(s)}{i_{drop}(s)}Z_f = \frac{R_{tia}}{1 + sR_{tia}C_{tia}} \tag{26}$$

The PDs need to be reverse-biased to generate a photocurrent, and, in this case, the non-inverting node voltage biases the PD. The linearized transfer function at the biasing point yields eq. 26. This equation is identical to eq. 12 in section 3.4.5 as desired. R_{tia} is a variable resistor to allow pole and gain configuration during testing.

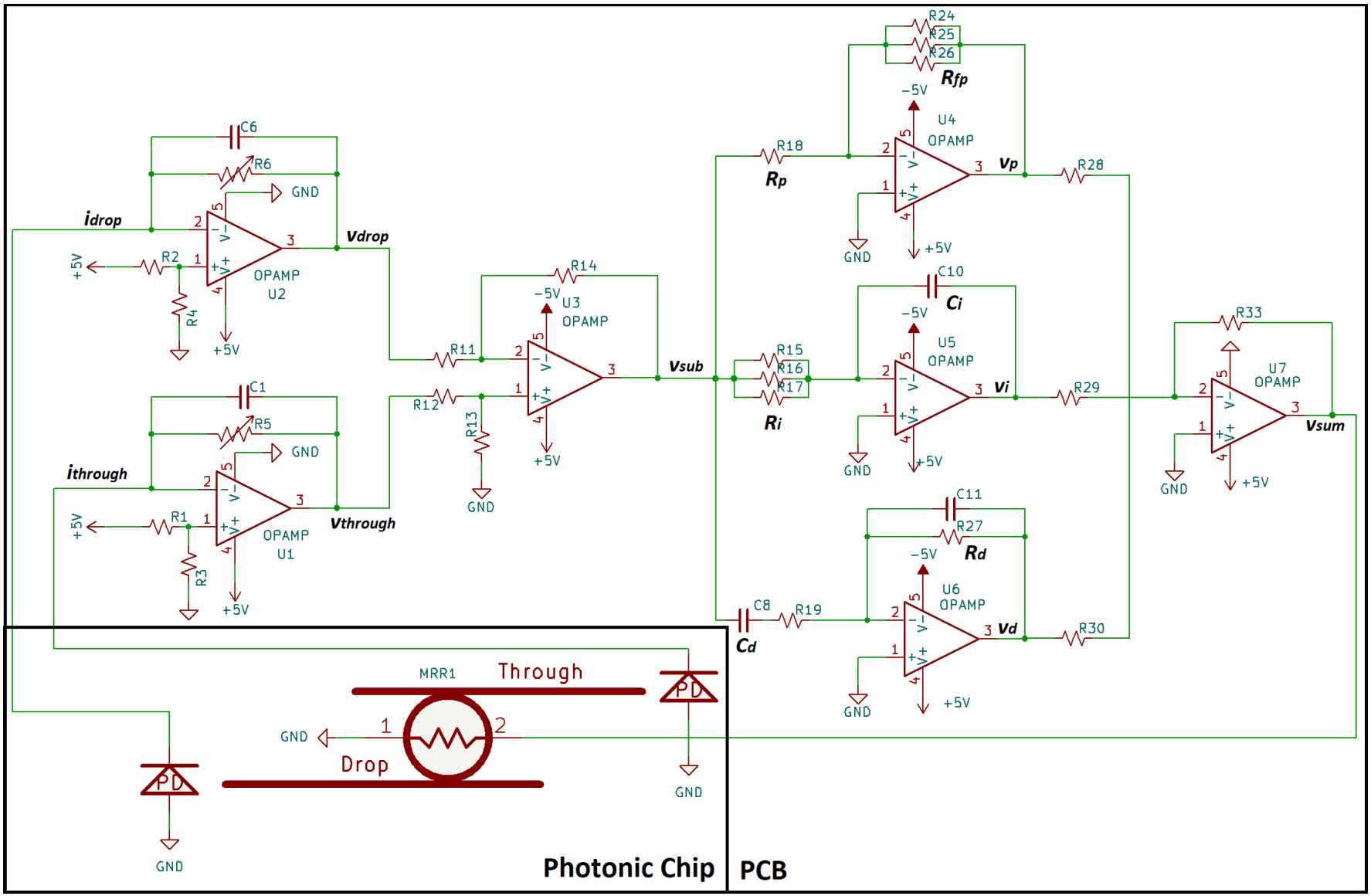

Figure 3.25: Opamp design for proposed thermal controller

The output of the subtractor can also be obtained by applying KCL at the inverting node and yields eq. 27 when the resistors are all identical.

$$v_{sub}(t) = v_{through}(t) - v_{drop}(t) = Z_f(i_{through}(t) - i_{drop}(t)) \tag{27}$$

The PID controller comprises four OpAmps: a proportional, integral, derivative, and summing OpAmp. The summing OpAmp adds the output voltages of the other three. Once again, applying KCL at each inverting node leads to eq. 28, 29, 30, and 31 for the proportional, integral, derivative, and summing OpAmps, respectively. The negative sign in each equation cancels out at the output of the summer. The values of R_{tia}, R_{fp}, R_i, and R_d are variable in the design to allow modifications in the gains of the TIA and PID controller for ease in testability. The derivative OpAmp was included in case the PI controller did not work, so jumpers for the derivative OpAmps were added in the final PCB to remove or include it in the feedback controller.

$$v_p(t) = -\frac{R_{fp}}{R_p} v_{sub}(t) \tag{28}$$

$$v_i(t) = -\frac{1}{R_i C_i} \int_0^t v_{sub}(t)\, dt \tag{29}$$

$$v_d(t) = -R_d C_d \frac{\mathrm{d}v_{sub}(t)}{\mathrm{d}x} \tag{30}$$

$$v_{sum}(t) = -v_p(t) - v_i(t) - v_d(t) \tag{31}$$

An additional capacitor is added to the feedback of the derivative OpAmp to limit the bandwidth and therefore high frequency noise. A resistor is also added in series to the input capacitor of the derivative OpAmp to limit the high frequency gain.

3.5.1 Simulations

Before designing and fabricating the PCB, the OpAmp-based design was extensively validated through simulations in Cadence. A Verilog-A ring model was coded into Cadence to serve as the MRM, and the Cadence model is presented in Appendix A. As the controller's OpAmps do not need high speed, voltage controlled voltage sources with extremely high gain were utilized instead. The simulation results are depicted in Fig. 3.26.

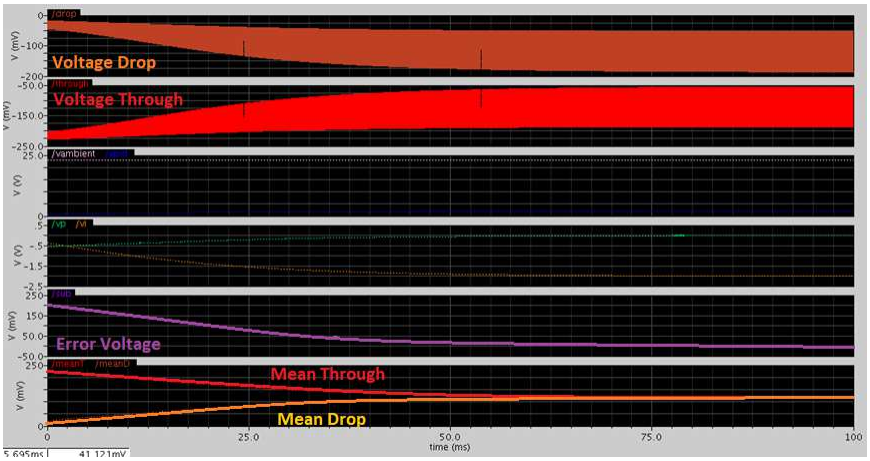

Figure 3.26: Simulations results of closed-loop operation for the OpAmp-based design

At the beginning of the simulation, the laser wavelength is set far from resonance in region C. This is evident from the significant difference in through and drop means. However, as the loop is closed, the output averages begin to converge. Eventually, the subtractor output falls to zero. Additionally, the through and drop OMA increases significantly until it stabilizes at the locking point. The results confirm that the OpAmp-based design is capable of effectively stabilizing MRMs and is ready for PCB implementation.

3.5.2 PCB Testing

After validating the OpAmp-based design using Cadence simulations, a PCB schematic and layout were completed using KiCad, which are displayed in Appendix B. Before testing the fabricated PCB with an ORR in an optical lab, the board was tested with simple lasers

and PDs to ensure proper functionality and to prevent accidentally damaging expensive optical equipment. Each individual OpAmp was tested to show proper functionality, but only the final closed-loop feedback control will be presented in this section.

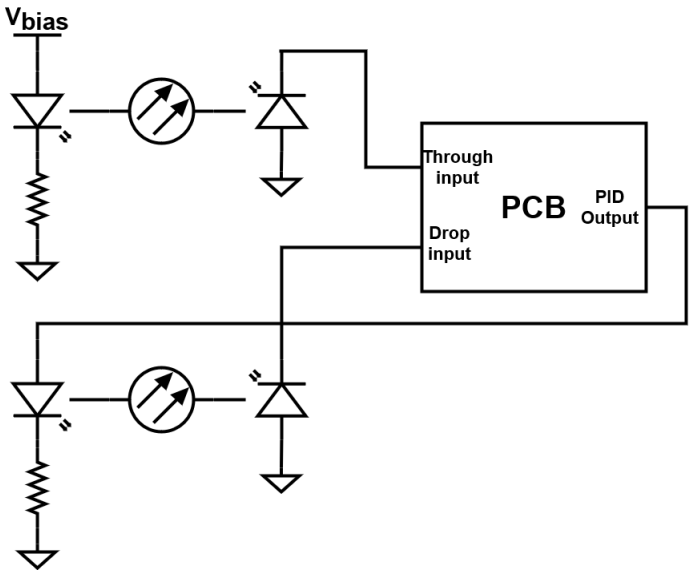

Figure 3.27: Test setup to validate PCB

Validating the feedback control requires a closed loop with optical/electrical conversions. Fig. 3.27 shows the test setup to validate the control loop. Two lasers are connected to two PDs with optical fiber. The current supplied to the lasers varies depending on the biasing voltage and resistor value. The higher the biasing voltage of the laser, the more optical power passes through the fiber, while decreasing the voltage leads to lower power in the fiber. The through port's laser has a constant bias. The drop port's laser is biased from the PID's output. Therefore, the feedback loop is closed. The PCB's circuit will change the drop port laser's bias until the optical power landing on both PDs is identical.

Fig. 3.28 depicts the closed-loop experimental results where channels 1, 2, and 3 are the through TIA, drop TIA, and subtractor outputs, respectively. At the start of this experiment, the feedback loop is open; then, it is abruptly closed. The error signal becomes positive since the through channel has a higher voltage than the drop. This error tells the controller to increase the biasing voltage of the drop laser, as seen by the increasing voltage on channel

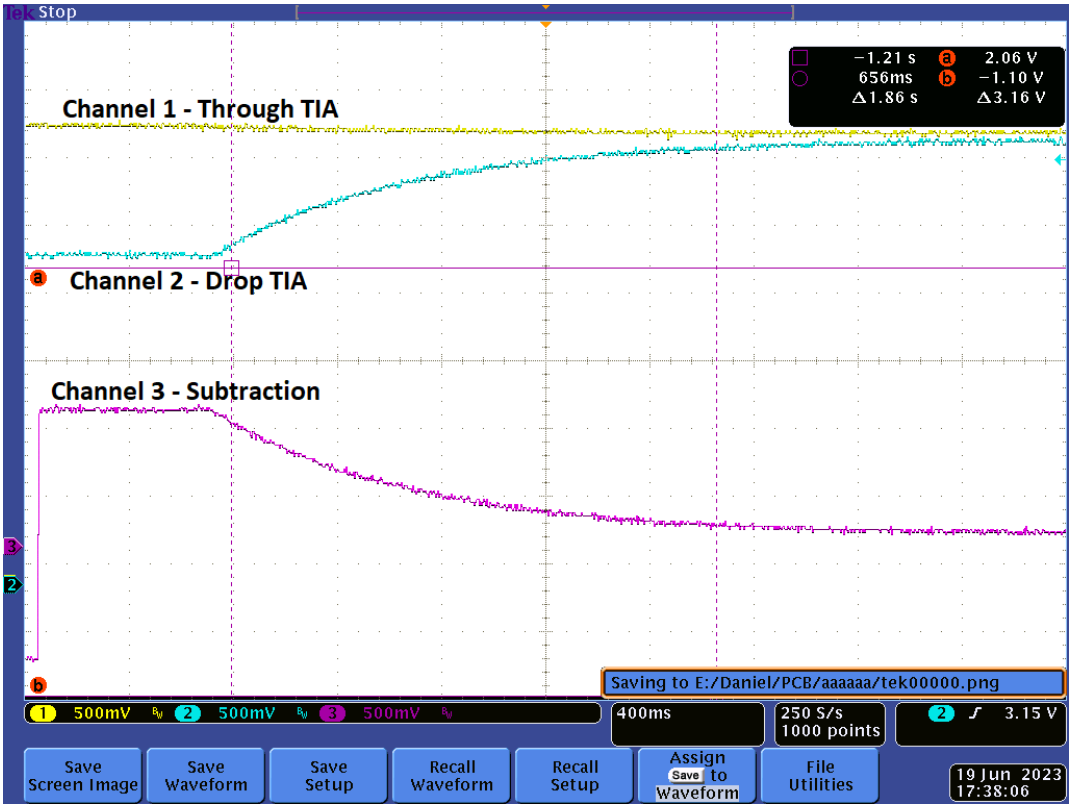

Figure 3.28: Experimental results for the PCB in a closed-loop

2. The error voltage reduces to zero, where the through and drop voltages are equivalent.

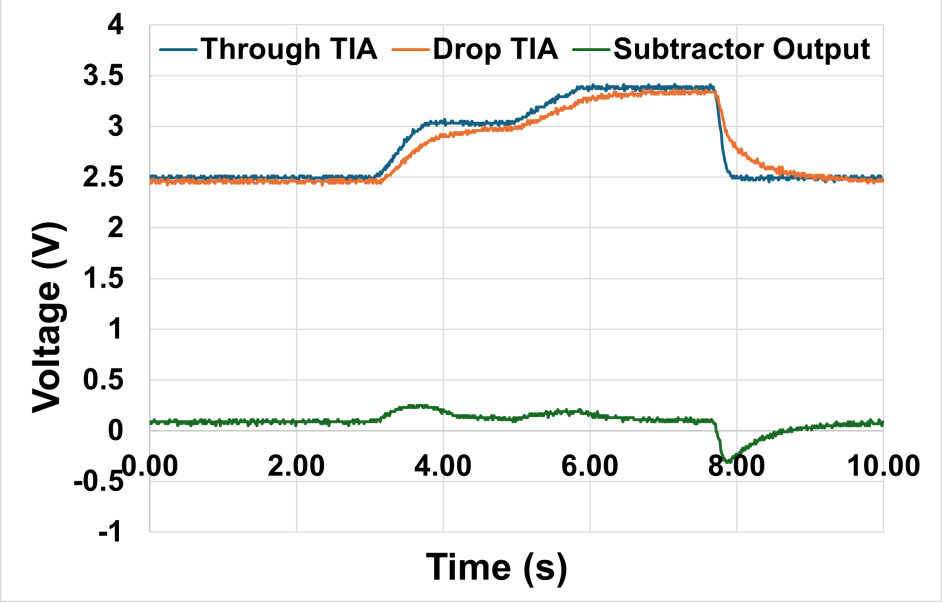

Figure 3.29: Experimental results for different laser biasing voltages

Fig. 3.29 illustrates the effect of varying the biasing voltage of the through laser. The feedback loop is closed this time, so the error signal starts at zero. The through laser's bias is varied in steps, and the controller automatically changes the bias of the drop laser to keep the error voltage zero.

These experiments validate the PCB design for a closed-loop feedback controller. The next step is testing the PCB with an ORR and validating the proposed thermal stabilization method.

3.6 Experimental Results

This section will show all experimental results obtained to validate the designed thermal controller for the ORR. The measurements of the microring's DC characterization are first presented. Then, wavelength locking will be demonstrated while the input laser wavelength varies. Finally, the change in operating wavelength based on the density of one's at the input will be depicted.

3.6.1 MRR DC Characterization

The designed microring's resonant spectrum depends on the ring's dimension and coupling ratios. So, a detailed characterization of the MRR used to validate the thermal controller provides insights into the obtained results.

The MRR was designed by José García-Echeverría, a PhD student from McGill. The design is a double-bus MRR with a width of 500 nm for single-mode operation, an insertion loss of 3 dB, a radius of 10 μm, and through and drop gaps of 350 nm and 300 nm, respectively, based on [36]. In addition, a TiW metal layer was placed on top of 90 % of the circular waveguide to act as the microheater. This design leads to an FSR of 8.8 nm, a tuning efficiency of 100 pm/mW, a FWHM of 0.1 nm at 1550 nm, and a Q-factor of 15500.

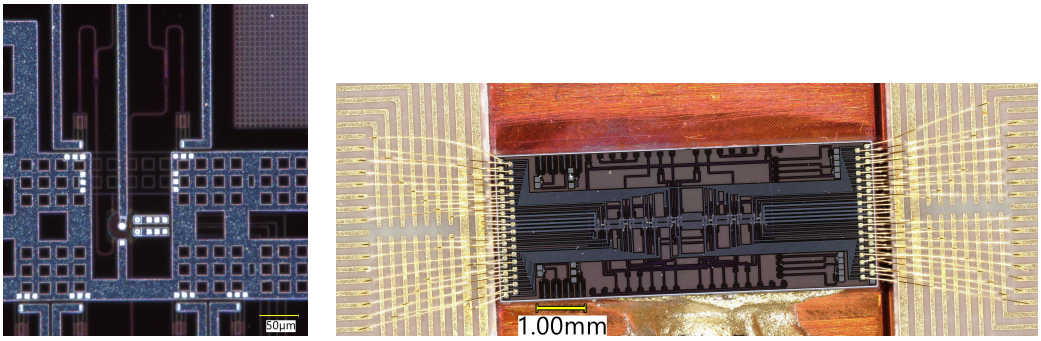

(a) Designed MRM (b) Wirebonded Chip

Figure 3.30: High resolution pictures of the fabricated photonics chip

Laser wavelength sweeps were conducted under different conditions to acquire the DC characterizations of the MRR. The thermal controller has yet to be included, so the wavelength sweep displays the full resonance spectrum. Fig. 3.31 shows the results of the wavelength sweep for the non-biased microring and the Lorentzian approximations of the measured results. These approximations were used in all simulation results presented earlier, showing a high degree of confidence in the simulation results.

The measured results showing the shift in resonance due to the reverse bias of the MRR's pn junction are displayed in Fig. 3.5. Finally, the measured tuning efficiency of the integrated heater is shown in Fig. 3.32. With an FSR of 8.8 nm and tuning efficiency of 100 pm/mW, the heater will need 88 mW to tune the ring for a full FSR, but the integrated heater can only handle around 45 mW before risking burning the metal. However, [37] achieved an efficiency of 1.25 nm/mW using thermal isolation through substrate removal. Adding this to a future optical chip design can lead to full FSR tuning while being considerably more power efficient.

The final results are summarized in Table 3.3. The measured Q-factor is 22 900, far from the expected 15 500. The FSR measured was 8.8 nm, but the resonant wavelength is not at 1550 nm but around 1554 nm. These differences highlight the significance of a thermal controller immune to process variation during manufacturing.

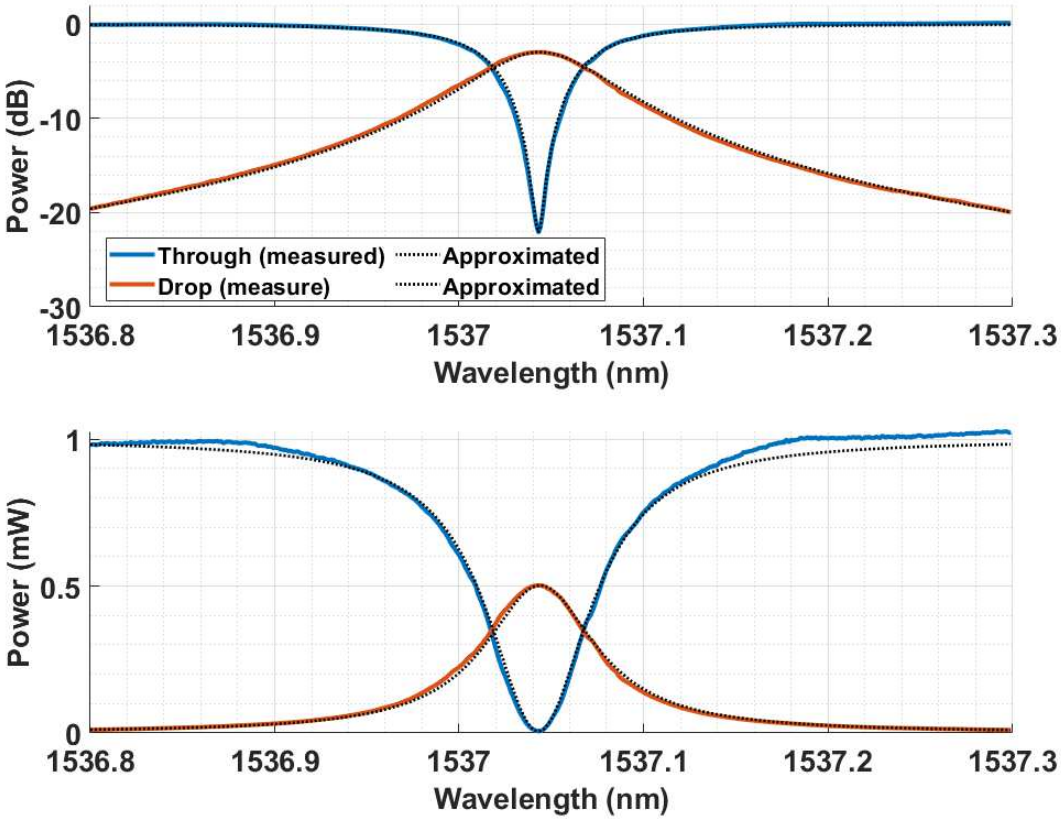

Figure 3.31: Measured resonant spectrum of fabircated MRR

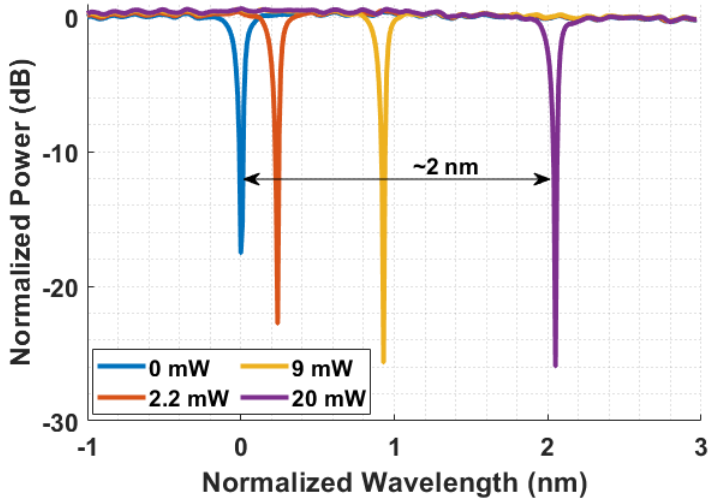

Figure 3.32: Measured tuning efficiency of the microheater

Table 3.3: Microring DC Characterization Measurements

Ring Parameter	Measured Value
Resonant Wavelength	1537 nm
FSR	8.8 nm
FWHM	67 pm
Q-Factor	22 900
Tuning Efficiency	104 pm/mW
Thermal Efficiency	74 pm/°C

3.6.2 Wavelength Sweep Locking

As an initial test for the thermal controller, the MRM is not biased, with the CWL wavelength to the right of the resonant wavelength (in region C). The tapped through and drop outputs that land on PDs are connected to the thermal controller PCB. The outputs are also connected to individual optical power meters to measure the output powers. With the feedback loop open, the power meters should display a high power for the through port and low power for the drop. Once the loop is closed, both power meters should stabilize around the same value. A block diagram of the test setup is shown in 3.33.

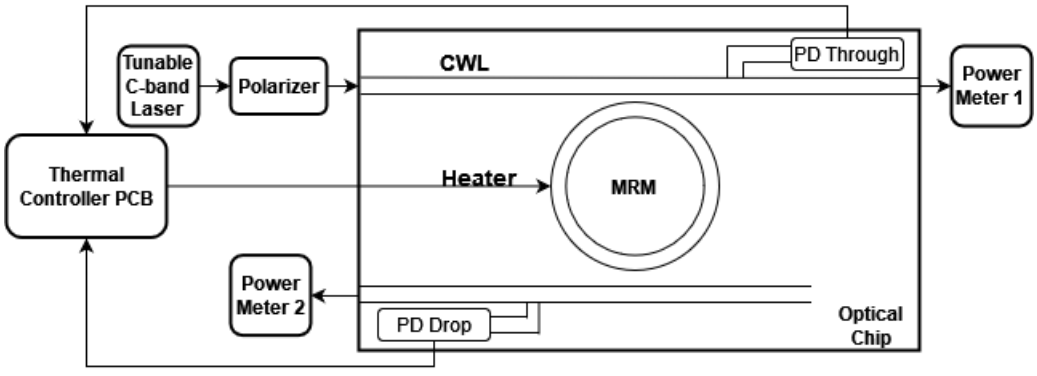

Figure 3.33: Test setup used to validate through = drop control

The results of this experiment are displayed in Table 3.4. The aggregate losses of the setup resulted in a maximum output power reading of -17.8 dB when the loop was open. Based on the measured spectrum in Fig. 3.31, the power when through = drop is -4.6 dB from the maximum power. Thus, the expected power under closed-loop conditions is

-22.4 dB, which is very close to the measured value of -22.96 dB. This result increases the confidence in this thermal control method. The closed-loop output powers are not identical, but this can be attributed to different losses and responsivity in the different paths.

Table 3.4: Initial experimental result of MRR locking with constant CWL

	Through Power (dB)	**Drop Power (dB)**
Open-Loop	-17.786	-52.166
Closed-Loop	-22.960	-22.018

The following experiment is the same, but two rings are locked simultaneously from a single laser this time. Compared to the previous setup, a 3 dB splitter is added after the laser to guide the light to the different rings. Only two power meters were available, so only the through outputs of each ring were measured. The results are depicted in Table 3.5.

Table 3.5: Locking two microrings to the same laser

	Ring 1 Power (dB)	**Ring 2 Power (dB)**
Open-Loop	-20.39	-20.46
Closed-Loop	-24.5	-24.78

After closing the loop, the through power of both microrings dropped by 4.3 dB, close to the expected value. These results indicate that the thermal controller can thermally stabilize multiple rings to the same laser, which reduces the number of lasers needed and increases power efficiency. Up to seven different MRRs have been simultaneously locked from a single laser but will not be presented here.

To properly evaluate the thermal controller, it must be tested under variations in external temperature. This is typically done with a thermoelectric cooler (TEC). However, the grating couplers of the photonic chip are affected by temperature changes due to the expansion and contraction of the chip. Hence, the TEC method cannot be used for this test. Instead, remember that changing the laser wavelength and adjusting the local ring temperature have similar effects: one alters the laser's wavelength while the other adjusts

the resonant wavelength of the ring. Therefore, sweeping the wavelength under closer-loop thermal control is an alternative to demonstrate thermal locking.

Fig. 3.34 displays the acquired results for the laser wavelength sweep during closed-loop and open-loop operation. As expected, without the controller, the wavelength sweep reproduces the resonant spectrum measured in Fig. 3.31. However, the same wavelength sweep with the controller now exhibits equivalent powers in the through and drop power meters around -4.6 dB of the maximum. These results confirm the controller's ability to maintain the operating point independently of temperature.

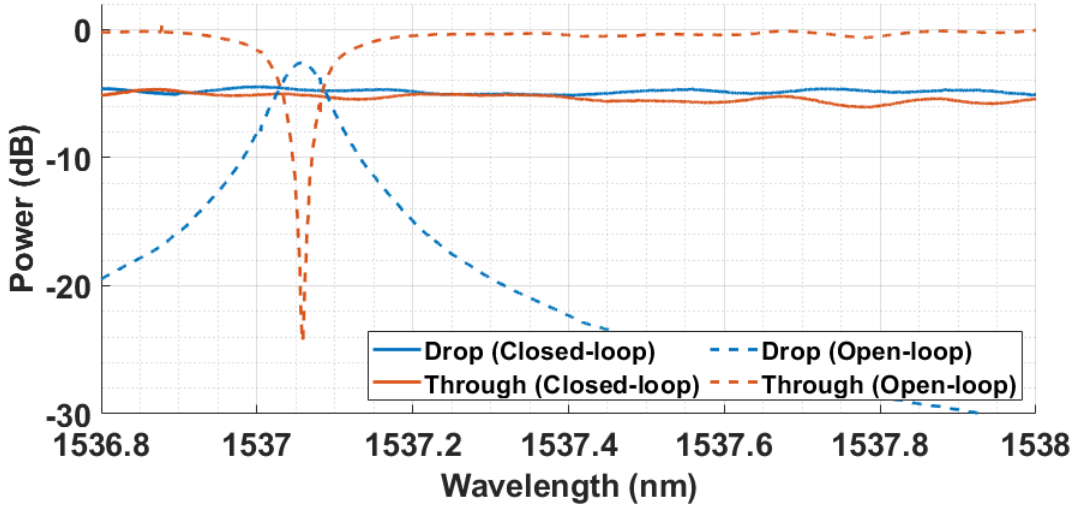

Figure 3.34: MRR output powers with and without thermal controller during CWL wavlength sweep from 1536.8 to 1538 nm

Before running the closed-loop sweep, the microring was cooled by 4 °C with a TEC and kept stable. Therefore, the blue shift in the resonance is not due to the controller but the TEC instead. In Fig. 3.34, slight deviations from through = drop operating point can be observed. This leads to a slight error in the locking point of about ± 3 pm. This controller's sources of error are the mismatch between splitting ratios, PD responsivities, and TIA gains, but this does not explain why the difference is not constant for a sweep in frequency. The PD responsivity is a function of wavelength, so the varying error from the

locking point is most likely due to the mismatch in the PD's responsivity.

During the closed-loop sweep, the control signals on the PCB were measured for the first 110 pm change in wavelength and are shown in Fig. 3.35. The TIA outputs remain equivalent throughout the sweep at around 2.47 V. The error signal stays steady at around -0.2V. The small deviation from zero is due to the oscilloscope's slight inaccuracy when measuring DC values. As expected, the heater voltage increases with time due to the red shift in the laser wavelength. The laser started sweeping its wavelength at around 17 seconds, which explains why the initial heater voltage remained constant. In addition, the laser used can only vary its wavelength slowly, resulting in a long time frame.

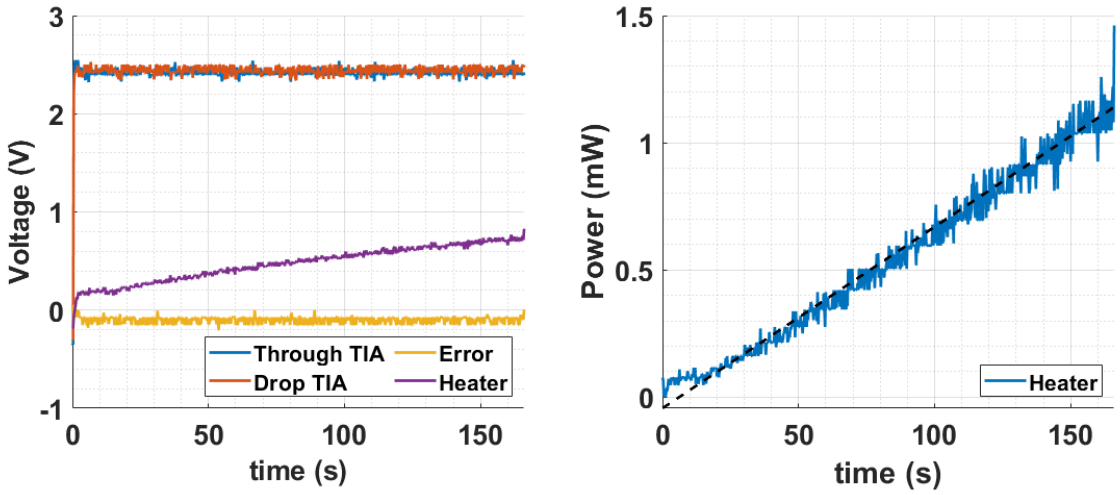

Figure 3.35: PCB control signals during wavelength sweep

The power dissipated in the heater is plotted based on the heater voltage and the 470 Ω microheater. The laser wavelength is increased at regular intervals, so the power increases linearly with time due to the linear relationship between power and resonance shift. The wavelength shift was 110 pm, and the heater power varied by 1.06 mW; therefore, the tuning efficiency is calculated to be 103 pm/mW, which is very close to the efficiency that was initially measured.

3.6.3 Data Dependent Locking

The final test demonstrates the thermal controller's operating point as a function of the density of ones for the modulated data. The test setup is presented in Figure 3.36, similar to the previous setup, but with an extra waveform generator to modulate the MRR.

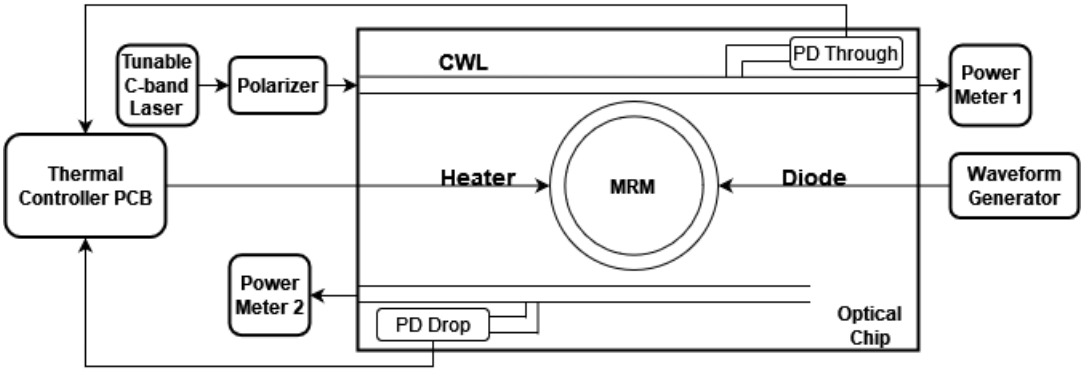

Figure 3.36: Test setup for data dependent locking

The waveform generator generates a 3 V square wave with a 0, 30, 50, 70, and 100 % duty cycle at 75 kHz, and the heater voltage is measured for each. Table 3.6 shows the measured results.

Table 3.6: Control operating point based on the modulating data's density

Density of 1's (%)	Heater (V)	Heater (mW)	Resonant shift from 100 % (pm)	Expected resonant shift from 100 % (pm)	Percentage Error (%)
0	0.985	2.066	23.8	26.6	10.45
30	0.964	1.978	14.7	19.0	22.61
50	0.9514	1.926	9.34	12.7	26.49
70	0.941	1.882	4.77	6.9	30.88
100	0.929	1.836	0	0	N/A

The laser's wavelength is initially set to the right of the locking point, so the closest operating point is 100 % density, which requires 0.929 V to heat. All other operating points will be normalized to this one. The voltage is then converted to power, and based on the 104 pm/mW initially measured, the shift in operating wavelength from the baseline is

calculated. Results show that the locking point does change based on the data, as expected. Compared to the expected values based on the locations of the zero errors in Fig. 3.23, the measured values are not quite the same. This mismatch is probably due to the waveform generator outputting slightly less than 3 V. The results are graphically depicted in Fig. 3.37.

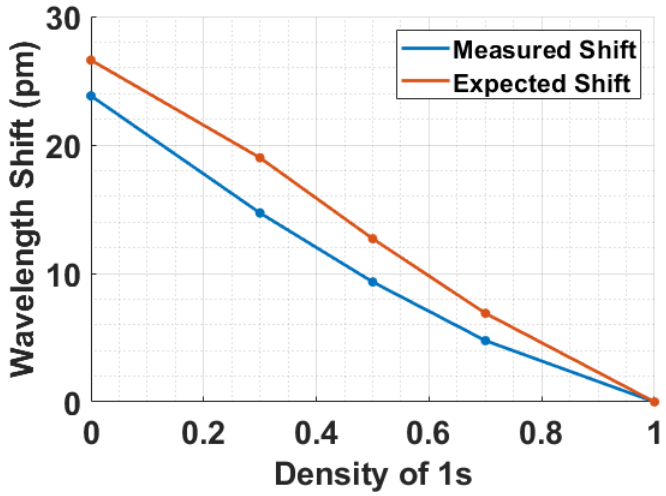

Figure 3.37: Plot of the normalized wavelength shift as a function of input density

These results demonstrate that the operating wavelength of the thermal control depends on the data and requires balanced data to maintain a single locking point. However, the next chapter presents a solution to this problem.

3.7 Summary

In this chapter, a novel method for stabilizing MRMs has been discussed. The method's fundamental working principle involves utilizing the through and drop spectrums of the microring and locking the operation at the point where they are equal. As a result, the method uses a self-reference to lock and does not require any calibration or reference value. Through simulations, it has been demonstrated that this method can lock at a near-optimal OMA, is immune to power and wavelength variations of the CWL input, and is immune

to temperature fluctuations. After designing and fabricating a PCB, the design was experimentally validated with an MRM.

Chapter 4

Tuning for Non-Balanced Ring Modulation

The simulated and experimental results have demonstrated that the proposed thermal controller, illustrated in Fig. 3.6, has an operating point that varies dynamically based on the input data density. This characteristic is not a concern for high-speed modulators as the input data is typically balanced. However, this feature becomes a critical roadblock for logic gates that lack balanced data. This chapter describes a modified design that addresses this issue. Furthermore, simulated results will be presented to validate these changes.

4.1 Modified Design Operation

The modified design is illustrated in Fig. 4.1. The design shares many similarities in its overall structure with that shown in 3.6. They both incorporate a splitter to tap power from the through and drop ports, PDs, and TIAs for conversion, subtractors to generate the error signal, a PID controller to stabilize the error to zero, and a microheater to vary the local temperature of the ring. The significant difference is the implementation of the TIA. It has been revised into a variable gain TIA (VG-TIA) that adjusts the transimpedance

gains in response to input data density. This improvement compensates for the controller's operating point variation based on data density, effectively reducing the operating region to a single wavelength.

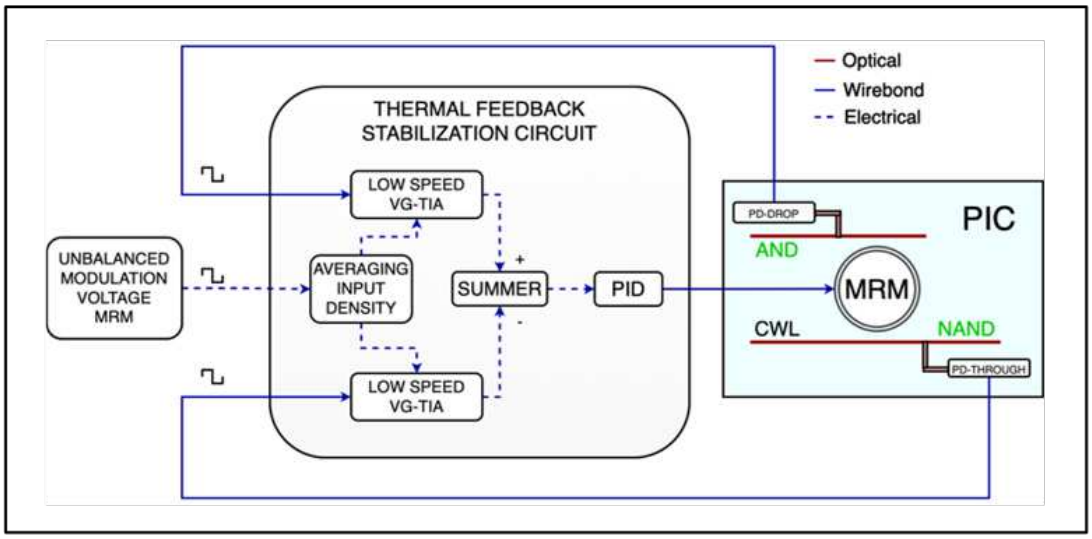

Figure 4.1: Modified thermal controller design for a stable MRR under variable data densities

4.1.1 Variable Gain Regression Models

The compensated design will operate at a single wavelength, regardless of input data density. The wavelength can be chosen from within the non-compensated design's locking region illustrated in Fig. 3.23. As the initial balanced design demonstrated near-optimal OMA, the same point will be selected for the compensation design. For insights into how the VG-TIA compensates for variations in input density, refer to Fig. 4.2. The figure illustrates that the average power of the through varies as a function of input density, as expected. For a single locking point, the TIA outputs must stay constant independent of the input density. This can be accomplished by elevating the transimpedance gain of the through output for input densities below 0.5 and reducing the TIA gain for input densities above 0.5. The adjustments in TIA gains must precisely shift the mean output powers to

match that obtained from a 0.5 input density. This process must also be applied to the drop VG-TIA.

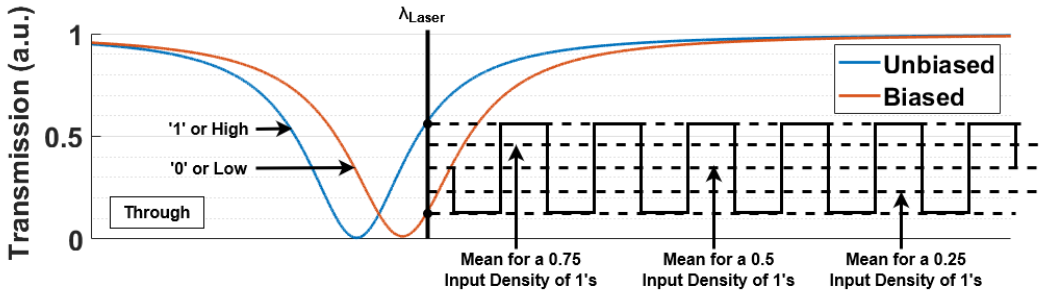

Figure 4.2: Change in average power of through based on the input density of 1's at original through=drop wavelength

To determine the optimal compensation model for the VG-TIA at the selected locking point, the mean power of both the through and drop outputs must be measured for different input densities at the desired wavelength. Fig. 4.3 plots the simulated results of the through and drop means while varying the input density of ones from 100 to 0 % in decrements of 10 % with the thermal controller off and the laser positioned at the selected operating point. Notice that the through and drop means are identical only at 0.5 density of ones, which aligns with expectations considering the selected operating point. In order to maintain a zero error signal across all input densities, it is necessary to calculate the required gain to reach the same mean power of the 0.5 input density. The gain corrections are found using eq. 32 where $\mathrm{mean}_{50\%}$ is the mean power for 0.5 input density and mean is the mean at each density.

$$Gain_{TIA} = \frac{mean_{50\%}}{mean} \tag{32}$$

The calculated results for the required TIA gains at 3 V modulation are presented in Table 4.1. Based on these calculations, Fig. 4.4 illustrates the gain as a function of density for 1, 2, 3, and 5 V modulations. The final compensation model for the VG-TIA results

g

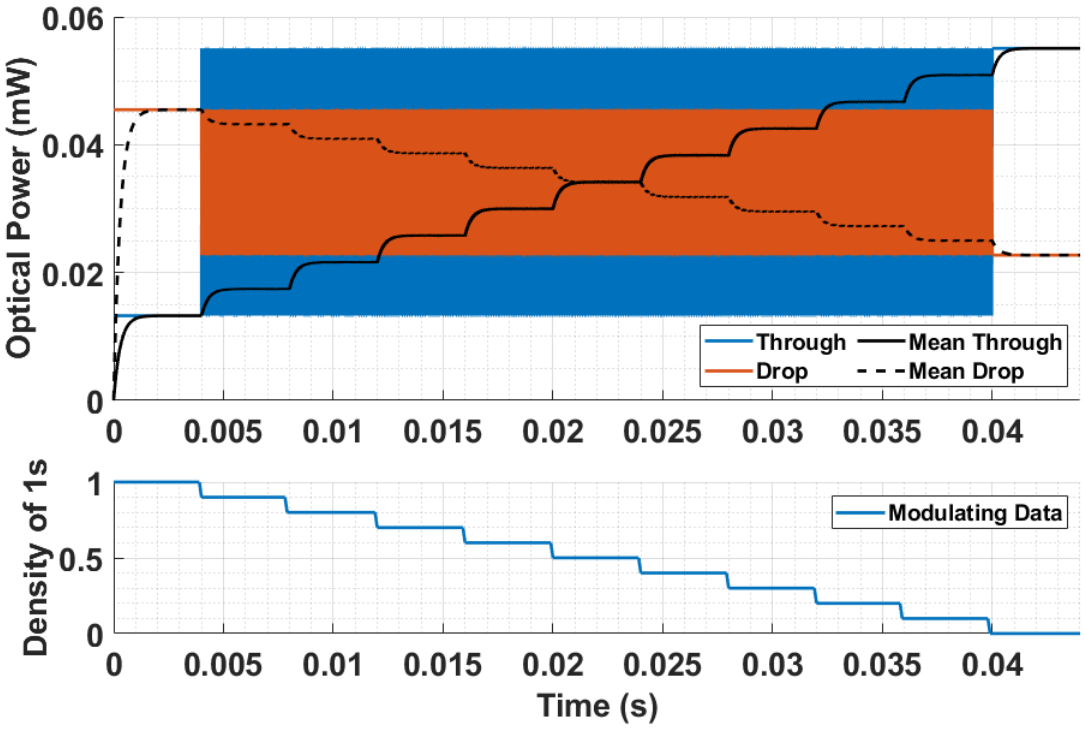

Figure 4.3: Open-loop simulation of the operating point at different input densities

from linear fittings of these plotted functions. More complex fittings can be used for narrower operating points and increase in OMA, but at the cost of more complex electronic implementation.

Table 4.2 shows the linear fittings plotted in Fig. 4.4. These results indicate a significant reduction in linearity as the reverse bias voltage increases, which impacts the overall operating point. The following section provides simulation results showing the non-linear effect on the operating point.

Table 4.1: TIA gains required to maintain single locking point as a function of input density for a 3V modulation

Input Density of 1s	Through		Drop	
	Mean	TIA Gain	Mean	TIA Gain
1	0.013	2.578	0.045	0.750
0.9	0.017	1.959	0.043	0.789
0.8	0.022	1.580	0.041	0.833
0.7	0.026	1.324	0.039	0.882
0.6	0.030	1.139	0.036	0.937
0.5	0.034	1.000	0.034	1.000
0.4	0.038	0.891	0.032	1.072
0.3	0.043	0.803	0.030	1.154
0.2	0.047	0.731	0.027	1.250
0.1	0.051	0.671	0.025	1.364
0	0.055	0.620	0.023	1.501

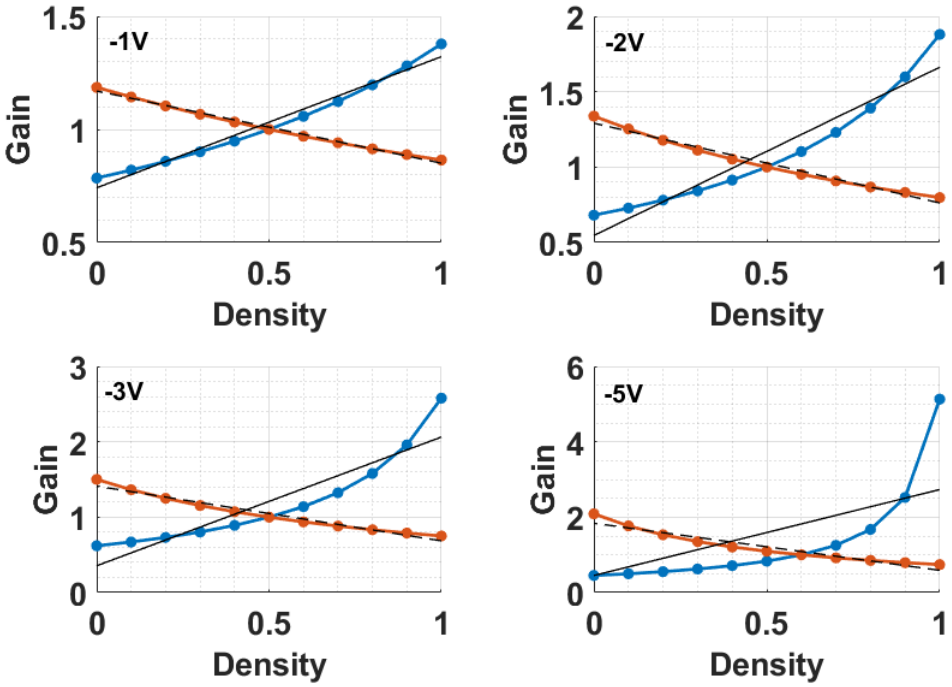

Figure 4.4: Linear fittings of the gain vs density results

Table 4.2: Linear fittings of gain vs density for optimal R^2

Reverse Bias	**Through**		**Drop**	
Amplitude (V)	**Linear Fitting**	R^2	**Linear Fitting**	R^2
1	$0.58x + 0.74$	0.97	$-0.32x + 1.17$	0.99
2	$1.12x + 0.55$	0.92	$-0.53x + 1.29$	0.98
3	$1.36x + 0.6$	0.85	$-0.73x + 1.41$	0.96
5	$2.28x + 0.45$	0.63	$-1.25x + 1.84$	0.92

4.2 Simulation Results

The simulation results presented in this section were obtained using Matlab and Simulink software. The ring model employed is the same as the balanced results, including the VG-TIA. The VG-TIA has a variable gain based on the previously calculated linear fittings in Table 4.2. The first simulation will repeat the one used for Fig. 3.23 where the input density of ones is decremented in steps of 10 % from 100 % to 0 %.

The simulation results are presented in Fig. 4.5. It can be observed that the temperature variation of the ring is much smaller than the previous simulation shown in Fig. 3.23. As a result, the operating region based on the input data is significantly reduced. However, the locking temperature is not constant due to imperfect linear fitting. A more sophisticated fitting leads to a more accurate operating point with the drawback of a more complex circuit design. Additionally, it should be noted that at 100 % and 0 %, the through and drop powers are no longer equal, indicating that the modulated data is not lost in a differential receiver.

Finally, a variable threshold receiver is not needed anymore to differentiate between a '1' and '0' bit since the operating wavelength is now almost constant. However, since it is not constant, the OMA and ER will be slightly reduced, as seen in the following section. Only a perfect fitting will result in the optimal OMA and ER obtained in the previous chapter.

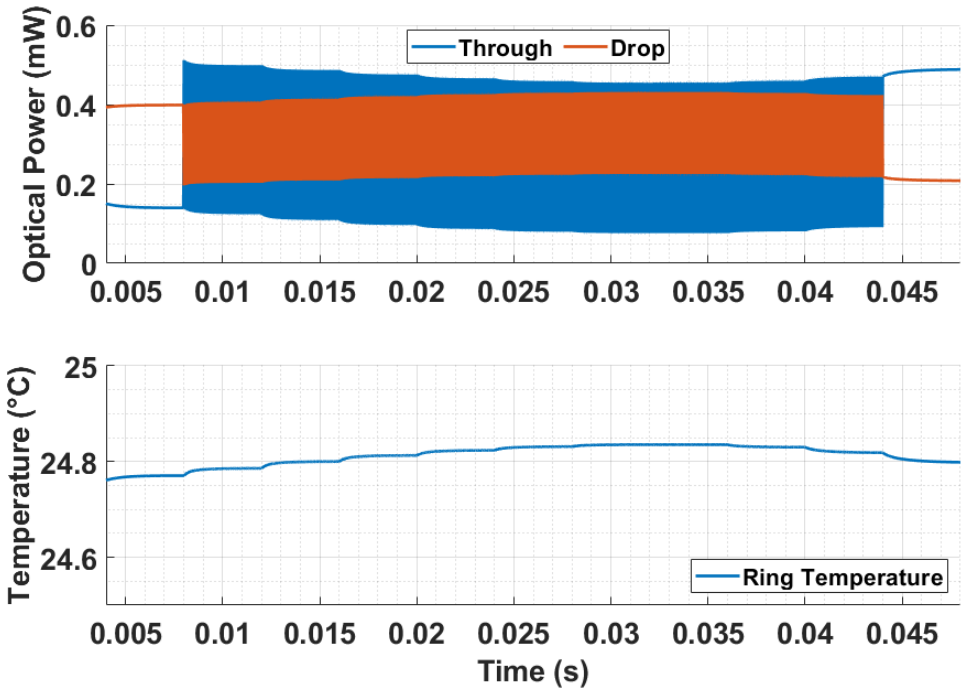

Figure 4.5: Simulation results where the input density of ones is varied from 100 % to 0% in steps of 10 % for a 3 V reverse bias amplitude with data compensation

4.2.1 OMA

As the compensated thermal controller is intended for logic gates applications, long-distance transmission is not a requirement. Therefore, the OMA is the optimal locking point. Hence, a comprehensive analysis of the reduction in OMA due to the linear fitting is crucial and will be presented next.

Table 4.3 displays the simulated OMA results of the compensated design for various reverse bias amplitudes and compares them to the optimal OMA. Envisioned MRR-based logic gates might utilize a differential receiver approach that measures the through-drop power. Therefore, the differential OMA is also investigated. Simulation results visualizing this comparison is available in Fig. 4.6.

Upon observing these results, it becomes clear that there is indeed a decrease in OMA when using the data-compensated thermal controller. This decrease occurs because the

Table 4.3: Comparison of the compensated design OMA to the Optimal OMA for all input denisities

Reverse Bias Amplitude (V)	OMA					
	Differential			Through Only		
	Optimal	Compensated	%	Optimal	Compensated	%
1	0.312	0.278	89.1	0.213	0.177	83.1
3	0.663	0.541	81.6	0.443	0.349	78.8
5	0.923	0.703	76.2	0.603	0.445	73.8

linear fittings are imperfect and still induce slight shifts in the locking wavelength based on the input density. A perfect fitting would have a stable locking point, and the resulting OMA would be the same as the one obtained in the balanced thermal controller.

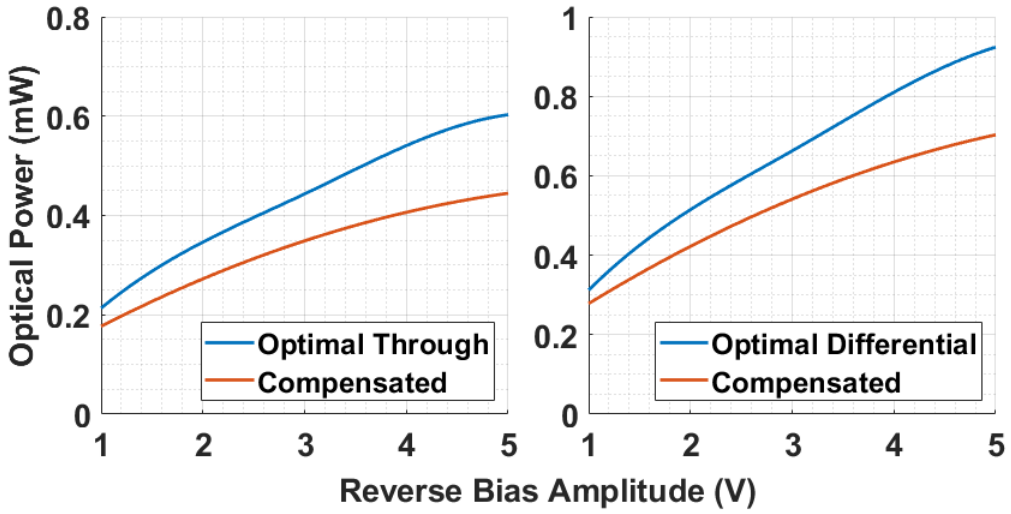

Figure 4.6: OMA as a function of reverse bias amplitude for the data compensated design

It has also been observed that when the input data amplitudes are higher, the OMAs tend to be worse. This can be attributed to the reduction in the linearity of the gain compensation as the amplitude increases. The accuracy of linear fittings decreases, and as a result, the locking wavelength tends to vary more. Better fitting (polynomial fittings) are the solution, but they significantly increase the complexity of the design.

4.3 Stabilizing Thermal Variations

Although simulations have shown that the non-balanced thermal controller can compensate for fluctuations in input data density, its performance in response to temperature changes has yet to be demonstrated. This section will investigate the controller's ability to stabilize the temperature. The same simulation as in Section 3.4.2 for balanced data will be explored here.

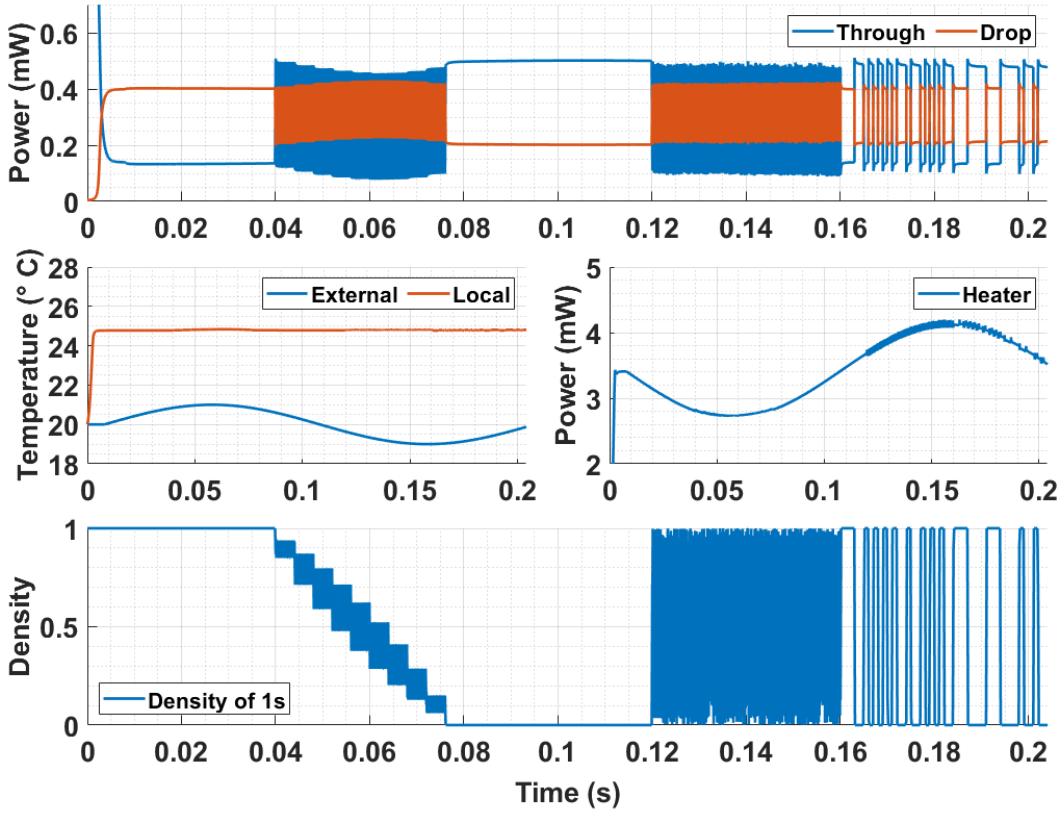

Figure 4.7: Simulation results demonstrating stable operation for the compensated thermal controller against temperature and density fluctuations for a 3 V reverse bias

In this simulation, the external temperature in the ring's model varies with an oscillation of 5 Hz. Moreover, since the design is intended for non-balanced applications, the density of ones at the input of the ring will also vary with time. Fig. 4.7 displays the obtained results. Observe that the microheater power oscillates with a π-phase shift compared to the

external temperature, effectively counterbalancing the temperature and ensuring that the local ring temperature remains constant. This observation serves as evidence of the thermal controller's proficiency in maintaining a locking point despite temperature fluctuations.

Furthermore, the figure showcases how the density of 1's at the input changes with time, yet the controller keeps the locking point stable. Although there are minor shifts in the locking temperature, these can be attributed to the imperfect linear fitting.

Chapter 5

Comparison and Conclusion

5.1 Thermal Stabilization Comparison

The previous chapters have presented a new and comprehensive approach to thermal stabilization of MRMs, which has been verified through simulations and experimental results. To ensure its effectiveness and identify potential areas for improvement, it is essential to compare this control with existing methods. Table 5.1 provides a comparison between the current solutions available for thermal stabilization of MRMs and the new approach. The comparison is based on the essential features required for an MRM thermal stabilizer.

The first method, which employs athermal MRRs [22], necessitates manual tuning for each ring after fabrication due to process variation. Moreover, active control is still necessary as there could be fluctuations in the input laser wavelength, but it is no longer feasible since athermal rings are not sensitive to temperature. Lastly, the fabrication process is further complicated by the exact waveguide widths required to produce athermal rings.

The second approach, which involves utilizing a thermal sensor, also demands a calibration process to select the locking point of each produced structure, owing to process variations. In addition, since only the local temperature is measured, any variation in laser wavelength will not be detected.

Table 5.1: MRM thermal stabilization method comparison

	[22]	[6]	[27]	[9]	[8]	[5]	This work
Ring Q	N/R	∼4700	∼8000	N/R	∼5000	∼5000	∼22 000
Wavelength Locking Method	Athermal MRR	Thermal Sensor	Average power	pn junction current monitoring	OMA monitoring	Dithering Signal	Through = Drop Monitoring
Heater Efficiency	N/A	0.12 nm/mW	N/R	N/R	0.15 nm/mW	N/R	0.1 nm/mW
Tuning Range	35 °C	125 °C	0.28 nm	4.8 nm	5 nm	N/R	4.7 nm
Locking Point	Manually Chosen	Manually Chosen	Optimal ER	Optimal ER	Optimal OMA	Minimum TP	Optimal OMA
Calibration-free	No	No	No	No	Yes	Yes	Yes
No start-up sequence	NA	NA	Yes	Yes	No	No	Yes
Immune to thermal fluctuations	Yes	Yes	Yes	Yes	Yes	Yes	Yes
Immune to Process variation	No	No	Yes	No	Yes	Yes	Yes
Immune to laser power variations	Yes	Yes	No	No	Yes	Yes	Yes
Immune to laser wavelength fluctuation	No	No	Yes	Yes	Yes	Yes	Yes
RF electronics	No	No	No	No	Yes	No	No
WDM compatible	Yes	Yes	Yes	Yes	Yes	Yes	Yes*
CMOS compatible	Yes	Yes	Yes	Yes	Yes	Yes	Yes

* Not the traditional single bus WDM, but can be done with different buses that converge after modulation.

The third technique, which involves monitoring the average power and comparing it to a reference [27], addresses many key system features. Initial calibration is required to determine the optimal reference value but can be accomplished with digital electronics in an integrated chip. Fluctuations in laser power will cause problems as the calibrated reference value depends on the input power of the ring. Therefore, any variation in the input power will affect the locking point.

The fourth method, which involves monitoring the photocurrent in the pn diode of the MRM [9], stands out for not requiring any additional sensor in the thermal controller. This makes it a promising solution for hybrid chip solutions, where wirebonds between chips can pose a limitation. However, this method requires precise calibrations where the ratio of the TIA sensors needs to be tuned to the desired locking point.

The fifth approach, which employs high-speed electronics to measure the OMA [8], provides a solution for almost all essential system requirements. However, it demands high-speed electronics to accurately track the OMA, resulting in higher power consumption as the modulation frequency increases.

The final controller, which implements a thermal dithering signal to extract the second derivative of resonance [5], meets almost all the system requirements. However, all experimental results started with the laser wavelength near resonance. In cases where the laser is far from resonance, the second derivative becomes zero, and the controller should not lock. Considering the possibility of process variation causing the laser to be far from resonance, it is crucial to have additional control that implements a start-up sequence to enter the capturing range of the dithering control.

The new approach is capable of meeting all system requirements by locking where the average through and drop powers are identical. Its most significant feature is the ability to lock any double-bus MRM under any initial conditions, provided the integrated heater can shift a full FSR. As the number of rings in a design increases, the fabrication and implementation processes are significantly simplified, thus increasing scalability. Although the extra drop sensor can limit hybrid solutions, it is not a problem in a monolithic solution. Additionally, the implementation is fully analog, reducing the required electrical components. This technique is also compatible with WDM systems. By modulating different input wavelengths in separate waveguides and combining all waveguides after modulation, the final waveguide will contain multiple encoded wavelengths, making this compatible with WDM. Finally, since thermal fluctuation has a slow time evolution, it can be envisioned that a single thermal controller can control multiple rings, reducing footprint and circuit power.

However, this technique requires a power tap at the through output, which reduces the actual transmitted power. In [5], they employ a ContactLess Integrated Photonic Probe

(CLIPP) instead of PD to measure the MRMs through output, which is noninvasive, so it does not reduce the output powers. If the CLIPP is used instead of PDs for this controlling method, no additional losses will be induced by the controller.

5.2 Conclusion

As the demand for bandwidth continues to increase, MRMs offer a promising solution with its high bandwidth, energy efficiency, and compact size. However, MRM technology is susceptible to thermal and process variations, hindering its commercial viability. Therefore, a simple and reliable stabilization circuit is essential for MRM to be a feasible option for commercial applications. The focus of this work was to present a novel stabilization technique for MRM that effectively caters to all essential system prerequisites.

Chapter 2 reviewed the fundamental knowledge required to comprehend this work and compared existing stabilization techniques for MRMs.

Chapter 3 provided a new approach to stabilizing MRM and a detailed description of its operation. Moreover, simulations have demonstrated that this approach is calibration-free, stabilizes against thermal fluctuations, and is immune to laser power and wavelength variations. A detailed analysis of the controller's closed-loop stability was then provided. Furthermore, simulations indicated that the design does not stabilize for data density variations. Finally, experimental results from a PCB implementation provided strong validation of the design's effectiveness.

Chapter 4 discussed the addition of a VG-TIA to the controller, which enabled data density-independent stabilization. The simulation results highlighted that the controller significantly lessens the input density dependence of the scheme. However, due to the use of imperfect linear fittings, it cannot be entirely eliminated, but this only resulted in a minor decrease in OMA.

5.3 Future Work

The experimental results obtained using a PCB provide strong evidence to conduct further research on this novel approach for actively stabilizing Magnetically Resonant Systems (MRMs). Various research directions can be undertaken to enhance the validation of this design:

- Because the optical chip was not initially designed for high-speed modulation, maintaining lock under high-speed modulation has yet to be demonstrated. As a crucial next step, testing the controller under high-speed modulation is vital to determine its effectiveness.
- The ASIC implementation of the thermal controller described is necessary to evaluate power efficiency and circuit footprint for balanced data.
- To determine the feasibility of using linear fittings to compensate for input data density, the modified thermal controller needs to be implemented in an ASIC for unbalanced modulation.
- To reduce power consumption and footprint while increasing scalability, optimizing the design to allow a single controller to stabilize multiple rings is important.
- Investigate the time constants of the active heating and passive cooling to determine the speed limitations of the controller.
- Investigate the feasibility of using this controller to lock MRR in filter application by changing through and dropping TIA gains.
- To determine the controllers' ability to remain locked in a dense grid of MRM, it is vital to investigate the thermal cross-talk effect on the controller.

- Investigate the feedback controller's performance when implemented as a digital controller instead and compare it to the analog controller presented in this research.
- Investigate the possibility of using different modulation schemes other than amplitude modulation.

Appendix A

Simulation Models

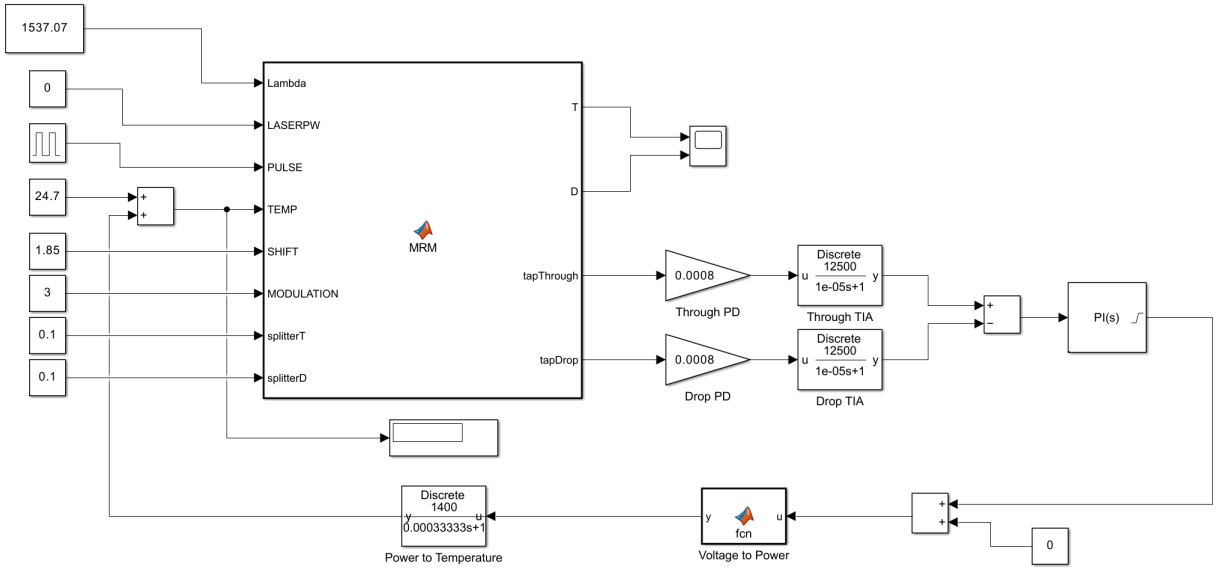

Figure A.1: Simulink model used for simulation results

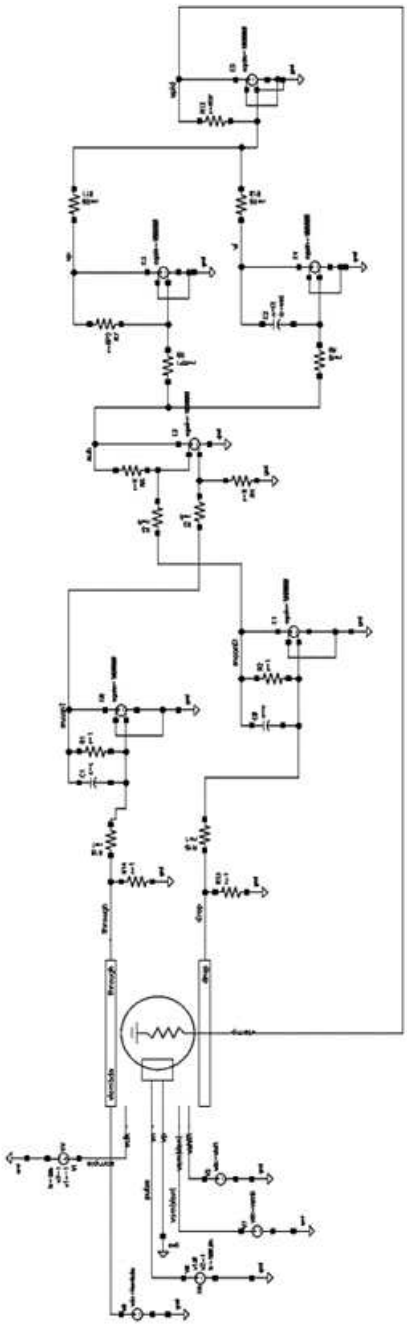

Figure A.2: Cadence model used to validate OpAmp design

Appendix B

PCB KiCad Design

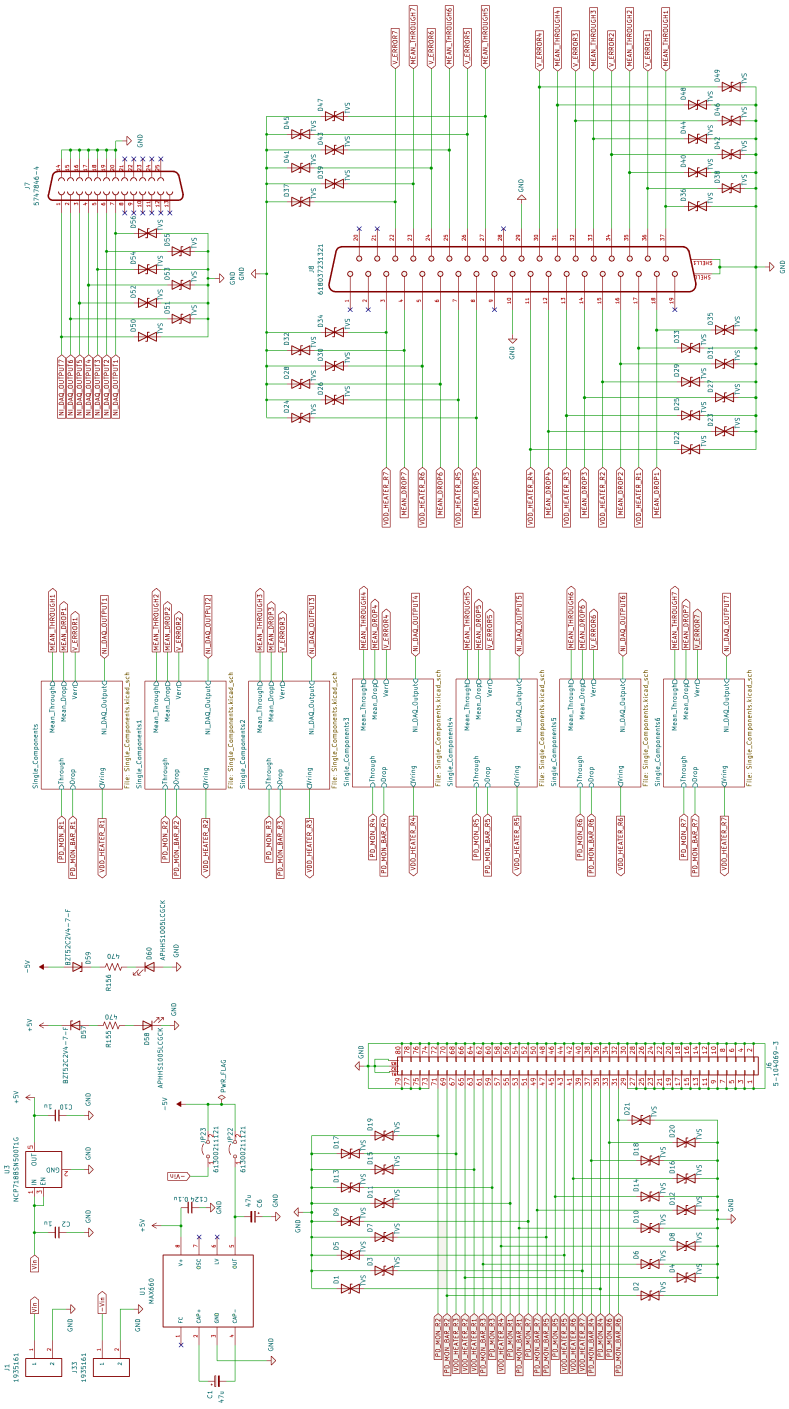

Figure B.1: PCB KiCad schematic page 1

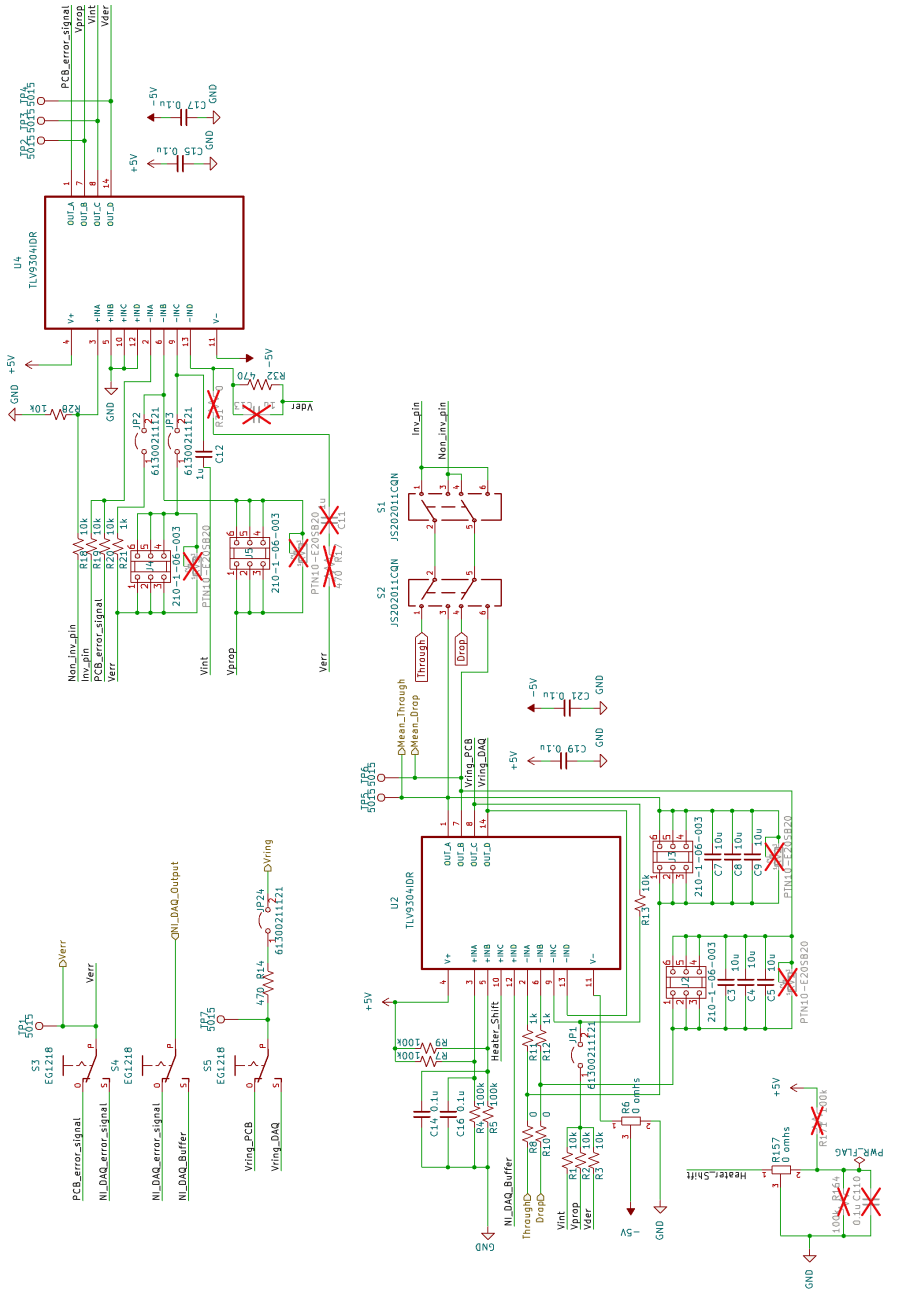

Figure B.2: PCB KiCad schematic page 2

Figure B.3: Fabricated PCB

Bibliography

[1] W. Bogaerts, P. De Heyn, T. Van Vaerenbergh, K. De Vos, S. Kumar Selvaraja, T. Claes, P. Dumon, P. Bienstman, D. Van Thourhout, and R. Baets, "Silicon microring resonators," *Laser & Photonics Reviews*, vol. 6, no. 1, pp. 47–73, 2012. [Online]. Available: https://onlinelibrary.wiley.com/doi/abs/10.1002/lpor.201100017

[2] K. Padmaraju, J. Chan, L. Chen, M. Lipson, and K. Bergman, "Thermal stabilization of a microring modulator using feedback control," *Optics Express*, vol. 20, no. 27, Dec 2012.

[3] K. Padmaraju, D. F. Logan, X. Zhu, J. J. Ackert, A. P. Knights, and K. Bergman, "Integrated thermal stabilization of a microring modulator," *Optics Express*, vol. 21, no. 12, p. 14342, Jun 2013.

[4] K. Padmaraju, D. F. Logan, J. J. Ackert, A. P. Knights, and K. Bergman, "Microring resonance stabilization using thermal dithering," in *2013 Optical Interconnects Conference*, 2013, pp. 58–59.

[5] V. Grimaldi, F. Zanetto, F. Toso, I. Roumpos, T. Chrysostomidis, A. Perino, M. Petrini, F. Morichetti, A. Melloni, N. Pleros, M. Moralis-Pegios, K. Vyrsokinos, G. Ferrari, and M. Sampietro, "Self-stabilized 50 gb/s silicon photonic microring modulator using a power-independent and calibration-free control loop," *Journal of Lightwave Technology*, vol. 41, no. 1, pp. 218–225, 2023.

[6] S. Saeedi and A. Emami, "Silicon-photonic ptat temperature sensor for micro-ring resonator thermal stabilization," *Opt. Express*, vol. 23, no. 17, pp. 21 875–21 883, Aug 2015. [Online]. Available: https://opg.optica.org/oe/abstract.cfm?URI=oe-23-17-21875

[7] W. A. Zortman, A. L. Lentine, D. C. Trotter, and M. R. Watts, "Bit-error-rate monitoring for active wavelength control of resonant modulators," *IEEE Micro*, vol. 33, no. 1, pp. 42–52, 2013.

[8] S. Agarwal, M. Ingels, M. Pantouvaki, M. Steyaert, P. Absil, and J. Van Campenhout, "Wavelength locking of a si ring modulator using an integrated drop-port oma monitoring circuit," *IEEE Journal of Solid-State Circuits*, vol. 51, no. 10, pp. 2328–2344, 2016.

[9] J. Sharma, Z. Xuan, H. Li, T. Kim, R. Kumar, M. N. Sakib, C.-M. Hsu, C. Ma, H. Rong, G. Balamurugan, and J. Jaussi, "Silicon photonic microring-based 4 × 112 gb/s wdm transmitter with photocurrent-based thermal control in 28-nm cmos," *IEEE Journal of Solid-State Circuits*, vol. 57, no. 4, pp. 1187–1198, 2022.

[10] J. Teng, P. Dumon, W. Bogaerts, H. Zhang, X. Jian, X. Han, M. Zhao, G. Morthier, and R. Baets, "Athermal silicon-on-insulator ring resonators by overlaying a polymer cladding on narrowed waveguides," *Opt. Express*, vol. 17, no. 17, pp. 14 627–14 633, Aug 2009. [Online]. Available: https://opg.optica.org/oe/abstract.cfm?URI=oe-17-17-14627

[11] A. V. Krishnamoorthy, H. D. Thacker, O. Torudbakken, S. Müller, A. Srinivasan, P. J. Decker, H. Opheim, J. E. Cunningham, I. Shubin, X. Zheng, M. Dignum, K. Raj, E. Rongved, and R. Penumatcha, "From chip to cloud: Optical interconnects in engineered systems," *Journal of Lightwave Technology*, vol. 35, no. 15, pp. 3103–3115, 2017.

[12] R. Mahajan, X. Li, J. Fryman, Z. Zhang, S. Nekkanty, P. Tadayon, J. Jaussi, S. Shumarayev, A. Agrawal, S. Jadhav, K. A. Singh, A. Alduino, S. Gujjula, C.-P. Chiu, T. Nordstog, K. J. Hosseini, S. Sane, N. Deshpande, K. Aygün, A. Sarkar, P. Dobriyal, S. Pothukuchi, V. A. Pogue, and D. Hui, "Co-packaged photonics for high performance computing: Status, challenges and opportunities," *Journal of Lightwave Technology*, vol. 40, no. 2, pp. 379–392, 2022.

[13] D. Thomson, A. Zilkie, J. E. Bowers, T. Komljenovic, G. T. Reed, L. Vivien, D. Marris-Morini, E. Cassan, L. Virot, J.-M. Fédéli, and et al., "Roadmap on silicon photonics," *Journal of Optics*, vol. 18, no. 7, p. 073003, Jun 2016.

[14] G. T. Reed, G. Mashanovich, F. Y. Gardes, and D. J. Thomson, "Silicon optical modulators," *Nature Photonics*, vol. 4, no. 8, p. 518–526, Jul 2010.

[15] Z. Lu, J. Jhoja, J. Klein, X. Wang, A. Liu, J. Flueckiger, J. Pond, and L. Chrostowski, "Performance prediction for silicon photonics integrated circuits with layout-dependent correlated manufacturing variability," *Opt. Express*, vol. 25, no. 9, pp. 9712–9733, May 2017. [Online]. Available: https://opg.optica.org/oe/abstract.cfm?URI=oe-25-9-9712

[16] M. Pantouvaki, P. Verheyen, G. Lepage, J. De Coster, H. Yu, P. De Heyn, P. Absil, and J. Van Campenhout, "20gb/s silicon ring modulator co-integrated with a ge monitor photodetector," in *39th European Conference and Exhibition on Optical Communication (ECOC 2013)*, 2013, pp. 1–3.

[17] M. Nawrocka, T. Liu, X. Wang, and R. Panepucci, "Tunable silicon microring resonator with wide free spectral range," *Applied Physics Letters - APPL PHYS LETT*, vol. 89, 08 2006.

[18] P. Dong, R. Shafiiha, S. Liao, H. Liang, N.-N. Feng, D. Feng, G. Li, X. Zheng, A. V. Krishnamoorthy, and M. Asghari, "Wavelength-tunable silicon microring modulator," *Opt. Express*, vol. 18, no. 11, pp. 10 941–10 946, May 2010. [Online]. Available: https://opg.optica.org/oe/abstract.cfm?URI=oe-18-11-10941

[19] S. K. Selvaraja, W. Bogaerts, P. Dumon, D. Van Thourhout, and R. Baets, "Sub-nanometer linewidth uniformity in silicon nanophotonic waveguide devices using cmos fabrication technology," *IEEE Journal of Selected Topics in Quantum Electronics*, vol. 16, no. 1, pp. 316–324, 2010.

[20] J. Garcia-Echeverria, G. Cowan, O. Liboiron-Ladouceur, and D. Rolston, "Towards combinational logic circuits based on optical logic gates," in *2023 Photonics North (PN)*, 2023, pp. 1–2.

[21] B. Guha, B. B. C. Kyotoku, and M. Lipson, "Cmos-compatible athermal silicon microring resonators," *Opt. Express*, vol. 18, no. 4, pp. 3487–3493, Feb 2010. [Online]. Available: https://opg.optica.org/oe/abstract.cfm?URI=oe-18-4-3487

[22] B. Guha, J. Cardenas, and M. Lipson, "Athermal silicon microring resonators with titanium oxide cladding," *Opt. Express*, vol. 21, no. 22, pp. 26 557–26 563, Nov 2013. [Online]. Available: https://opg.optica.org/oe/abstract.cfm?URI=oe-21-22-26557

[23] K. Padmaraju, D. F. Logan, T. Shiraishi, J. J. Ackert, A. P. Knights, and K. Bergman, "Wavelength locking and thermally stabilizing microring resonators using dithering signals," *Journal of Lightwave Technology*, vol. 32, no. 3, pp. 505–512, 2014.

[24] C. T. DeRose, M. R. Watts, D. C. Trotter, D. L. Luck, G. N. Nielson, and R. W. Young, "Silicon microring modulator with integrated heater and temperature sensor for thermal control," in *CLEO/QELS: 2010 Laser Science to Photonic Applications*, 2010, pp. 1–2.

[25] S. Yang, X. Zhu, Y. Zhang, Y. Li, T. Baehr-Jones, M. Hochberg, and K. Bergman, "Thermal stabilization of a microring resonator using bandgap temperature sensor," in *2015 IEEE Optical Interconnects Conference (OI)*, 2015, pp. 44–45.

[26] R. Nandi, V. Ruparelia, V. R. Kuppireddy, I. Som, P. K. Sharma, A. Chatterjee, A. Aboketaf, C. Hedges, C. Pike, F. Pavlik, and et al., "Thermal stabilization of micro-ring modulator using a monolithically integrated analog feedback circuit," in *Presented at 24th European Conference on Integrated Optics*, 2023.

[27] C. Li, R. Bai, A. Shafik, E. Z. Tabasy, B. Wang, G. Tang, C. Ma, C.-H. Chen, Z. Peng, M. Fiorentino, R. G. Beausoleil, P. Chiang, and S. Palermo, "Silicon photonic transceiver circuits with microring resonator bias-based wavelength stabilization in 65 nm cmos," *IEEE Journal of Solid-State Circuits*, vol. 49, no. 6, pp. 1419–1436, 2014.

[28] K. Padmaraju, J. Chan, L. Chen, M. Lipson, and K. Bergman, "Dynamic stabilization of a microring modulator under thermal perturbation," in *Optical Fiber Communication Conference*. Optica Publishing Group, 2012, p. OW4F.2. [Online]. Available: https://opg.optica.org/abstract.cfm?URI=OFC-2012-OW4F.2

[29] X. Zheng, E. Chang, P. Amberg, I. Shubin, J. Lexau, F. Liu, H. Thacker, S. S. Djordjevic, S. Lin, Y. Luo, J. Yao, J.-H. Lee, K. Raj, R. Ho, J. E. Cunningham, and A. V. Krishnamoorthy, "A high-speed, tunable silicon photonic ring modulator integrated with ultra-efficient active wavelength control," *Opt. Express*, vol. 22, no. 10, pp. 12 628–12 633, May 2014. [Online]. Available: https://opg.optica.org/oe/abstract.cfm?URI=oe-22-10-12628

[30] H. Li, Z. Xuan, A. Titriku, C. Li, K. Yu, B. Wang, A. Shafik, N. Qi, Y. Liu, R. Ding, T. Baehr-Jones, M. Fiorentino, M. Hochberg, S. Palermo, and P. Y. Chiang, "A 25 gb/s, 4.4 v-swing, ac-coupled ring modulator-based wdm transmitter with wavelength

stabilization in 65 nm cmos," *IEEE Journal of Solid-State Circuits*, vol. 50, no. 12, pp. 3145–3159, 2015.

[31] S. Manipatruni, R. K. Dokania, B. Schmidt, N. Sherwood-Droz, C. B. Poitras, A. B. Apsel, and M. Lipson, "Wide temperature range operation of micrometer-scale silicon electro-optic modulators," *Optics Letters*, vol. 33, no. 19, p. 2185–2187, Oct 2008.

[32] K. Padmaraju and K. Bergman, "Resolving the thermal challenges for silicon microring resonator devices," *Nanophotonics*, vol. 3, no. 4–5, p. 269–281, 2014.

[33] C. Qiu, J. Shu, Z. Li, X. Zhang, and Q. Xu, "Wavelength tracking with thermally controlled silicon resonators," *Opt. Express*, vol. 19, no. 6, pp. 5143–5148, Mar 2011. [Online]. Available: https://opg.optica.org/oe/abstract.cfm?URI=oe-19-6-5143

[34] M. Kim, M.-H. Kim, Y. Jo, H.-K. Kim, S. Lischke, C. Mai, L. Zimmermann, and W.-Y. Choi, "Silicon electronic photonic integrated 25 gb/s ring modulator transmitter with a built-in temperature controller," *Photon. Res.*, vol. 9, no. 4, pp. 507–513, Apr 2021. [Online]. Available: https://opg.optica.org/prj/abstract.cfm?URI=prj-9-4-507

[35] Y. Kokubun, N. Funato, and M. Takizawa, "Athermal waveguides for temperature-independent lightwave devices," *IEEE Photonics Technology Letters*, vol. 5, no. 11, pp. 1297–1300, 1993.

[36] X. Guan, W. Shi, and L. A. Rusch, "Ultra-dense wavelength-division multiplexing with microring modulator," *Journal of Lightwave Technology*, vol. 39, no. 13, pp. 4300–4306, 2021.

[37] C. Sun, M. Wade, M. Georgas, S. Lin, L. Alloatti, B. Moss, R. Kumar, A. H. Atabaki, F. Pavanello, J. M. Shainline, J. S. Orcutt, R. J. Ram, M. Popović, and V. Stojanović, "A 45 nm cmos-soi monolithic photonics platform with bit-statistics-based resonant

microring thermal tuning," *IEEE Journal of Solid-State Circuits*, vol. 51, no. 4, pp. 893–907, 2016.